Regulation of Lysosomal Chloride and Proton Concentrations in Mammalian Cells

Inaugural-Dissertation

zur Erlangung des Doktorgrades
der Mathematisch-Naturwissenschaftlichen Fakultät
der Heinrich-Heine-Universität Düsseldorf

vorgelegt von

Andrea Jansen-Grabowski
aus Papenburg

Jülich, Juli 2020

aus dem Institute of Biological Information Processing 1 (IBI-1) –
Molecular and Cellular Physiology des Forschungszentrums Jülich

Gedruckt mit Genehmigung der
Mathematisch-Naturwissenschaftlichen Fakultät der
Heinrich-Heine-Universität Düsseldorf

Berichterstatter:

1. Prof. Dr. Christoph Fahlke

2. Prof. Dr. Christine R. Rose

Tag der mündlichen Prüfung: 21.01.2021

"Das Schönste, was wir erleben können, ist das Geheimnisvolle"
Albert Einstein

Zusammenfassung

Lysosomen sind Zellorganellen, die eine wichtige Rolle beim Energiemetabolismus, der Antigenprozessierung und der Verdauung von Makromolekülen durch hydrolytische Enzyme spielen, und Veränderungen der lysosomalen Funktion werden mit schwerwiegenden Krankheiten in Verbindung gebracht. Wichtige Funktionen von Lysosomen sind abhängig von einer korrekten Ionen-Homöostase. Unser bisheriges Wissen über die Zusammensetzung und Regulation lysosomaler Ionen ist unzureichend. Das sehr saure Lumen erschwert den Gebrauch von genetischen Biosensoren für die Messung von Ionenkonzentrationen im Lysosom.

In dieser Arbeit wird erstmals eine Methode demonstriert, mit der die beiden quinolinium-basierten chloridsensitiven Fluoreszenzfarbstoffe SPQ (6-Methoxy-N-(3-Sulfopropyl)Quinolinium) und MEQ (6-Methoxy-N-Ethylquinolinium Iodid) für die Messung der lysosomalen Chloridkonzentration ($[\mathrm{Cl}^-]$) mittels Fluoreszenzlebenszeitmikroskopie (FLIM) verwendet werden können. SPQ und MEQ werden über Kollisions-Fluoreszenzauslöschung durch Chlorid gequencht und haben daher Fluoreszenzlebenszeiten, welche von der umgebenden Chloridkonzentration abhängen und zudem unabhängig von der Konzentration des Fluorophors und von Instrumenteneigenschaften sind, weshalb sich diese Messmethode perfekt für die Messung absoluter Konzentrationen eignet.

SPQ ist membranimpermeabel und gelangt über Endozytose in die Lysosomen. Die reduzierte Form von MEQ, diH-MEQ, ist dagegen membranpermeabel und gelangt über Diffusion in die Zelle und die Lysosomen, wo es dann rasch zu MEQ reoxidiert [1]. MEQ ermöglicht daher das simultane Messen der lysosomalen und zytosolischen $[\mathrm{Cl}^-]$ nach Vergrößerung der Lysosomen durch den PIKfyve-Blocker YM-201636.

Unter physiologischen Bedingungen weisen die Lysosomen von HEK293T Zellen eine sehr hohe $[\mathrm{Cl}^-]$ von ~ 150 mM auf, während die zytosolische $[\mathrm{Cl}^-]$ etwa 56 mM beträgt. Um die Transportmechanismen zu untersuchen, welche für die lysosomale Chloridakkumulation sorgen, und um die Auswirkungen von Veränderungen in der lysosomalen $[\mathrm{Cl}^-]$ zu verstehen, haben wir FLIM mit ratiometrischen pH-Messungen kombiniert, sowie mit der Überexpression, dem Knock-down und dem pharmakologischen Blockieren verschiedener Ionenkanäle und -transporter. Die Ergebnisse zeigen eine Korrelation zwischen der lysosomalen $[\mathrm{Cl}^-]$ und dem pH. Des Weiteren deuten sie darauf hin, dass lysosomales Chlorid in einem sekundäraktiven Prozess, angetrieben von der vesikulären ATPase, akkumuliert wird. Die Chloridakkumulation ist elektrogen und wird über Änderungen des Membranpotentials modifiziert. Verschiedene Transporter, die

möglicherweise bei der Akkumulation des lysosomalen Chlorid eine Rolle spielen, wurden getestet. Dabei wurde festgestellt, dass der Chlorid-Protonen-Antiporter ClC-7 Chlorid nicht akkumuliert, sondern heraustransportiert und dabei Protonen in das Lysosom bewegt.

Abstract

Lysosomes are cell organelles with important roles in energy metabolism, antigen processing, and digestion of macromolecules via hydrolytic enzymes, and changes in lysosomal function are associated with severe human diseases. Key lysosomal functions depend on proper ion homeostasis. Hitherto, our knowledge about the ion composition and regulation in lysosomes is insufficient. Lysosomes exhibit a very acidic pH, which impedes the use of genetically encoded biosensors for measuring ion concentrations in these organelles.

In this work, it is demonstrated for the first time that the two quinolinium-based chloride-sensitive fluorescent dyes, SPQ (6-methoxy-N-(3-sulfopropyl)quinolinium) and MEQ (6-methoxy-N-ethylquinolinium iodide), can be used to measure lysosomal chloride concentrations ($[Cl^-]$) via fluorescence lifetime imaging microscopy (FLIM). SPQ and MEQ are collisionally quenched by chloride and exhibit chloride dependent fluorescence lifetimes, which are independent of fluorophore concentrations and instrumental properties and therefore perfectly suited as a readout to determine absolute concentrations.

SPQ is membrane-impermeant and loaded into lysosomes via the endocytic pathway. A reduced form of MEQ, diH-MEQ, is membrane permeable and can be loaded into the cells and lysosomes via diffusion, where it is trapped after rapid reoxidization to the cell-impermeant MEQ [1]. MEQ thus permits simultaneous measurements of lysosomal and cytosolic chloride concentrations, after enlargement of the lysosomes via the PIKfyve inhibitor YM-201636.

Under physiological conditions, lysosomes of HEK293T cells exhibit very high $[Cl^-]$ of ~ 150 mM, while the cytosolic $[Cl^-]$ is ~ 56 mM. To study transport processes that are responsible for lysosomal chloride accumulation and to understand the effects of changes in lysosomal $[Cl^-]$, FLIM was combined with ratiometric lysosomal pH measurements and overexpression, knock-down, or pharmacological blocking of various ion channels and transporters in HEK293T cells. Results from this work show a correlation between lysosomal $[Cl^-]$ and pH and that chloride facilitates lysosomal acidification. Furthermore, it is shown that lysosomes accumulate chloride in a secondary active process, driven by the vesicular v-type ATPases. Chloride accumulation is electrogenic and directly modified by changes in the membrane potential. Several candidate transporters were tested and could be ruled out. Results indicate that the chloride proton antiporter ClC-7 does not accumulate chloride in the lysosome but rather transports chloride out of the lysosome, thereby driving proton inward movement.

Contents

List of Figures

List of Tables

Chapter 1

Introduction

1.1 The Lysosome

Lysosomes are membrane-bound cell organelles with important roles in the degradation and recycling of material from extracellular as well as intracellular sources [5, 6, 7]. They digest proteins, polysaccharides, and complex lipids into amino acids, monosaccharides, and free fatty acids using a variety of lipases, proteases, and glycosidases. Although historically referred to as the waste disposal system of the cell, it has been reported that the lysosome has a much broader function, e.g. in secretion, cell signaling, and plasma membrane repair [8, 9]. Along with its function in autophagy, the lysosome is the centre of several vital processes like nutrient sensing, metabolism, and homeostasis [10, 11, 12].

1.1.1 The Lysosomal Pathway

Lysosomes receive material via two major pathways: endocytosis and autophagy. These pathways are schematically illustrated in figure 1.1.

During endocytosis, material from outside the cell enters the lysosome through the invagination of the plasma membrane and pinching off an endocytic vesicle or early endosome (EE), that contains ingested substances. These substances are then delivered to the late endosomes (LE), also called multivesicular bodies (MVB), which then fuse with lysosomes to form endolysosome (EL) hybrids.

Damaged intracellular organelles are phagocyted from autophagosomes (APs), which then form autolysosomes (ALs) by fusion with lysosomes.

ELs and ALs can also exchange material or fuse to form EL-AL hybrids. The endocytic and autophagic material in the ELs and ALs is then degraded by lysosomal acid hydrolases.

Insoluble catabolites can be transported to the trans-Golgi network for reutilization via transport vesicles or released into the extracellular medium via lysosomal exocytosis. When degradation is completed, ALs undergo extensive tubulation and form tubular ALs (Tu-ALs), from which protolysosomes are regenerated [13].

The intracellular motion of lysosomes is a combination of diffusion and active, ATP-dependent transport via the motor proteins kinesin and dynein, which move the lysosome along microtubules [8, 14, 15].

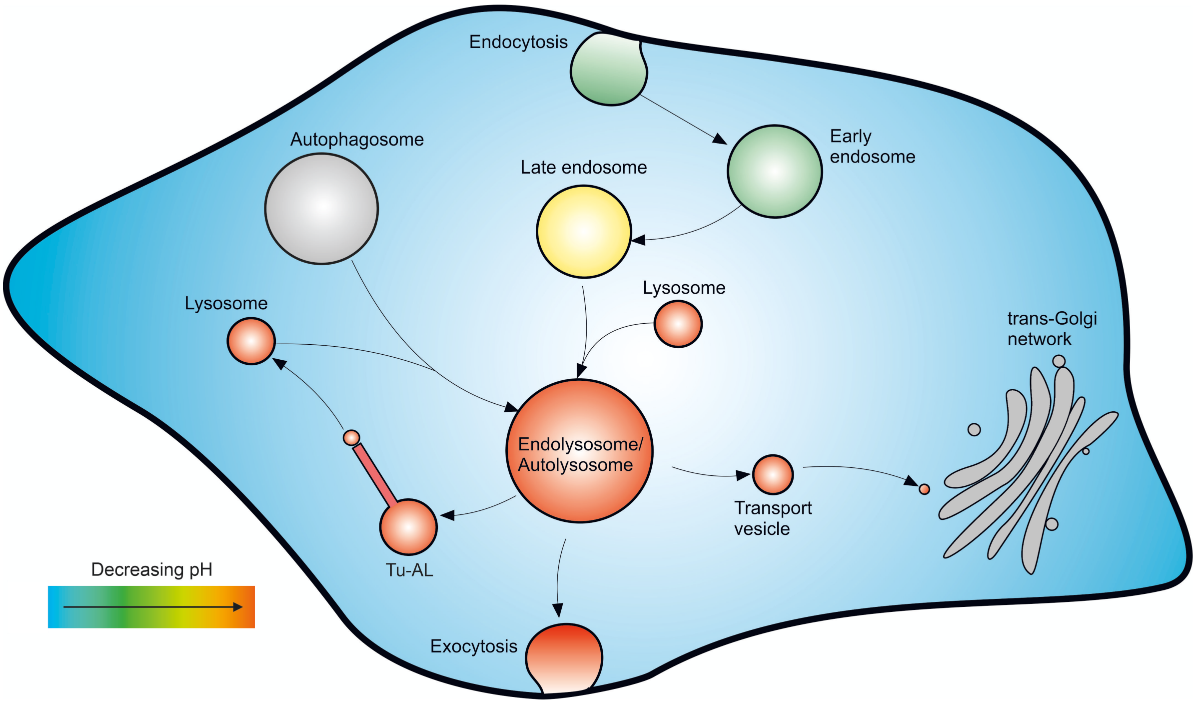

Figure 1.1: Scheme illustrating the lysosomal pathways (modified from [13]).

1.1.2 Lysosomal Acidification

For the degradation of ingested material, the lysosome lumen, i.e. the volume enclosed by the lysosomal membrane, contains hydrolases. These enzymes are most efficient in an acidic environment, so lysosomal acidification plays a major role in intracellular digestion

[16]. The inhibition of the enzymatic activity at neutral pH protects the cell against uncontrolled digestion: If the acid hydrolases were to be released into the cytosol they would be inactivated by the neutral cytosolic pH [17].

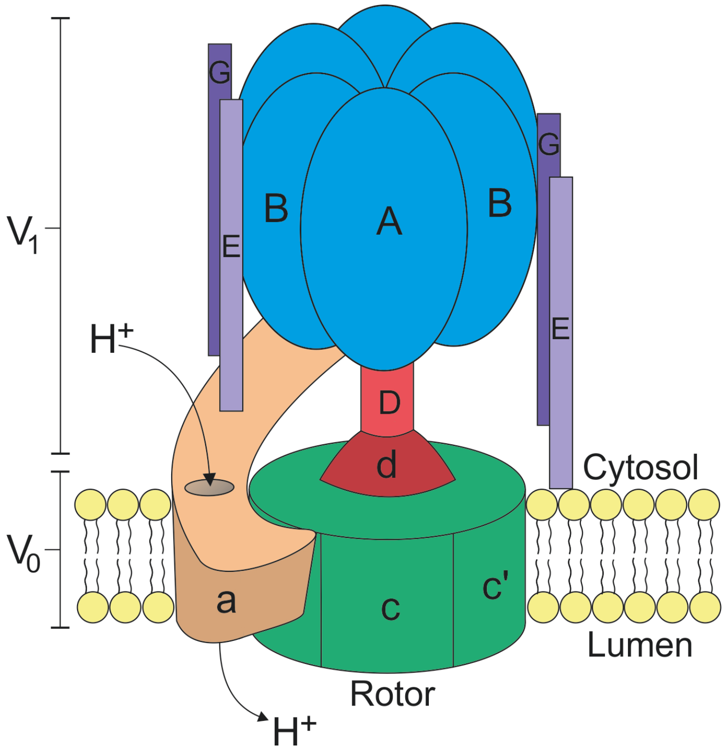

Figure 1.2: Structure of the v-ATPase (modified from [18]). The V_1-domain consists of the ATP-hydrolyzing subunits A and B (blue). The subunit D of the V_1-domain and the subunit d of the V_0-domain compose the central stalk (red). This stalk connects the ATP-hydrolizing subunits to the rotor (green), made up of the subunits c, c', and c". The rotor is embedded in the membrane and transports protons from the cytoplasmic side to the luminal side through the subunit a (brown), which contains access pathways to both sides of the membrane. The subunits E and G (purple) compose the peripheral stalks.

The luminal pH decreases in the vesicles along the endocytic pathway (see color legend in figure 1.1). The lysosomal lumen has a pH between 4.3 and 5.5 [18, 19]. The vacuolar ATPases (v-ATPases) in the endosomal and lysosomal membrane are primarily involved in acidifying these organelles. V-ATPases are multi-subunit protein complexes, composed of a cytosolic V_1-domain and a lysosomal membrane-anchored V_0-domain (figure 1.2). The V_1-domain generates energy by ATP hydrolysis, which drives movement of a central rotary complex. This, in turn, results in the transport of protons from the cytoplasm through the integral V_0-domain into the vesicle lumen, leading to acidification of the lumen [18, 20, 21].

With each proton pumped into the lysosome, a lumen positive membrane potential is generated, which impedes further pumping. To dissipate this potential, the proton movement must be accompanied by a counterion flux. This can either be an outward flux of other cations out of the lysosome, or an inward flux of cytoplasmic anions, or both [18].

1.1.3 The Role of Chloride in the Lysosome

Chloride is the most abundant anion in living organisms and is involved in a variety of crucial cellular processes, such as volume regulation of the cell, water-salt balance, and neurotransmission [22, 23, 24]. It has also been shown that chloride can function as a second messenger and modulate the expression of several genes [25, 26]. Thus, alterations in Cl^- homeostasis lead to several human diseases [27].

Compared to the cytosol and other organelles within the endosomal pathway, lysosomes possess very high chloride concentrations [28]. Lysosomal chloride regulates Ca^{2+} release from the lysosome [29], which is required for fusion of lysosomes with other compartments, including endosomes and the plasma membrane [30]. Furthermore, it has been suggested that chloride is an important counterion required for the acidification of the lysosome, as mentioned earlier. Indeed, the disruption of the Cl^-/H^+ exchanger ClC-5 in the endosomal membrane as well as the knock-out of ClC-3, a Cl^-/H^+ exchanger which is present in the membrane of synaptic vesicles, impairs the acidification of endosomes and synaptic vesicles, respectively [31, 32]. This gives rise to the assumption that chloride might also play an important role in the maintenance of the lysosomal pH. However, reports that the lysosomal pH is unaffected in neurons of ClC-7 knockout mice have raised questions regarding the role of chloride in lysosomal acidification [33], which has since been a matter of ongoing debate [34].

1.1.4 Chloride Transport Through the Lysosomal Membrane

There are several known chloride transporters in the lysosomal membrane, which are members of the CLC family of Cl^- channels and transporters. These are the ClC-3 splice variants ClC-3a and ClC-3b [35], ClC-6, which is almost exclusively expressed in neurons of the central and peripheral nervous system [36], and ClC-7 [37]. All of them are Cl^-/H^+ exchangers with a $2Cl^-:1H^+$ stoichiometry [34].

It has been suggested that these CLCs transport protons out of the lysosome and chloride into the lysosome [33], leading to high luminal chloride concentrations, and there are studies which support this hypothesis [38, 39]. However, a study by Rohrbough et al.

[40], where they used patch-clamp recordings to examine ClC-3, challenges this assumption, as their results indicate an outward flux of chloride out of the endosome/lysosome. Similar experiments also show that ClC-7 is a strong outward rectifier, indicating a primary direction of Cl^- flow through ClC-7 out of the lumen and proton flow into the lumen [4, 41].

The transport mechanisms that lead to the accumulation of lysosomal chloride are still not entirely understood.

1.1.5 Diseases Caused by Lysosomal Dysfunction

Key lysosomal functions depend on proper ion homeostasis, regulated by a network of lysosomal proteins, and a disturbance of any part of this network can cause human diseases: Genetic alterations of lysosomal hydrolases lead to lysosomal storage diseases (LSDs), such as Gaucher, Fabry, Krabbe, Pompe, or Niemann-Pick disease, with symptoms like cardiac problems, bone abnormalities, dementia, deafness, blindness, and movement problems [42, 43].

A dysfunction of ClC-7 or its β-subunit Ostm1 (osteopetrosis-associated transmembrane protein 1), which is required for the transport activity as well as the stability of ClC-7 [41, 44], causes osteopetrosis and a form of neuronal ceroid lipofuscinosis (NCL), characterized by a progressive loss of motor and intellectual ability, blindness, seizures, and early death [33, 37, 45, 46]. The mutation Y750Q of ClC-7, which accelerates its usually slow voltage-dependent activation, leads to osteopetrosis and gingival harmatomas in cattle (human analogue: ClC-7 Y746Q) [47].

In recent years, the role of lysosomal dysfunction in neurodegeneration has been widely appreciated in Alzheimer´s or Parkinson´s disease as well as in fronto-temporal dementia [48, 49]. Alzheimer's disease, for example, can be caused by a mutation of the protein presenilin-1 (PS1), which is involved in targeting the V0a1 subunit of the V-ATPase to the lysosomes. The mutated form of PS1 fails in that function, resulting in inadequate autolysosome/lysosome acidification [50].

1.1.6 Aim of This Study

The mechanisms underlying lysosomal ion homeostasis, and the ion transport processes permitting ion gradients across lysosomal membranes are insufficiently understood. Technical challenges limit the possibilities to monitor the physical state and ionic composition in these vesicles.

Chloride is the most abundant anion in living organisms, and there are several chloride-sensitive reporters to measure chloride concentrations in cells, but not many of them are suitable to measure chloride concentrations in the lysosome. Genetically encoded sensors based on fluorescent proteins, such as Cl-Sensor [51] and Clomeleon [52], can specifically be targeted to intracellular compartments by incorporation of localization signals. They are, however, pH-sensitive and therefore require the simultaneous determination of the pH for quantitative chloride measurements. In contrast to that, chloride sensitive organic fluorescent dyes, like MEQ (6-methoxy-N-ethylquinolinium iodide), MQAE (1-(Ethoxycarbonylmethyl)-6-methoxyquinolinuim bromide), or SPQ (6-methoxy-N-(3-sulfopropyl)quinolinium), are insensitive to pH-changes and sensitive to chloride across the entire physiological regime [1, 53, 54, 55], but attempts to target these dyes to specific organelles by chemical conjugation, e.g. to dextran, lead to a massive reduction of their chloride sensitivity [38].

In this study, a method is established to load the lysosomes of HEK293T cells with free MEQ and SPQ, and fluorescence lifetime imaging microscopy is used to measure lysosomal [Cl^-]. To examine transport processes that are responsible for lysosomal chloride accumulation and to understand the effects of changes in lysosomal [Cl^-], FLIM is combined with ratiometric lysosomal pH measurements and overexpression, knock-down, and pharmacological blocking of various ion channels and transporters.

1.2 Chloride Imaging

1.2.1 Fluorescence Lifetime Imaging Microscopy

A molecule with absorption in the ultraviolet, visible, or near-infrared spectral region that shows sizeable probability for emission of a photon upon absorption is called a fluorophore. Fluorescence can occur when a fluorophore absorbs the energy of a photon (hν, where h is the Planck constant and ν the frequency of the photon) or, in case of two-photon excitation, the sum of the energies of two photons, which transfers an electron of the molecule from the ground state (S_0) to the excited state (S_1) (figure 1.3). From this state the fluorophore returns to the ground state (S_0) either non-radiatively (vibrational relaxation (VR), internal conversion, quenching) or by the emission of fluorescence light. The deactivation of the fluorescence is described by an exponential decay:

$$I(t) = I_0 e^{-t/\tau} \tag{1.1}$$

I_0 is the fluorescence intensity directly after excitation, $I(t)$ is the fluorescence intensity after a time t has passed, and τ is the fluorescence lifetime.

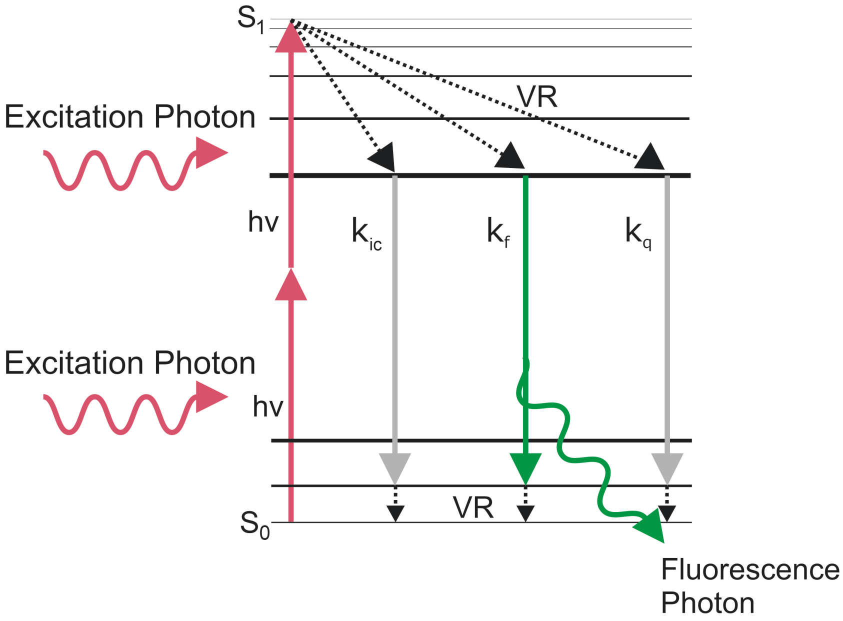

Figure 1.3: Jablonski diagram illustrating two-photon excitation and different pathways of energy release. k_{ic} is the rate constant for internal conversion deactivation, k_f for radiative deactivation, where a fluorescence photon is emitted, and k_q is the rate constant for deactivation induced by a quencher like chloride (chapter 1.2.3).

The fluorescence intensity of a fluorophore is directly proportional to the number of fluorophore molecules. In cells, the exact amount of fluorophore molecules cannot be controlled, making it impossible to gain reliable information about the respective parameter the fluorescent dye is sensitive to, such as the chloride concentration.

A possibility to overcome this problem is to measure the dye‘s fluorescence lifetime τ instead of the fluorescence intensity I, because the fluorescence lifetime of a dye is independent of the amount of dye and the excitation light intensity. Fluorescence lifetime imaging microscopy (FLIM) thus is a well suited tool to measure intracellular and even intraorganellar ion concentrations. It is a non-invasive method and works at a high spatial resolution [56, 57].

The fluorescence lifetime τ describes the characteristic time a fluorophore stays in the excited state (S_1) before it returns to the ground state (S_0) by emission of light. More precisely, it is defined as the time after which a fraction 1 - 1/e of a population of excited fluorophores is deactivated ($t = \tau$ in equation 1.1).

1.2.2 Measuring Fluorescence Lifetimes via Time-Correlated Single Photon Counting

The fluorescence lifetime of a fluorophore can be measured by time-correlated single photon counting [58, 59]. A pulsed laser with defined wavelength, pulse length (50 fs -200 ps), and high pulse frequency (MHz) generates a train of photon pulses, which excite the fluorescent sample. The time interval between the excitation pulse and the registration of the first detected fluorescence photon is measured repeatedly and collected in a histogram (figure 1.4). The plotted fluorescence lifetimes can usually be described by the best fit of a sum of exponential functions, from which the average fluorescence lifetime (τ_{mean}) is calculated.

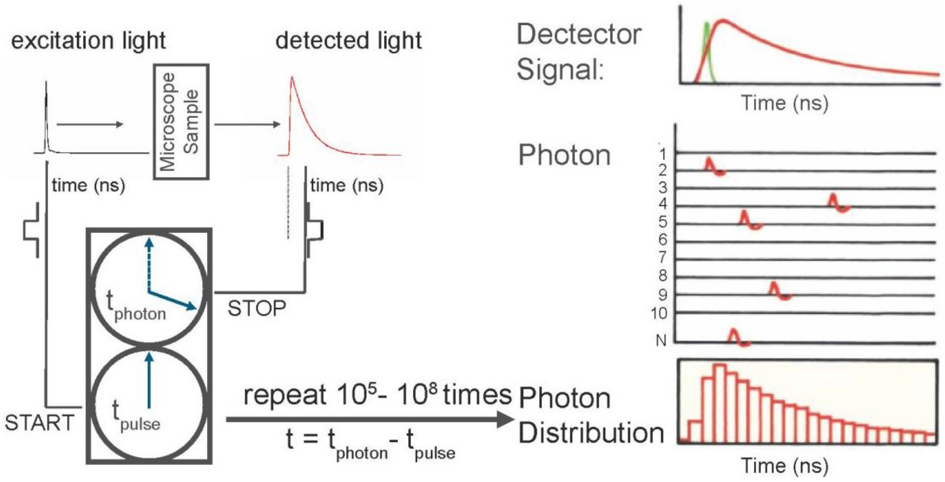

Figure 1.4: **Illustration of TCSPC.** In TCSPC τ_{mean} is determined by detecting single photons and measuring the time between excitation of the fluorophore and detection of emitted photons (scheme modified from [59]).

1.2.3 The Chloride-Sensitive Fluorescent Dyes MEQ and SPQ

MEQ (6-methoxy-N-ethylquinolinium iodide) and SPQ (6-methoxy-N-(3-sulfopropyl)-quinolinium) are quinoline derivatives with chloride sensitive fluorescence properties [60, 61]. The chloride sensitivity results from collisional quenching of the dye's fluorescence by chloride ions. When the excited fluorophore collides with a chloride ion, a short-term complex is formed (picoseconds), in which the probability of non-radiative decay is largely increased, so it is very likely that the fluorophore returns to the ground state without the emission of fluorescence light (see most right deactivation pathway in figure 1.3). Hence, the fluorescence lifetime τ – and also the fluorescence intensity I – of MEQ and SPQ are inversely proportional to the chloride concentration:

$$\frac{I_0}{I} = \frac{\tau_0}{\tau} = 1 + K_{SV}[Cl^-] \tag{1.2}$$

K_{SV} is the Stern-Volmer constant and τ_0 and I_0 the fluorescence lifetime and intensity, respectively, in the absence of quenchers. These parameters are fluorophore-specific and depend on the surrounding environment, because MEQ and SPQ are not only quenched by chloride but also by other halides and anions. Although the physiological concentrations of these non-chloride ions are low compared to physiological chloride concentrations, their influence is not negligible, so the parameters should be determined in the particular environment, i.e. cell-type.

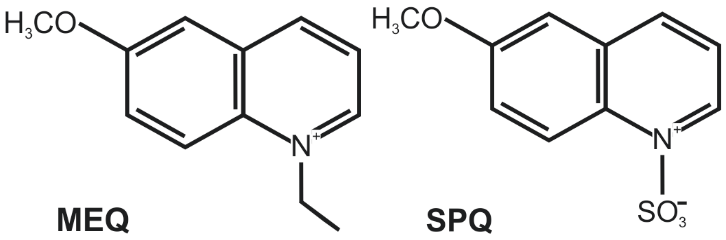

(a) (b)

Figure 1.5: Chemical structures of (a) MEQ and (b) SPQ.

1.3 pH Imgaging

1.3.1 Ratiometric Fluorescence Microscopy

As mentioned before, the fluorescence intensity of a dye is directly proportional to the number of dye molecules, making it impossible to gain reliable information about the parameter the dye is sensitive to by simply measuring the fluorescence intensity, if the the exact amount of dye molecules cannot be controlled.

Besides reading out the fluorescence lifetime instead of the intensity, as it is done in case of SPQ and MEQ in this work, this problem can also be overcome using ratiometric fluorescence microscopy. Here, the fluorescence intensities of two dyes are measured simultaneously. Only one of these dyes is specifically sensitive to the parameter of interest, while the fluorescence intensity of the second dye is insensitive. Hence, the second dye serves as a reference to compensate for effects which are not related to changes of the parameter of interest, e.g. variations of the amount of dye. Accordingly, the ratio of the fluorescence intensities of the sensitive and the insensitive dye directly correlates with the parameter of interest.

1.3.2 The pH-Sensitive Fluorescent Dye Oregon Green 488 Coupled to Dextran

Dextrans are polysaccharides (figure 1.7) and not membrane-permeable, but enter the cells via the endocytic pathway and accumulate within the lysosomes after a few hours (figure 1.6). Because of this feature, dextrans can also be used as lysosomal markers.

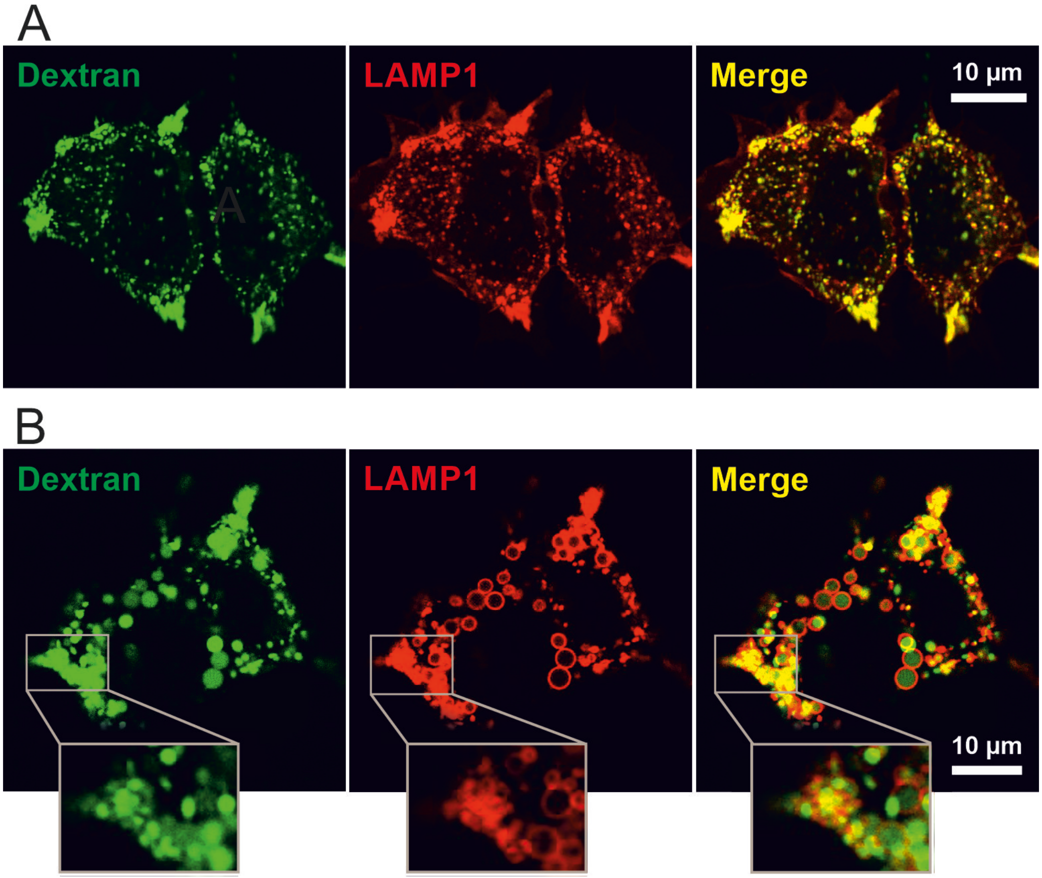

Figure 1.6: **Colocalization of dextran with the lysosomal associated membrane protein 1 (LAMP1).** (A) Confocal images of fixed HEK293T cells, transfected with the lysosomal associated membrane protein 1 (LAMP1) and loaded with dextran (6h, chased overnight). Dextran colocalizes with LAMP1 (Pearson's coefficient of 0.87, analyzed with the JACoP plugin in Fiji by ImageJ [62, 63]), indicating an accumulation of dextran within the lysosomes. (B) After increasing the lysosomal size using YM-201636 (chapter 2.4), the exact localization of LAMP1 and dextran can be resolved. While LAMP1 is located in the lysosomal membrane, dextran is placed in the lumen. (Here, with 0.60 the Pearson's coefficient is of course lower.)

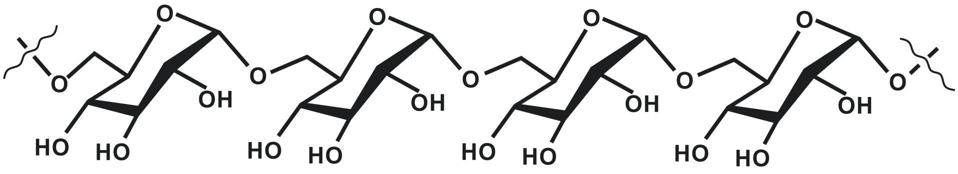

Figure 1.7: Chemical structure of dextrans.

To measure the lysosomal pH, the pH-sensitive dye oregon green 488, coupled to dextran (OG-dextran), is used. The fluorescence intensity of this dye decreases with decreasing pH. Tetramethylrhodamine, coupled to dextran (TMR-dextran), serves as reference for ratiometric pH-measurements, since its fluorescence intensity is not affected by changes in the pH [19], and its fluorescence spectrum is well separated from that of oregon green 488.

Chapter 2

Materials and Methods

2.1 Chemicals and Materials

All chemicals were purity grade *pro analysis* and were obtained from several companies listed in chapter 2.18. Solutions and buffers were prepared with bi-distilled water and filtered with a 0.22 µm pore size filter (Millipore) for sterilization.

2.2 Cell Culture

2.2.1 Maintenance of HEK293T Cells

HEK293T cells, which are modified HEK293 cells (derived from human embryonic kidney, Sigma), were cultured in DH10, Dulbecco's Modified Eagle Medium (DMEM, Gibco), supplemented with 10% FBS (Gibco) and 1% Pen/Strep (100x, ThermoFisher Scientific), and were kept in an incubator at 37°C and 5% CO_2. Cells were split twice a week, when a confluency of 90%-100% was reached.

2.2.2 Transient Transfection

For most of the DNA constructs used in this work, transfection was done using the calcium-phosphate method. In these cases, cells were first transfected and then split the next day and seeded on coverslips for experiments.

For some DNA constructs the transfection with calcium-phosphate was not sufficient, or the cells did not survive the following two days until experiments. In these rare cases, the cells were first split and seeded on coverslips and were transfected the next day, i.e. one day before experiments, using the PEI MAX transfection technique.

Plasmid DNAs used for transfections in this study are listed in table 2.9.

Calcium-Phosphate Transfection

Two to three days before experiments, HEK293T cells were transiently transfected using the calcium-phosphate method, where calcium phosphate-DNA precipitates bind to the surface of the cells and enhance uptake of the DNA via endocytosis [64].
Briefly, 0.5-2.0 µg DNA in TE-Buffer was diluted in ddH_2O to a final volume of 124 µl and mixed with 41 µl $CaCl_2$ (124 mM final concentration). Then, 165 µl 2x HEBS (274 mM NaCl, 40 mM HEPES, 12 mM Glucose, 10 mM KCl, 1.4 mM $Na_2HPO_4(2\ H_2O)$, pH 7.05) were added dropwise under agitation. After 20 min, the precipitate was added dropwise to the cells in a 5 cm dish and was gently mixed with the medium. Cells were washed with PBS/EDTA after 20-22 h to remove the precipitate and were split afterwards (chapter 2.2.3).

PEI MAX Transfection

For some DNA constructs (Arch3, SLC26A11) the DNA was introduced into the HEK293T cells by transfection with polyethylenimine (PEI). PEI is a stable cationic polymer, which condenses the DNA into positively charged particles, that bind to the anionic surface of the cell and are then endocytosed [65, 66].

The following protocol was used for the transfection of cells in three wells of a 24-well plate (Greiner Bio-One). In a first tube, 1 µg DNA was diluted in OptiMEM (Gibco) to a final volume of 75 µl. In a second tube, 5 µl of the PEI MAX (1 mg/ml) solution (Polysciences Inc.) was mixed with OptiMEM again to a final volume of 75 µl. After approx. 2 min, the content of the second was added to the first tube and mixed by pipetting up and down several times. After 15 min of incubation at room temperature (RT), 50 µl of the mixture was added to 500 µl medium in each of the three wells. The medium was changed after 8 h, and experiments were performed the next day.

2.2.3 Splitting and Seeding Cells

Before splitting, cells were washed with wash-PBS (or, in case of calcium-phosphate transfected cells, with PBS/EDTA) to remove the medium, which would otherwise neutralize the activity of Trypsin. 1 ml of 0.05% Trypsin/EDTA (Gibco) was added for 2-5 min to the cells, which were then triturated with a sterile one-way-pipette. The singularized cells were seeded on glass coverslips coated with 0.1 mg/ml poly-L-lysine (Sigma) in a 24-well plate (Greiner Bio-One), containing 500 µl DH10 medium per well.

With the exception of pH measurements and PEI MAX transfected cells, experiments were performed the next day. In case of pH measurements, cells were loaded with the dextrans the day after splitting (chapter 2.3.3). In case of PEI MAX transfection, cells were transfected the day after splitting, and thus, in these cases, experiments were performed two days after splitting and seeding the cells.

For experiments, the medium was replaced by extracellular solution (ES, table 2.6), if not otherwise noted, and exposed to air atmosphere at room temperature (for confocal microscopy) or 37°C (for FLIM experiments and pH measurements).

2.3 Loading of Cells with Fluorescent Dyes

2.3.1 SPQ

SPQ has a very low membrane permeability because of the fixed positively charged nitrogen on the quinoline-ring (figure 2.1 a), but it can be loaded into the lysosomes non-invasively via the endocytic pathway.

A 100 mM stock of SPQ (6-methoxy-N-(3-sulfopropyl)quinolinium, Invitrogen, Thermo Fisher Scientific) dissolved in DH10 was freshly prepared one day before experiments and kept in the dark at 7°C.

HEK293T cells were incubated in DH10 supplemented with 20 mM SPQ for 2 h at 37°C. 20 min before experiments, the cells were washed and incubated in fresh medium without SPQ (chasing step).

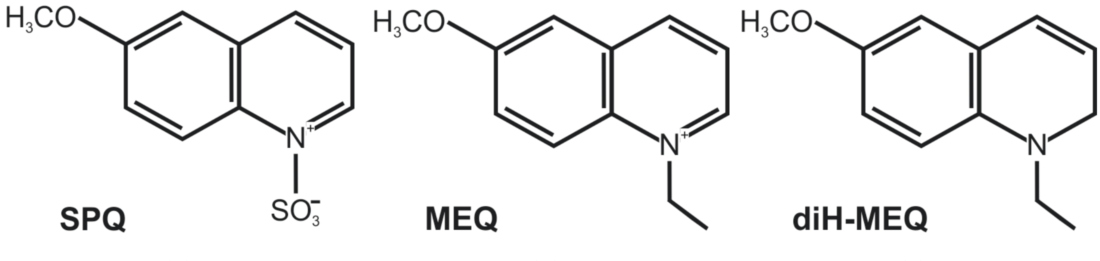

(a) (b) (c)

Figure 2.1: Chemical structure of (a) SPQ (b) MEQ and (c) diH-MEQ.

2.3.2 MEQ

Like SPQ, MEQ (6-methoxy-N-ethylquinolinium iodide) is not membrane permeable, due to its positively charged nitrogen (figure 2.1 b). However, the same approach used for loading the lysosomes with SPQ was not successful for MEQ. Instead, MEQ was rendered cell-permeable by masking the positively charged nitrogen, i.e. reducing MEQ to the Cl^--insensitive diH-MEQ (6-methoxy-N-ethyl-1,2-dihydroquinoline, figure 2.1 c). This was done by our colleagues from INM-5 according to the protocol described in Biwersi et al. [1].

Being able to cross the cell membrane as well as intracellular membranes, diH-MEQ fills the cytosol and the cell organelles, including the lysosomes, non-invasively via diffusion. It rapidly is reoxidized to the Cl^--sensitive MEQ within the cytosol and the cell organelles, where it is then trapped.

To avoid too much oxidation of diH-MEQ to MEQ before loading of the cells, aliquots of diH-MEQ were kept in a -80°C freezer.

For loading of HEK293T cells, diH-MEQ was diluted in ES immediately after thawing, by pipetting up and down several times, and added to the cell medium to a final concentration of 2 mM. After 20 min of incubation at 37°C, cells were washed with ES and transferred to the measuring setup.

2.3.3 OG-Dextran and TMR-Dextran

Oregon green 488 dextran (OG-dextran; 10 000 MW, anionic, Invitrogen, Thermo Fisher Scientific) and tetramethylrhodamine dextran (TMR-dextran; 10 000 MW, neutral, Invitrogen, Thermo Fisher Scientific) were dissolved in PBS to a final concentration of 10 mg/ml, and aliquots were kept at -20°C.

HEK293T cells were loaded with 0.25 mg/ml of each of the dextrans in DH10 for 7 - 8 h at 37°C the day before experiments. After that, cells were washed and incubated in fresh medium without dextrans (chasing step).

It has been shown that after a chasing time of 2 h, most of the dextran is already accumulated within the lysosomes. However, to further decrease the amount of early endosomes loaded with dextran and increase the number of stained lysosomes, a longer chasing time is recommended, which is why an overnight chase was implemented [67].

2.4 Increasing the Lysosome Size with YM-201636

For some experiments, HEK293T cells were treated with 0.8 µM YM-201636 (Cayman Chemical Company) in DH10 overnight to increase the lysosomal size [68, 69].

YM-201636 is cell-permeable and selective inhibitor of PIKfyve, an enzyme, which phosphorylates PI(3)P (phosphatidylinositol3-phosphate) to PI(3,5)P2 (phosphatidylinositol3,5-biphosphate). PI(3,5)P2 is present in the lysosomal membrane, and its depletion leads to defective fission of vesicles and hence to an enlargement of vesicular size [70, 71].

To avoid a reversion of this effect, YM-201636 was kept on the cells while loading the cells with the fluorescent dyes and during chasing steps.

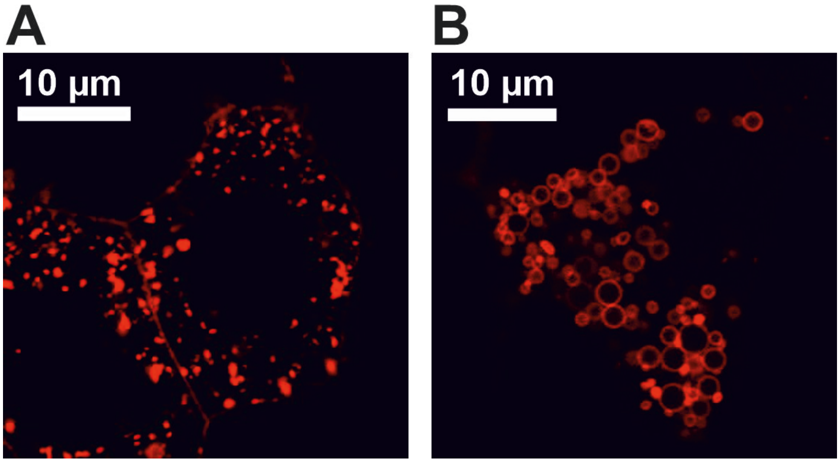

Figure 2.2: **YM-201636 increases the lysosome size.** (A) Confocal image of HEK293T cells transfected with the lysosomal associated membrane protein 1 (LAMP1, fused to the fluorescence protein mCherry). (B) Confocal image of HEK293T cells transfected with LAMP1 and treated with YM-201636 overnight. The lysosome size is increased in these cells.

2.5 Fluorescence Lifetime Imaging Microscopy

2.5.1 Two-Photon Fluorescence Microscopy

For the aquisition of data, glass-coverslips with HEK293T cells, loaded with diH-MEQ or SPQ, were transferred to a 5 cm petri dish or (in case of calibration or blocker experiments) to an imaging chamber and placed on the stage of an upright scanning fluorescence microscope (A1 MP; Nikon Instruments Europe), equipped with a 25 x water-immersion objective (NA 1.1, working distance 2.0 mm; Nikon). The stage was enclosed by a climate chamber (Okolab), which maintained the temperature at 37°C for all experiments.

MEQ or SPQ were excited by 100 fs light pulses with a wavelength of 750 nm by two-photon excitation. The laser pulses, generated by a mode-locked Titanium-Sapphire laser (MaiTai DeepSee, output power 2.3 W at 750 nm, Newport Spectra Physics) at a frequency of 80 MHz, were directed onto the cells through the lens with reduced power. The focal spot was scanned over the sample with a frame rate of 0.25 images/sec and a scan size of 512 x 512 pixels. Depending on the chosen zoom factor between 6% and 10%, the pixel sizes ranged from 0.10 µm to 0.17 µm.

A bandpass filter (BP445, lambda 400 - 490 nm, Omega Optical) in front of the GaAsP hybrid photodetector (HPM-100-40, Becker & Hickl) was used to diminish autofluorescence and, in case of transfected cells, the fluorescence of proteins like RFP (mCherry, mKate2), YFP, or GFP. These proteins, which were used for the identification of transfected cells, were excited by tuning the excitation wavelength to 920 nm. The emission of the fluorescence proteins was filtered with appropriate bandpass filters (for RFP: 595AF60, lambda 565 - 637 nm, Omega Optical; for GFP: FF02 534/30-25, lambda 519.5 – 549.5 nm, Semrock) to diminish MEQ or SPQ fluorescence.

For the last few experiments, the microscope was replaced by a Zeiss-microscope (LSM880) with a 20x Objective (NA 1.0, working distance 2.1 mm; Zeiss), and the laser was replaced by a tunable laser (InSight X3, Spectra Physics). The results were reproducible with the new setup.

Beside two-photon excitation, the new setup also offers the possibility for one-photon excitation, which was used here for the identification of transfected cells. GFP was excited with a 488 nm Argon-ion laser, RFP with a 561 nm DPSS laser, and iRFP713 was excited with a 633 nm HeNe laser. The respective emission signals were detected after filtering with variable bandpass filters (GFP: 499-541 nm, RFP: 570-642 nm; iRFP713: 670-750 nm), using a PMT or a GaAsP-PMT detector.

2.5.2 Time-Correlated Single Photon Counting and Analysis of Data using SPCImage

Fluorescence lifetimes were measured via time-correlated single photon counting (TCSPC, Simple-Tau 152; Becker & Hickl). The fluorescence was averaged over a total scanning time of 80 sec, which corresponds to 20 frames with a pixel dwell time of 12.1 µsec per pixel and frame.

Data were analyzed using the software SPCImage (Version 6.0, Becker & Hickl), which computes fluorescence decay curves $I(t)$ in every pixel of the image by iterative reconvolution of the instrument response function $IRF(t)$ with a bi-exponential model function $f(t)$:

$$I(t) = IRF(t) * f(t) \tag{2.1}$$

with

$$f(t) = a_1 e^{-t/\tau_1} + a_2 e^{-t/\tau_2} \tag{2.2}$$

where τ_i are the lifetimes of the exponential components and a_i the respective amplitudes.

A bi-exponential model function was used, because for both MEQ and SPQ this resulted in a better description of the measured data, compared to a mono-exponential fit (see figure 2.3 D). A reason for this might be that MEQ and SPQ probably have two preferential sites for collisions with chloride-ions (and other quenchers). For MQAE (1-(Ethoxycarbonylmethyl)-6-methoxyquinolinuim bromide), which is another quinolinium-based fluorescent chloride sensitive dye, this was shown by Gensch et al. [72] by molecular dynamics (MD) simulations of MQAE in water in the presence of 0.5 M NaCl. These two preferential sites might have different efficiencies for the formation of a collisional complex or different probabilities for internal conversion during the existence of the collisional complex, which would explain the bi-exponential fluorescence decay.

The amplitude-weighted average fluorescence lifetimes τ_{mean} were used for further analysis [73]:

$$\tau_{mean} = \frac{a_1\tau_1 + a_2\tau_2}{a_1 + a_2} \tag{2.3}$$

The number of photons collected per pixel was above a critical minimum of 2000 photons [74] when a bin-factor b of 1 was used. The bin-factor b defines the number of combined pixels n used for the calculation of the fluorescence lifetimes:

$$n = (2b + 1)^2, \tag{2.4}$$

so the used bin-factor of 1 corresponds to 9 combined pixels.

To avoid the inclusion of pixel clusters (bin 1), where the total number of photons is below 2000, the threshold of the minimum number of photons in the peak of a fluorescence curve was set to at least "35" in SPCImage.

For further analysis, the dataset for τ_{mean} and pixel intensities were exported as matrix text image files from SPCImage. In these text files, τ_{mean} or the number of photons for every pixel is stored as grey values, which were then further processed in Fiji by ImageJ [62] (chapter 2.9).

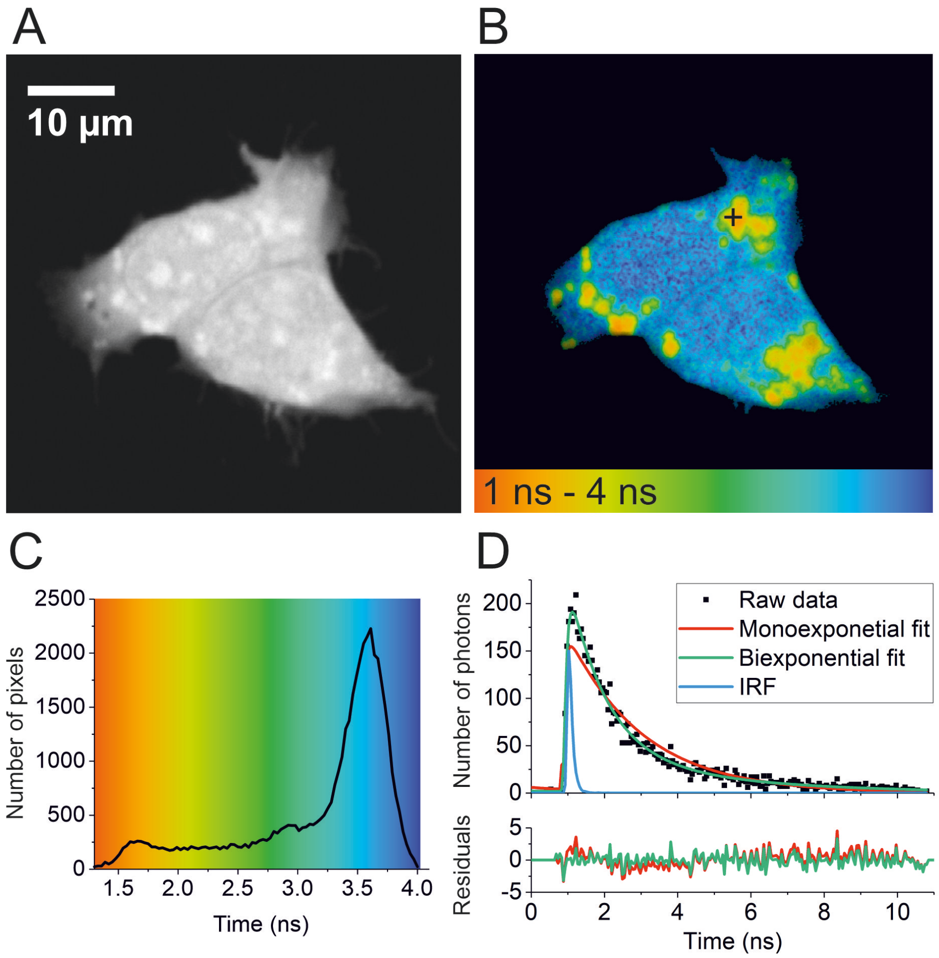

Figure 2.3: **Mono- vs. biexponential fit.** (A) Fluorescence intensity image of MEQ in HEK293T cells treated with YM-201636. (B) Corresponding fluorescence lifetime image showing τ_{mean} from 1 ns to 4 ns, represented by a color code. (C) Distribution of the fluorescence lifetimes in image B. (D) Comparison of mono- and biexponential fit of the selected pixel in B (black cross). The biexponential fit leads to a better description of the measured data (the same applies to SPQ).

2.6 Determination of Chloride Concentrations

2.6.1 Calibration of MEQ and SPQ in HEK293T Cells

To determine absolute chloride concentrations, a calibration has to be performed to relate the measured fluorescence lifetimes τ to specific chloride concentrations within the cytosol and lysosomes.

Since MEQ and SPQ are not only quenched by chloride but also by other anions, which are present in different cell types to different amounts, the calibration has to be carried out within the cell type of interest to determine the cell specific Stern-Volmer constant.

After loading the cells with diH-MEQ or SPQ (and after the chasing step), cells were incubated for 1 h at 37°C in calibration solutions (CS) with a high potassium concentration of 122.4 mM and different chloride concentrations ranging from 10 to 140 mM. The CS was supplemented with a variety of ionophores and blocking agents (see table 2.7). The use of Nigericin, which exchanges K^+ and H^+, and Tributyltin, which is a Cl^- and OH^- antiporter, together with a high extracellular potassium concentration has been shown to equalize intra- and extracellular chloride concentrations [58, 75, 76]. To further solubilize not only the plasma membrane but also the lysosomal membrane, the potassium ionophore Valinomycin, the uncoupler Carbonyl Cyanide m-Chlorophenyl Hydrazone (CCCP), the Na^+/H^+ antiporter Monensin, and the V-ATPase blocker Bafilomycin A1 were added, together with Triton X-100. The CS was kept on the cells also during the measurements.

For each chloride concentration, the calibration was repeated at least three times. The obtained calibration data were used for all experiments with SPQ or MEQ, respectively, to determine the chloride concentrations as explained in the following chapter.

2.6.2 Calculation of Chloride Concentrations from Fluorescence Lifetimes of MEQ and SPQ

The average inverse fluorescence lifetimes $1/\tau$ obtained from the calibration were plotted over the respective chloride concentrations with the software OriginPro 2017 (OriginLab Corporation).

Since the collisional quenching of MEQ and SPQ by chloride ions results in an inverse linear relationship between τ and $[Cl^-]$ (equation 1.2), a linear regression was made using the weighted least square method.

$$\frac{1}{\tau} = \frac{1}{\tau_0} + \frac{K_{SV}}{\tau_0}[Cl^-] \tag{2.5}$$

The inverse intercept of this linear function equals τ_0, from which, together with the slope, the corresponding Stern-Volmer constant K_{SV} was calculated.

The chloride concentrations were calculated from the measured fluorescence lifetimes τ by equation 2.6:

$$[Cl^-] = \frac{\frac{\tau_0}{\tau} - 1}{K_{SV}}. \tag{2.6}$$

2.7 Ratiometric Fluorescence Microscopy

Ratiometric fluorescence microscopy was performed on an upright scanning fluorescence microscope (LSM880; Zeiss), equipped with a 20x water-immersion objective (NA 1.0, working distance 2.1 mm; Zeiss). Cells loaded with OG- and TMR-dextran were transferred to an imaging chamber and placed on the microscope stage, enclosed by a climate chamber (PeCon), which maintained the temperature at 37°C during all experiments using a heating unit (XL S; Zeiss).

OG-dextran was excited with a 488 nm Argon-ion laser and TMR-dextran with a 561 nm DPSS laser. Emission signals were detected simultaneously after filtering with a 499-541 nm and a 570-642 nm (variable) bandpass filter, using a PMT and a GaAsP-PMT detector, respectively. To avoid saturation of the signal, the laser power was adjusted at the highest pH (calibration solution at pH 7.3), since the fluorescence intensity of OG-dextran decreases with decreasing pH. The pinhole size was set to 30.4 µm in diameter. These settings remained unchanged during all measurements, including the calibration.

For pH measurements with transfected cells, a fluorescence tag was used which did not interfere with the OG- or TMR-fluorescence. The fluorescence protein iRFP713 is well suited, since it is not excited at 488 nm and hardly excited at 561 nm [77]. Furthermore, its emission spectrum starts at 650 nm, so any iRFP emission would be blocked by the filter range used for OG and TMR detection.

For identification of transfected cells, iRFP713 was excited with a 633 nm HeNe laser, and the emission signal was filtered with a 670-750 nm bandpass filter and detected by a PMT detector.

2.8 Determination of Lysosomal pH

2.8.1 Calibration of I_{OG}/I_{TMR}-Ratio in Lysosomes of HEK293T Cells

To determine absolute pH values, the ratio of the fluorescence intensities of OG- and TMR-dextran, I_{OG} and I_{TMR} respectively, has to be related to specific pH values in the lysosomes of living cells.

For this, a calibration was done according to the protocol described in Johnson et al. [19]. To adjust the lysosomal pH (pH$_{lyso}$) to different known external pH (pH$_{ex}$), calibration solutions (CS, table 2.8) were used, which contained 10 µM of the K^+/H^+ exchanger Nigericin and 10 µM of the Na^+/H^+ antiporter Monensin to dissipate proton gradients across the membranes. To prevent the transmembrane potassium gradient from affecting the proton gradient, the CS also contained high [K^+] (122.4 mM) [78]. This ensures that the luminal pH of the lysosomes reaches a value that closely approximates that of the cytosol, which in turn approximates the pH of the CS [79].

10 different CS with pHs ranging from 3.5 to 7.3 were used for the calibration. The pH of the solutions was adjusted with NaOH and HCl at 37°C (WTW pH 197 pH-meter; SenTix 41 pH-electrode) and kept stable by different buffers depending on the respective pH: For solutions below pH 5.5, potassium acetate buffer was used; MES buffer was used for solutions between pH 5.5 and 6.7; HEPES buffer was used for solutions set above pH 6.7.

To ensure the adjustment of pH$_{lyso}$ to pH$_{ex}$, cells were incubated for at least 3 minutes in CS before recordings. After this time, the I_{OG}/I_{TMR}-ratios were stable. For each day of experiments, an individual calibration was performed, and for every preset pH, the OG- and TMR-intensities of at least 25 cells were measured.

Unlike Johnson et al., who performed the whole calibration in one single dish [19], in this work only two different pH values per dish were sequentially calibrated. Since the HEK293T cells started to look unhealthy after 3 - 6 minutes in CS with pH values below approx. 4.5, they were sequentially bathed first in a CS with a pH higher than 5 and then in a CS with a pH below 5. Afterwards, a new dish of HEK293T cells was used for the next two pH values. This way, cells looked healthy during the whole calibration.

For every image, the background intensity was determined and subtracted from the average intensities in the ROIs (see chapter 2.9), before calculating the ratios.

2.8.2 Calculation of Lysosomal pH from Fluorescence Intensity Ratio of OG- and TMR-Dextran

The ratios of OG- and TMR-fluorescence intensities (I_{OG}/I_{TMR}) obtained from the calibration were plotted versus the respective pH-values in OriginPro 2017 and best fitted by a DoseResponse sigmoidal curve with a variable Hill slope b:

$$\frac{I_{OG}}{I_{TMR}} = A1 + \frac{A2 - A1}{1 + 10^{(pK_a - pH)b}} \tag{2.7}$$

where pK_a is the acid dissociation constant and $A1$ and $A2$ are the minimum and maximum asymptotic values of I_{OG}/I_{TMR} [80].

Using this equation, the I_{OG}/I_{TMR}-ratios calculated from the measured OG- and TMR-intensities I_{OG} and I_{TMR} (again, after subtraction of the background) were converted into pH values.

2.9 Criteria for Data Selection

To determine [Cl$^-$] or pH in the lysosomes, regions of interest (ROIs) were defined in Fiji (ImageJ) [62]. For all experiments, including the calibrations, only the average fluorescence lifetimes or intensities within these ROIs were further analyzed in OriginPro2017. Round and therefore presumably apoptotic or necrotic cells were not analyzed. Further criteria and the methods used to define the ROIs for analysis are listed in the following chapters for MEQ, SPQ and the dextrans.

2.9.1 MEQ

The cytosol was only analyzed if the cell was sufficiently loaded with MEQ, which was determined by the fluorescence intensity at excitation with a reasonable laser power. In general, for fluorescence lifetime measurements, pixel clusters (bin-factor 1) with counts below approx. 2000 photons were not analyzed.

In experiments investigating lysosomal [Cl$^-$] with MEQ, the lysosomal size was always increased by treating the cells with YM-201636. The lysosomes were identified in the image containing the fluorescence lifetime values, since the intensities of the MEQ signal in the lysosome and the cytosol were very similar and therefore indistinguishable (figure 2.4 A). The fluorescence lifetime images revealed vesicular structures within the cell, with considerably shorter fluorescence lifetimes than in the cytosol (figure 2.4 B). These round, large vesicular structures within the cell were identified as lysosomes.

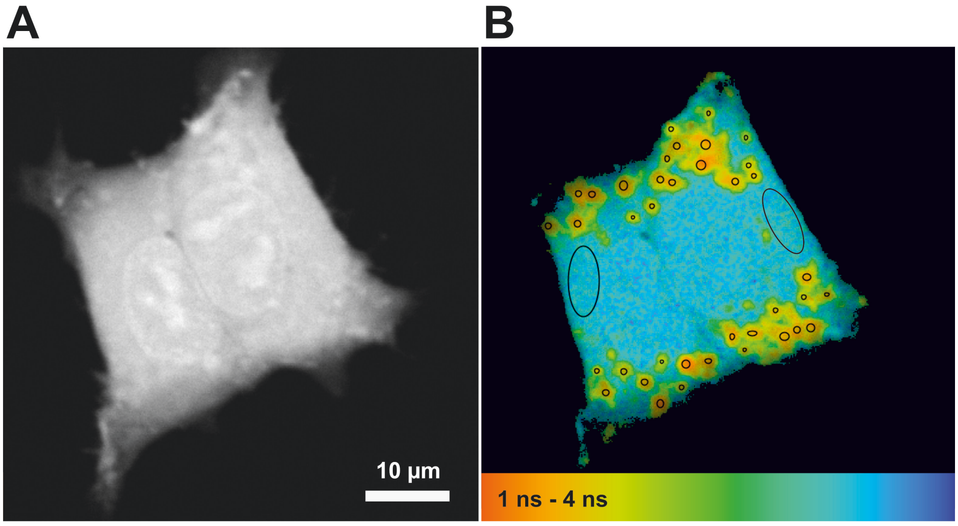

Figure 2.4: **Selection of ROIs in case of MEQ.** (A) Fluorescence intensity image of two HEK293T cells with MEQ (after treatment with YM-201636). (B) Identification of lysosomes in the fluorescence lifetime image of MEQ. The ROIs on the lysosomes (black circles) were not set exactly along the lysosomal membrane, but slightly shifted towards the inside of the lysosome. The ROIs on the cytosol were set in areas of the cell without lysosomal signal.

Only vesicular structures with a diameter larger than approx. 0.8 µm were analyzed, because for smaller vesicles the luminal signal could not be sufficiently separated from the cytosolic signal anymore, due to the used binning factor of 1, that combines the fluorescence lifetimes of 9 pixels in SPCImage (chapter 2.5.2), and movements of the smaller lysosomes during the acquisition time.

ROIs were set by hand using the oval selection tool in Fiji. To avoid a distortion of results by the cytosolic signal, the ROIs were not set exactly along the lysosomal membrane, but were slightly shifted towards the inside of the lysosome (figure 2.4 B). This is important, since, due to the binning, the pixels in close proximity to the lysosomal membrane contain partially signal contribution from the lysosome surrounding cytosol.

2.9.2 SPQ

Round vesicular structures within the cell with a diameter larger than approx. 0.4 µm were identified as lysosomes. Due to the limited spatial resolution, smaller structures could not be resolved properly. Pixel clusters (bin-factor 1) with counts below approx. 2000 photons were not analyzed. The ROIs were set by hand using the oval selection tool in Fiji as described for MEQ in the previous subchapter (Figure 2.5).

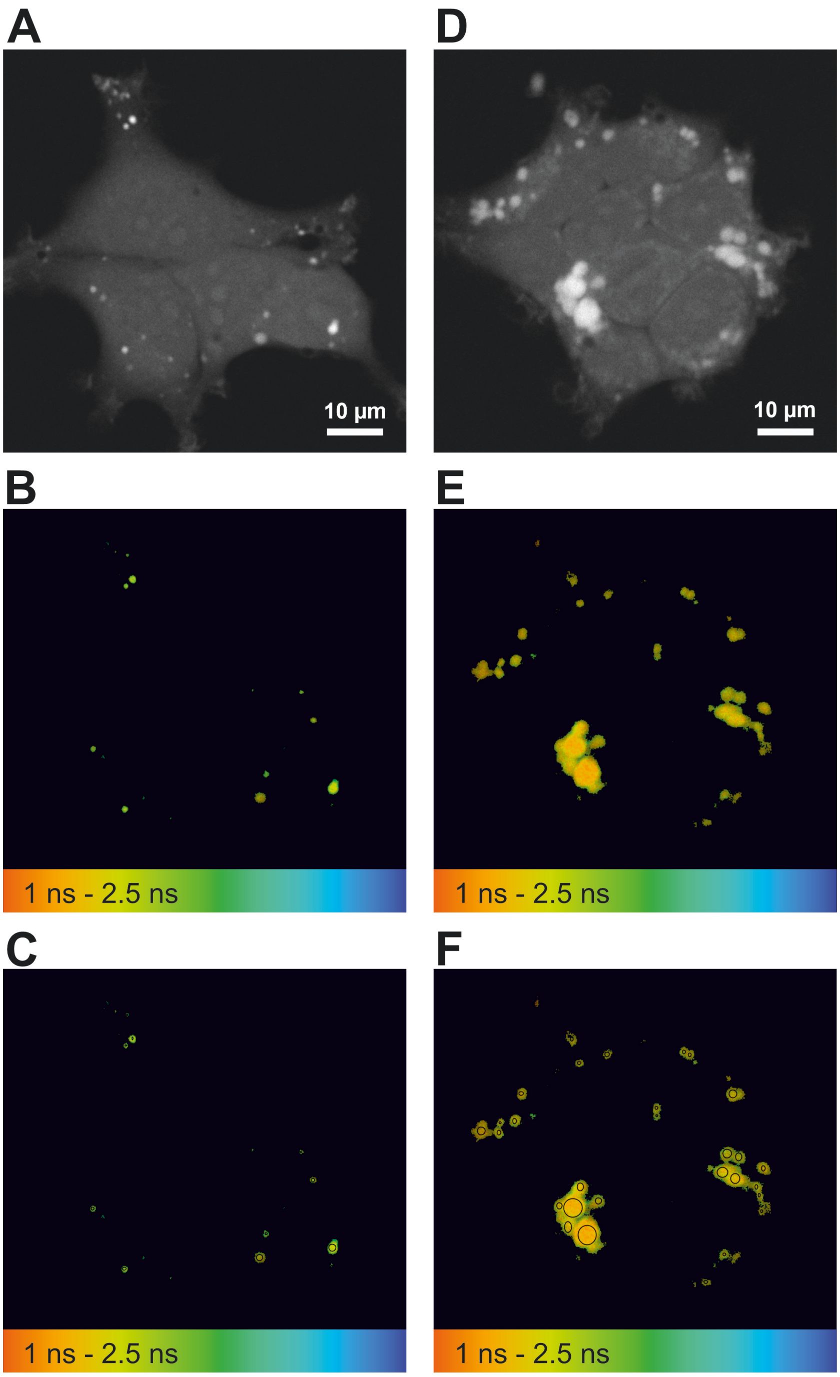

Figure 2.5: **Selection of ROIs in case of SPQ.** (A) Fluorescence intensity image of HEK293T cells loaded with SPQ (without YM-201636) and (B) corresponding fluorescence lifetime image. (C) Selected ROIs in the fluorescence lifetime image (black circles). (D) Fluorescence intensity image of HEK293T cells loaded with SPQ (after treatment with YM-201636) and (E) corresponding fluorescence lifetime image. The vesicular structures are larger. (F) Selected ROIs in the fluorescence lifetime image (black circles).

2.9.3 Dextrans

The high fluorescence intensities of OG and TMR allowed the use of a small pinhole (diameter 30.4 µm). The thus improved resolution in turn allowed the analysis of vesicular structures with smaller diameters than it was the case for SPQ. Instead of drawing the ROIs manually, in Fiji a gaussian blur filter with a radius of 1.0 was applied in the fluorescence intensity image of OG-dextran to increase the difference between signal and background noise. After that, the "Find Maxima"-plugin was used to identify single lysosomes. The minimal value for the noise tolerance was adjusted by visual inspection for each image in a way that only round spots with high fluorescence intensities compared to the background were selected which would also have been chosen manually (figure 2.6).

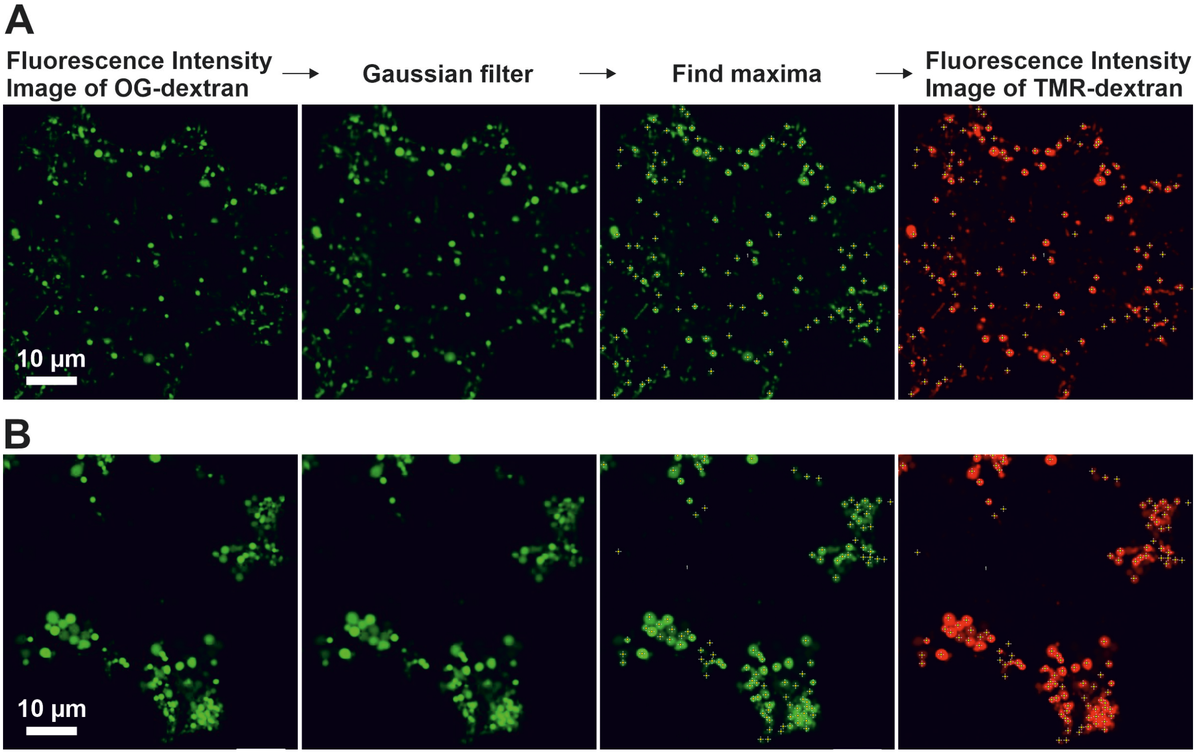

Figure 2.6: **Selection of ROIs in case of OG- and TMR-dextran.** Fluorescence intensity images of lysosomes loaded with OG-dextran ((A) without YM-201636 and (B) after treatment with YM-201636). ROIs were not selected manually. Instead, first a gaussian filter and after that the "Find maxima" plugin were applied in Fiji on the intensity image of OG-dextran. The coordinates of the fluorescence intensity maxima in the OG-dextran image were then transferred to the intensity image of TMR-dextran.

This approach was used not only for lysosomes of normal size but also after treatment with YM-201636, because it was significantly faster and the resulting average intensities from this method and manual selection were similar. The ROIs, defined in the intensity image of OG-dextran, were then also transferred to the TMR-dextran image, because all vesicles with OG-signal also had TMR-signal (and vice versa).

For every image, the background intensity was determined in an area of the image without a cell and subtracted from the average intensities in the ROIs, before calculating the I_{OG}/I_{TMR}-ratios.

2.10 Statistical Analysis

All [Cl$^-$] and pH values are presented as boxplots, which show the mean value, the median, the lower and upper quartile, and the region within 1.5 IQR (interquartile range) (figure 2.7). Values are given as mean ± standard deviation (SD).

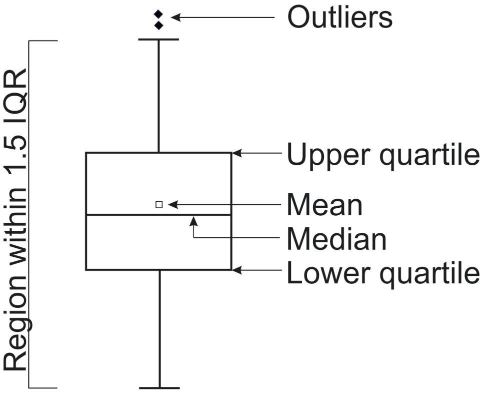

Figure 2.7: **Features of boxplots.**

All different experimental conditions were measured on at least three different days and therefore with at least three different coverslips. For statistical analysis, the sample size (N), which is equal to the number of independent experimental units, is often given by single cells. However, cells in a culture dish or on a coverslip influence each other, e.g. by forming cell-to-cell connections, releasing signalling molecules, and competing for nutrients in the media. Thus, instead of the cells, the coverslips were used as appropriate independent experimental units on which statistical analysis was performed.

Statistical analysis was done using SigmaPlot (Version 12.3). For normally distributed values, results were compared using a two-tailed student's t-test. When an equal variance test failed or the dataset was not normally distributed, a Mann-Whitney Rank Sum test was used instead. A normal distribution of values was examined by Shapiro-Wilk tests. The level of significance is indicated by asterisks (***, $p < 0.001$; **, $p < 0.01$; *, $p < 0.05$). All determined values and test results are listed in the tables in chapter 3.11.

2.11 Confocal Microscopy

Confocal images were acquired at room temperature using a Leica TCS SP5 II inverted microscope, equipped with a 63x oil immersion objective.

The following table shows the excitation wavelengths and variable bandpass filters used for filtering the emission signals of different fluorescence tags:

Table 2.1: **Excitation wavelengths and bandpass filters applied for different fluorescence proteins.**

Fluorescence protein	**Excitation wavelength**	**bandpass filter**
GFP	488 nm	497 - 522 nm
YFP	514 nm	525 - 545 nm
mCherry	594 nm	610 - 675 nm
mKate2	594 nm	620 - 650 nm
iRFP713	633 nm	703 - 800 nm

When several proteins were imaged simultaneously, well-separable fluorescence tags were chosen and the bandpass filters were adjusted accordingly. Recorded images were edited in Fiji by ImageJ [62].

2.12 Observation of Autophagosome-Lysosome Fusion Using pftLC3

The fusion of lysosomes with autophagosomes, leading to autolysosomes (ALs), was monitored using LC3b (microtubule-associated protein 1 light chain 3 beta) fused to mRFP and EGFP as an autophagosome marker (pftLC3 plasmid # 21074, Addgene). Before fusion with lysosomes, autophagosomes are RFP- and GFP-positive, whereas after fusion, they are RFP positive but GFP negative, because the GFP fluorescence is quenched in the acidic lumen [81]. Hence, the ratio of GFP to RFP fluorescence intensity can be taken as a measure of the extent of autophagosome fusion with lysosomes.

Cells were transfected with pftLC3 and split on glass-coverslips the next day. Two days after transfection, coverslips were transferred to an imaging chamber, and confocal images of the living cells were taken (for excitation wavelengths and bandpass filters see table 2.1, GFP and mCherry). For experiments with additional transfection, iRFP713 was used as a fluorescence tag, since this is well-separable from GFP- and RFP-fluorescence.

The GFP- as well as the RFP-positive vesicles per cell were counted manually. From the relation of GFP- to RFP-positive vesicles the percentage of autolysosomes was determined.

2.13 Knock-Down of Proteins Using shRNA

Removing a specific protein from an otherwise unchanged cell can give useful information about the function and importance of this protein, but the process of genetic knock-out is time-consuming and does not always lead to clear results, considering that cells often compensate the missing protein by upregulating the expression of other proteins. These developmental compensations do not occur when the protein expression is knocked down via RNA interference (RNAi) [82].

RNAi is a process, in which protein expression is inhibited by short, double-stranded RNA molecules, called small interfering RNA (siRNA). These siRNA molecules are designed in a way that they are complementary to the targeted endogenous mRNA. This way, when introduced into the cell, the siRNA molecules bind to the target mRNA and functionally inactivate it, thereby preventing the translation process. This inactivation is achieved by the activity of the endogenous RNA-induced silencing complex (RISC). One strand of the siRNA duplex is loaded into the RISC, which then localizes the strand to the complementary mRNA. The mRNA molecule is subsequently cleaved and degraded by various nucleases [83].

A disadvantage of this method is that the protein expression is only knocked-down until the siRNA is also degraded within the cell. A longer-term solution is the use of small hairpin RNA (shRNA). shRNA are sequences of RNA, which contain two sections that are reversely complementary to each other, so that they form a hairpin structure (figure 2.8). Within the cell, the shRNA is processed to form siRNA. The advantage of shRNA compared to the direct introduction of siRNA is that the sequence of the shRNA can be incorporated into a plasmid vector and integrated into the genomic DNA, which in turn leads to a more permanent knock-down of the target mRNA [83].

The short hairpin targeting sequence for ClC-7, PAC and Sialin (see table 2.2) was inserted into the lentiviral backbone vector FsY1.1 downstream of the human H1 promoter. To identify transfected cells, iRFP sequence was cloned in front of the synapsin promoter (H1-shRNA-FsY1.1-iRFP). In addition, a scrambled shRNA sequence was inserted into the same vector and used as a control.

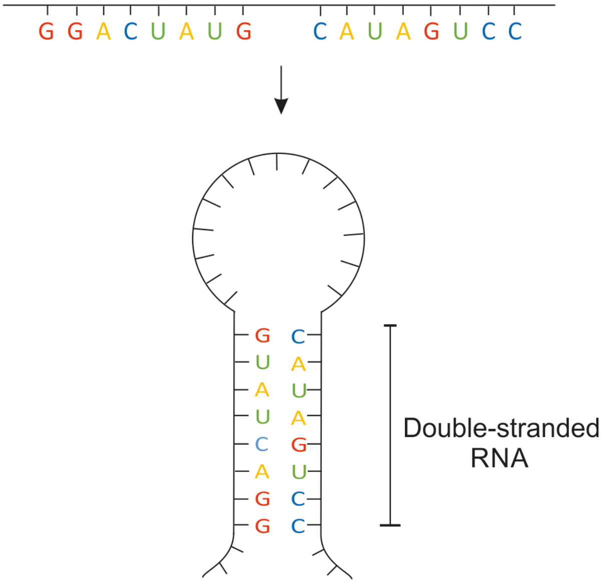

Figure 2.8: **Design of shRNA.** The RNA resulting from the designed plasmid folds up to form a hairpin with a double stranded section.

Table 2.2: **ClC-7, PAC and Sialin shRNA targeting sequences for reduction of the mRNA expression levels in human cells.**

Protein	Sequence of shRNA	Clone ID (Sigma)
ClC-7	tcgagccAGTATGAGAGCTTGGACTATGttcaagaga CATAGTCCAAGCTCTCATACTttttttGGAAAt	NM 001287.4-388s21c1
PAC	tcgagccGAACAAGAGTAGTGAGGACTTttcaagaga AAGTCCTCACTACTCTTGTTCttttttGGAAAt	NM 018252.1-705s1c1
Sialin	tcgagccGCCGTTGCTTTCCTAACTATAttcaagaga TATAGTTAGGAAAGCAACGGCttttttGGAAAt	NM 012434.3-1261s1c1

The efficiency of the knock-down was determined via qPCR (quantitative PCR). Briefly, HEK293T cells were transfected using calcium-phosphate with the plasmid containing the shRNA or the scrambled shRNA sequence. Two days after transfection, the cells were lysed using Trizol reagent (Life Technologies, Thermo Fisher Scientific) and the RNA was isolated according to the RNA isolation protocol by Life Technologies. Then, the isolated RNA was used for first-strand cDNA synthesis, using Superscript III Reverse Transcriptase and following the instructions of the manufacturer (Invitrogen, Thermo Fisher Scientific). Afterwards, the probes for the qPCR were prepared according to the Maxima SYBR Green qPCR Master Mix protocol by Thermo Fisher Scientific. The dye SYBR green fluoresces upon intercalation in double-stranded DNA and therefore allows the quantification of the amount of amplified DNA [84]. Table 2.3 lists the primers used for the qPCR.

The relative amounts of mRNA for the gene of interest is determined using the comparative Ct method (Applied Biosystems, Thermo Fisher Scientific). The Ct (cycle threshold) value of the qPCR describes the cycle of the qPCR, in which the fluorescence exceeds the background fluorescence for the first time. The values are standardized to the expression of the endogenous 18S rRNA (housekeeping gene). This is done for the knock-down cells as well as for the control cells, and the relation between the respective standardized Ct values corresponds to the knock-down efficiency [84].

The resulting knock-down efficiencies for ClC-7, PAC, and Sialin are 73% ± 12%, 77% ± 25%, and 83% ± 21% (table 2.4). These efficiencies are already high and promise a sufficient knock-down of the target proteins in HEK293T cells. However, since the transfection efficiencies are lower than 100%, the dishes used for RNA-isolation did not only contain transfected cells, but also untransfected cells in which the protein expression was not knocked down. These untransfected cells also contribute to the qPCR results and reduce the determined efficiencies. Thus, the real knock-down efficiencies in the transfected cells are expected to be even higher.

Table 2.3: **Sequences of primers used for qPCR.**

Gene	Forward Primer	Reverse Primer
18s	CGCCGCTAGAGGTGAAATTCTTG	GTGGCTGAACGCCACTTGTCC
ClC-7	GCCTTCCGGACGGTGGAGAT	TCCAAACGCCGCTGACACTC
PAC	CAGGTATTGCCTTGTACCCC	CTACATTGACCAGAGGCCAGCTG
Sialin	TCAACAACACTGGGAGGCTTTTGCTC	CCTACTTCATGTTGCCCGACTAGCAGG

Table 2.4: **Knock-down efficiencies of different shRNAs stated by Sigma and determined by qPCR in HEK293T cells.** All values determined by qPCR result from 3 independent transfections (N=3).

Protein	Mean k.d. efficiency stated by Sigma	Mean k.d. efficiency in HEK293T cells
ClC-7	94%	73% ± 12%
PAC	77%	77% ± 25%
Sialin	94%	83% ± 21%

2.14 Simulations

Simulations were performed in Berkeley Madonna, using a mathematical model of lysosomal pH regulation provided by Ishida et al. [4]. The model includes proton leakage, ClC-7 antiporters, Na^+ and K^+ channels, and v-ATPases. It also considers the influence of negatively charged Donnan particles in the lumen and the buffering capacity of the luminal contents. Detailed information can be found in [4].

2.15 Blockers and Ionophores

Table 2.5: **Blockers and ionophores.** With the exception of Nigericin, Tributyltin and 4-Aminopyridin, which were stored at 4°C, the other stock solutions were stored at -20°C. In case of Bafilomycin A1, aliquots were prepared, because repeated thawing and freezing is known to decrease its effect. During the measurement day, the used aliquots were kept on ice.

Blocker	**Concentration**	**Stock**	**Manufacturer**
Nigericin	10 µM	20 mM in EtOH	Sigma
Tributyltin	10 µM	10 mM in ES	Sigma
Valinomycin	10 µM	10 mM in EtOH	Sigma
CCCP	5 µM	50 mM in EtOH	Sigma
Monensin	10 µM	14 mM in EtOH	Sigma
Bafilomycin A1	200 nM	200 µM in DMSO	Calbiotech
Triton X-100	0.015%	2% v/v in ES	Sigma
4-Aminopyridin	400 µM	50 mM in ES	Sigma

2.16 Buffers

Table 2.6: **Extracellular solution (ES), pH adjusted to 7.4 with NaOH at 37°C**

Concentration	**Substance**
140 mM	NaCl
2.4 mM	KCl
10 mM	D-Glucose
10 mM	HEPES
2 mM	$CaCl_2$
1 mM	$MgCl_2$

Table 2.7: **Solution for chloride calibration ($\mathbf{CS}_{Cl}$).** pH was adjusted to 7.4 with NaOH at 37°C. The chloride concentration was varied by partial substitution of NaCl and KCl with $NaNO_3$ and KNO_3.

Concentration	**Substance**
20 mM	NaCl
122.4 mM	KCl
10 mM	D-Glucose
10 mM	HEPES
2 mM	$CaCl_2$
1 mM	$MgCl_2$
10 µM	Nigericin
10 µM	Tributyltin
10 µM	Valinomycin
5 µM	CCCP
10 µM	Monensin
200 nM	Bafilomycin A1
0.015 % v/v	Triton X-100

Table 2.8: **Solution for pH calibration ($\mathbf{CS}_{pH}$).** pH was adjusted to values between 3.5 and 7.3 with NaOH and HCl at 37°C. Potassium acetate was used for pH $<$ 5.5, MES for pH 5.5 to 6.7 and HEPES for pH $>$ 6.7.

Concentration	**Substance**
20 mM	NaCl
122.4 mM	KCl
10 mM	D-Glucose
10 mM	Potassium acetate/MES/HEPES
2 mM	$CaCl_2$
1 mM	$MgCl_2$
10 µM	Nigericin
10 µM	Monensin

2.17 Clones Used for Transfections

Table 2.9: **All plasmids used for transfections and their respective institute-intern clone numbers.** Plasmids contain different protein expression vectors, proteins of interest (POI), and fluorescence proteins (FP) for identification of transfected cells. HEK293T cells transfected with these plasmid-DNAs were used in the FLIM-experiments, pH-measurements, and AL-fusion experiments presented in chapter 3. In case of ClC-7 shRNA and PAC shRNA, two different fluorescence proteins, GFP or iRFP, were used for identification of transfected cells in FLIM-experiments, but the results were identical and therefore merged.

Vector	POI	FP	Clone #	Experiment	Capter
Fsy1.1	LAMP1	mCherry	K.2203	lysosomal localisation	2.4, 3.1, 3.8.1, 3.9
pCMV	Arch3	mKate2	K.2991	FLIM	3.5
P156rrl	ClC-7	GFP	K.3153	FLIM	3.7.1
P156rrl	OSTM-1	mCherry	K.3154	FLIM	3.7.1, 3.7.2
P156rrl	ClC-7	iRFP713	K.3940	pH	3.7.1
pcDNA3.1(+)	OSTM-1	/	K.3906	pH, AL-fusion	3.7.1, 3.7.2, 3.10
P156rrl	ClC-6	GFP	K.2766	FLIM	3.7.1
Fsy1.1	ClC-6	iRFP713	K.3910	pH	3.7.1
Fsy1.1	ClC-3b	YFP	K.2783	FLIM	3.7.1
FsY1.1	ClC-3b	iRFP713	K.3869	pH	3.7.1
Fsy1.1	ClC-7 E245A	mCherry	K.3585	FLIM	3.7.2
Fsy1.1	ClC-7 E245A	iRFP713	K.3870	pH, AL-fusion	3.7.2, 3.10
p156rrl	ClC-7 Y746Q	GFP	K.3684	FLIM	3.7.2
Fsy1.1	ClC-7 Y746Q	iRFP713	K.3911	pH	3.7.2
Fsy1.1	ClC-7 shRNA	GFP	K.3935	FLIM	3.7.3
Fsy1.1	ClC-7 shRNA	iRFP713	K.3946	FLIM, pH, AL-fusion	3.7.3, 3.10
Fsy1.1	PAC shRNA	GFP	K.3971	FLIM	3.8.3
Fsy1.1	PAC shRNA	iRFP713	K.3978	FLIM, pH	3.8.3
pEGFP	Sialin	GFP	K.3471	FLIM	3.8.2
piRFP	Sialin	iRFP713	K.3912	pH	3.8.2
Fsy1.1	Sialin shRNA	iRFP713	K.3945	FLIM, pH	3.8.2
Fsy1.1	SLC26A11	GFP	K.2123	FLIM	3.8.1
Fsy1.1	SLC26A11	iRFP	K.3908	pH	3.8.1
pcDNA3.1(+)	VGLUT1	GFP	K.2751	FLIM	3.9
pcDNA3.1(+)	VGLUT1	iRFP713	K.3871	pH, AL-fusion	3.9, 3.10

2.18 Manufacturers

Addgene, Watertown, MA, USA
Becker & Hickl, Berlin, Germany
Calbiotech, El Cajon, CA, USA
Cayman Chemical Company, Ann Arbor, MI, USA
Gibco, Darmstadt, Germany
Greiner Bio-One, Kremsmünster, Austria
Invitrogen, Carlsbad, CA, USA

Leica, Mannheim, Germany
Merck, Darmstadt, Germany
Newport Spectra Physics, Irvine, CA, USA
Nikon Instruments Europe, Amsterdam, Netherlands
Okolab, Ambridge, PA, USA
Omega Optical, Brattleboro, VT, USA
OriginLab Corporation, MA, USA
PeCon, Erbach, Germany
Polysciences Inc., Worrington, PA, USA
Semrock Inc., Rochester, NY, USA
Sigma-Aldrich, Göttingen, Germany
Thermo Fisher Scientific, Darmstadt, Germany
WTW, Xylem, Rye Brook, NY, USA
Zeiss, Jena, Germany

Chapter 3

Results

3.1 SPQ and MEQ Can Enter the Lysosomal Lumen

SPQ is not membrane permeable and enters the cells via the endocytic pathway. After incubating HEK293T cells in medium supplemented with SPQ for 2 h, a vesicular distribution of SPQ can be observed. Longer incubation times neither increased the amount of loaded vesicles nor the signal intensity.

Similar to the protocol used for loading lysosomes with dextrans, a subsequent chasing step was implemented for SPQ before experiments. The chasing time of 2 h to 16 h, which is usually used to target dextrans to the lysosomes [67], is not suitable for SPQ, because after this time almost no SPQ is left in the vesicles. SPQ seems to pass the endocytic pathway faster than dextran, which might be due to its substantially lower MW of 281.33 Da, compared to the dextrans with 10 kDa. Instead, a shorter chasing time of 20 min was used for SPQ.

To investigate whether the SPQ-positive vesicles are lysosomes, cells were loaded with TMR-dextran (for 7 h followed by 16 h chase) before loading them with SPQ (for 2 h and 20 min chase). Since all of the vesicles which are loaded with SPQ are also loaded with dextran, the SPQ is assumed to be located in the lysosomes (figure 3.1). However, not all the vesicles which are loaded with dextran are also loaded with SPQ. Hence, only a subset of lysosomes can be examined with SPQ.

Unlike SPQ, diH-MEQ is membrane permeable and therefore does not only stain

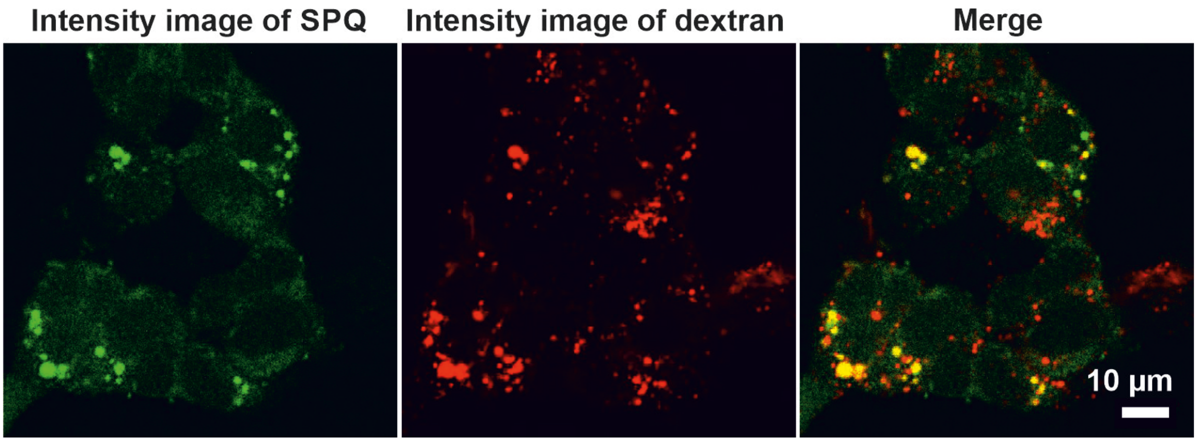

Figure 3.1: **Vesicular SPQ signals colocalize with dextran.** All vesicles which are loaded with SPQ (for 2 h, 20 min chase) are also loaded with the lysosomal marker TMR-dextran (loaded for 7h and chased overnight), but not all the vesicles which are loaded with dextran are also loaded with SPQ (only about 55% ± 11%, N = 14 cells).

compartments of the endocytic pathway but the whole cell. In figure 3.2 (B) the fluorescence lifetime of MEQ is relatively homogeneous throughout the two cells. This could indicate that the $[Cl^-]$ in the cytosol and the lysosomes (and other cell organelles) are equal and therefore indistinguishable. Another possible explanation would be, however, that the signal originating from the small vesicles is overlapped by the signal from the MEQ in the cytosol, especially considering that the vesicles might move during the 80 sec recordings. To be able to distinguish between lysosomes and the cytosol, the lysosomal size was increased by the use of YM-201636.

YM-201636 is a cell-permeable and selective inhibitor of PIKfyve, an enzyme which phosphorylates PI(3)P to PI(3,5)P2. The latter phosphoinositide is present in the membrane of late endosomes and lysosomes and is required for fission. Hence, the use of YM-201636 inhibits the fission of lysosomes and late endosomes, which, in consequence, leads to an increase of their size [68, 69, 71].

In cells treated with YM-201636, the vesicular size is sufficient for the luminal MEQ-signal to be distinguished from the cytosolic signal in the fluorescence lifetime image (figure 3.2 D). These vesicles are assumed to be lysosomes (and partially late endosomes), since YM-201636 selectively increases only the size of lysosomes and late endosomes. Moreover, figure 3.3 shows that after transfecting cells with the lysosomal associated membrane protein 1 (LAMP1) fused to mCherry, the vesicular structures visible in the fluorescence lifetime image of MEQ are LAMP1-positive.

The increase of the lysosomal size has another advantage as it reduces the lysosome‘s

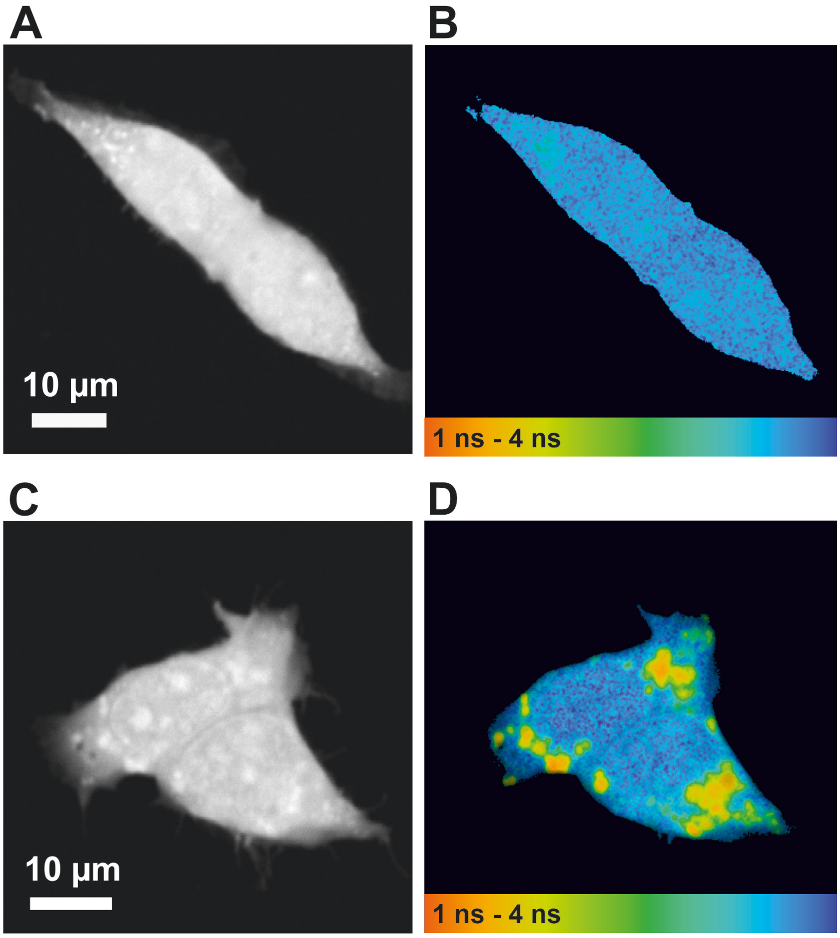

Figure 3.2: **MEQ in cells without vs. cells with YM-201636.** (A) Fluorescence intensity and (B) fluorescence lifetime image of MEQ in HEK293T cells. Lysosomes are not distinguishable from the cytosol because the lysosomal signal is overlapped by the fluorescence originating from the MEQ in the cytosol. (C) Fluorescence intensity and (D) fluorescence lifetime image of YM-201636 treated HEK293T cells loaded with MEQ. Due to the increased lysosomal size, the lysosomes are now distinguishable from the cytosol in the fluorescence lifetime image.

transport velocity. This has also been described by Bandyopadhyay et al., who observed lysosome transport as a function of lysosome diameter and found that, while the active transport is unaffected by the lysosomal size, the diffusive component of the transport decreases proportionally to the increasing diameter [14]. The reduction of the lysosome‘s velocity additionally improves the recording conditions, because the MEQ signal originating from lysosomes that move a lot during the recordings will still be overlapped by the cytosolic signal, even if the size of the lysosome is increased. This might also be the reason why some of the smaller vesicles which can be seen in the fluorescence intensity image of LAMP1 in figure 3.3 are not visible in the fluorescence lifetime image of MEQ. The intensity image of LAMP1 was taken during the recording of the first

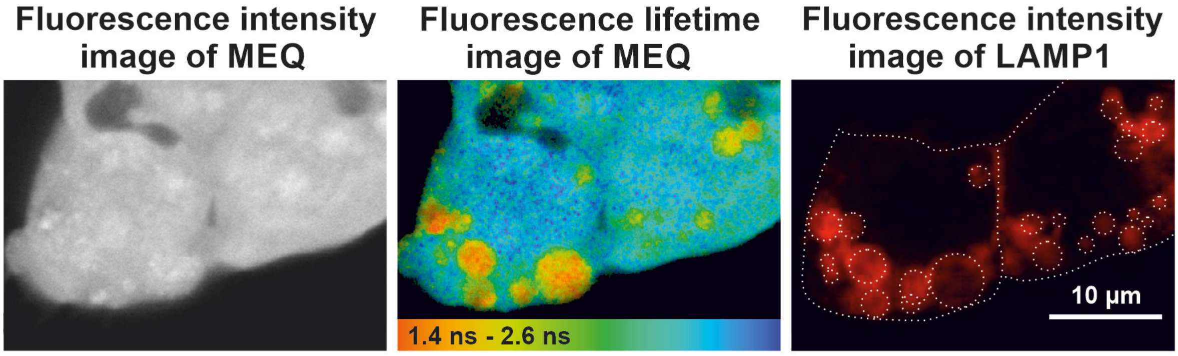

Figure 3.3: **MEQ is localized in LAMP1-positive vesicles.** Images of HEK293T cells transfected with LAMP1-mCherry, treated with YM-201636 and loaded with diH-MEQ. The vesicular structures visible in the fluorescence lifetime image of MEQ are LAMP1-positive.

frame of the fluorescence lifetime image, but during the recording of the following frames some lysosomes possibly moved out of the focus plane and therefore are blurry or even invisible in the resulting fluorescence lifetime image.

To summarize, chloride concentrations in enlarged lysosomes as well as in lysosomes with normal size can be measured well with SPQ, whereas MEQ offers the possibility to simultaneously measure chloride concentrations in the cytosol and in enlarged lysosomes.

However, it has to be taken into account that YM-201636 does not only increase the size of lysosomes but also that of late endosomes, and that vesicles that contain SPQ or MEQ might not exclusively be lysosomes but partially also late endosomes. Hence, the vesicles measured in this thesis are most likely a mixture of late endosomes, lysosomes, and endolysosomes. This is, however, a general issue, since it has been shown that even LAMP1 is not exclusively located in the lysosomes [85]. It also should not be forgotten that for both SPQ and MEQ only the fraction of the larger vesicles is analyzed, while for pH considerably smaller vesicles were accepted (chapter 2.9). Nonetheless, for simplification, in the following chapters this mixture of vesicles will be referred to as lysosomes.

3.2 Determination of Cytosolic and Lysosomal [Cl$^-$] in HEK293T Cells

Representative fluorescence intensity and lifetime images of cells loaded with SPQ and diH-MEQ are shown in figure 3.4.

In case of SPQ, most of the dye accumulates in the lysosomes. The fluorescence

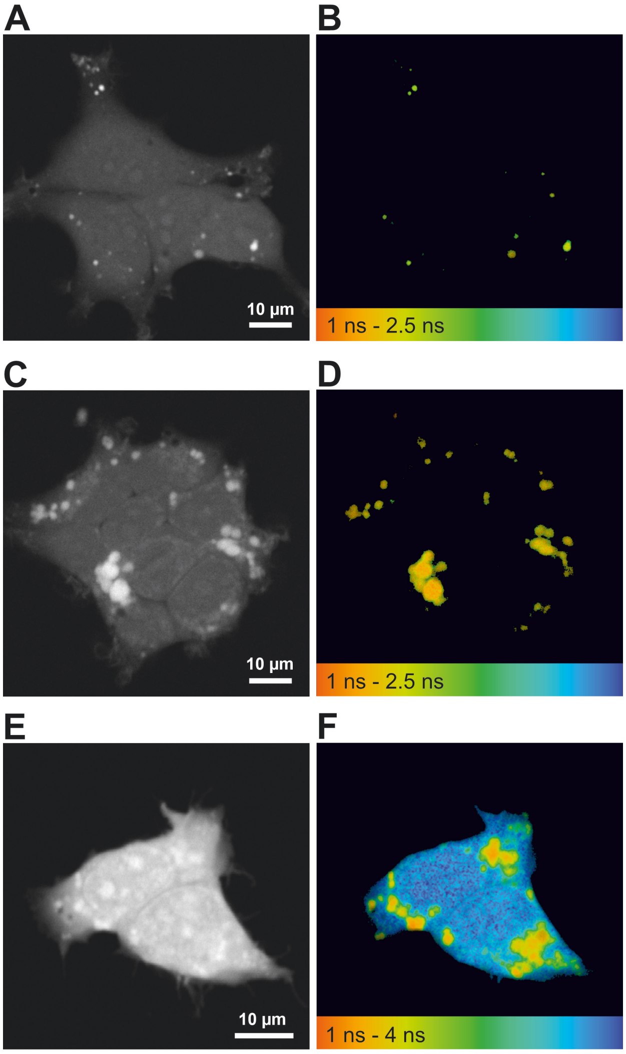

Figure 3.4: **Representative images of HEK293T cells loaded with SPQ or diH-MEQ** (A) Fluorescence intensity image and (B) corresponding fluorescence lifetime image of HEK293T cells loaded with SPQ. (B shows τ_{mean} from 1 ns to 2.5 ns, represented by a color code). (C) Fluorescence intensity image and (D) corresponding fluorescence lifetime image of HEK293T cells loaded with SPQ. Cells were treated with YM-201636 overnight, which leads to an increase of the lysosomal size. (E) Fluorescence intensity image of MEQ in HEK293T cells after loading with diH-MEQ. Lysosomes are hardly distinguishable from the cytosol. (F) Corresponding fluorescence lifetime image showing τ_{mean} from 1 ns to 4 ns, represented by a color code. Here, the lysosomes can be easily identified because of the shorter fluorescence lifetimes compared to the cytosol.

intensity of SPQ in the cytosol is too low to overcome the set intensity threshold in SPCImage (Version 6.0, Becker & Hickl). Hence, in the corresponding fluorescence lifetime image, only the τ_{mean} for the lysosomes with high fluorescence intensity was evaluated, represented by a color code (figures 3.4 B (lysosomes of normal size) and D (lysosomes enlarged with YM-201636)).

In the intensity image of MEQ, lysosomal structures can hardly be identified, because the cytosolic and lysosomal signal intensities are almost equal (figure 3.4 E). The corresponding fluorescence lifetime image reveals the position of the lysosomes, as the fluorescence from the lysosomes has significantly shorter lifetimes than the cytosolic MEQ signal (figure 3.4 F).

The chloride dependence of the fluorescence lifetime τ_{mean} of SPQ and MEQ in HEK293T cells was determined using the calibration method described in chapter 2.6.1. During calibration, the fluorescence lifetimes τ_{mean} of MEQ in the cytosol and lysosomes equalize, as shown in figure 3.5 A, which indicates a successful permeabilization of the membranes. To ensure complete equilibration of lysosomal and cytosolic [Cl^-] to the externally set [Cl^-] between 10 mM and 140 mM (in 10 mM steps), cells were incubated in the calibration solution for approx. 1 h. Since after this time the cytosolic and lysosomal τ_{mean} are equal (see figure 3.5 B), the average τ_{mean} of the whole cytosol could be used for evaluation, and the resulting calibration function was used for both the cytosol and the lysosomes. For each externally set [Cl^-], corresponding fluorescence lifetimes were measured at three days at least, resulting in a total number of at least 3 coverslips (N) and about 400 measured cells per [Cl^-]. During calibration, the measured τ_{mean} change from 5.5 ns to 1.9 ns at preset [Cl^-] between 10 mM and 140 mM (figure 3.5 E).

For SPQ, the same method was employed, but the resulting fluorescence lifetimes τ_{mean} were evaluated from single lysosomes. This was separately done with untreated HEK293T cells and with cells treated with YM-201636. For each externally set [Cl^-] between 30 mM and 140 mM (in 10 mM steps), corresponding fluorescence lifetimes were measured at at least three days as well, resulting in a total number of at least 3 coverslips (N), 40 cells, and about 100 to 600 lysosomes per [Cl^-].

To calculate the Stern-Volmer constants for SPQ and MEQ, the respective inverse fluorescence lifetimes were plotted over the corresponding chloride concentrations. The inverse intercepts of the resulting linear regression curves equal τ_0, from which, together with the slope, the corresponding Stern-Volmer constants K_{SV} were calculated (equation 2.5, Figure 3.5 D and E). The calibration functions for SPQ with and without YM-201636 and MEQ were used in all experiments to calculate [Cl^-] from the measured fluorescence lifetimes τ_{mean}. All of the three calibration curves can be fit well with a linear equation and have high coefficients of determination R^2 of 0.98 (SPQ without YM-201636) and 0.99 (SPQ with YM-201636 and MEQ). This value indicates how well the data and the regression model coincide and can range from 0 to 1, with 1 indicating a perfect fit.

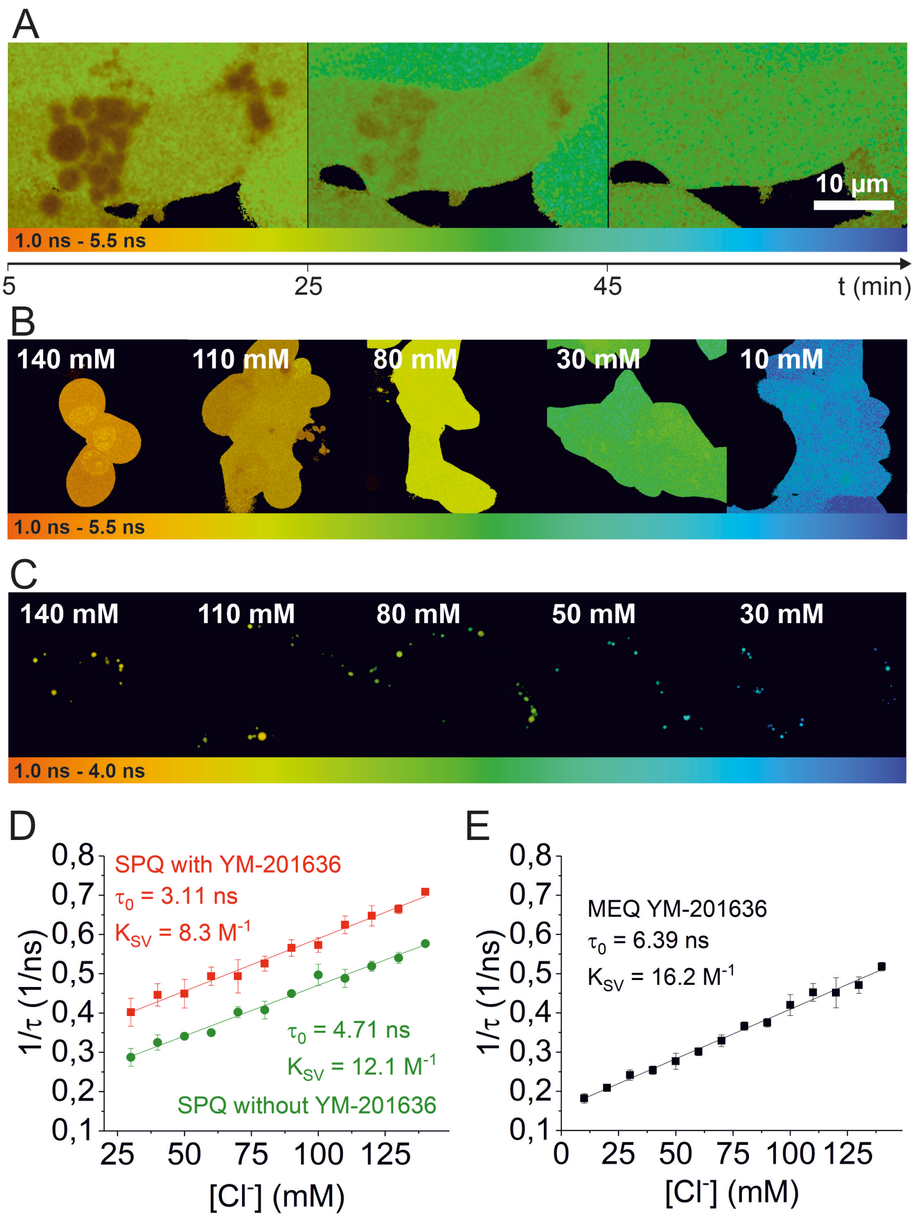

Figure 3.5: **Calibration of SPQ and MEQ in HEK293T cells.** (A) Fluorescence lifetime images of MEQ after 5, 25, and 45 min of incubation in calibration solution ([Cl⁻] = 50 mM). The fluorescence lifetimes measured in the cytosol and lysosomes equalize after 45 min. (B) Fluorescence lifetime images of HEK293T cells during calibration of MEQ. The different chloride concentrations between 10 mM and 140 mM result in different fluorescence lifetimes of the MEQ, represented by a color code. The fluorescence lifetime in cytosol and lysosomes are equal during calibration. (C) Fluorescence lifetime images of HEK293T cells during calibration of SPQ. Only the lysosomes are loaded with SPQ. (D) Calibration plot for SPQ with (red) and without (green) YM-201636. (E) Calibration plot of MEQ with YM-201636. (Error bars show standard deviation SD of N = 3 - 5 coverslips.)

The difference in the calibration curves of SPQ with and without YM-201636 is unexpected. If one had to predict a difference, shorter fluorescence lifetimes of SPQ would be anticipated due to higher SPQ concentration in smaller vesicles (in the absence YM-201636). The higher SPQ concentration could lead to self-quenching of SPQ fluorescence accompanied by fluorescence decay shortening. On the contrary, the fluorescence lifetimes of SPQ in the vesicles without YM-201636 treatment are longer than in the YM-201636 enlarged vesicles. Also, no systematic difference was observed in the SPQ fluorescence intensities of smaller and larger vesicles – neither within cells treated with YM-201636 nor when comparing cells treated and non-treated with YM-201636. As mentioned before, the vesicles measured in this thesis are part of the endolysosomal system, most likely a mixture of late endosomes and lysosomes in unperturbed cells. Perhaps, the treatment of cells with YM-201636 partially disturbs the mechanisms by which SPQ enters into and distributes within the endolysosomal system, so that the SPQ-filled vesicles in cells treated with YM-201636 have higher relative amount of late endosomes. However, it is unlikely that this would lead to such pronounced differences in the fluorescence lifetimes, even if the composition of quenchers in endosomes and lysosomes was slightly different. So the reason for the difference in the calibration curve of SPQ with and without YM-201636 is unclear.

3.3 Determination of Lysosomal pH in HEK293T Cells

To measure the lysosomal pH, the ratio of the fluorescence intensities of OG- and TMR-dextran (I_{OG}/I_{TMR}) was calibrated according to the high [K$^+$]-method [78] (see chapter 2.8.1). For each day of experiments, an individual calibration was performed. This was necessary, since the ratios resulting from the same preset pH but measured on different days were sometimes shifted towards lower or higher values, possibly due to daily fluctuations in the laser powers of the two different lasers or variations in the exact amount of dextrans used for loading the cells. For each preset pH between 3.5 and 7.3, the OG/TMR-ratios of lysosomes of at least 25 cells were measured.

Figure 3.6 exemplary shows a calibration curve of a single measurement day, where the measured I_{OG}/I_{TMR}-ratios are plotted against the respective preset pH and sigmoidally fitted with a DoseResponse model, which was then used to calculate the pH from I_{OG}/I_{TMR} (see chapter 2.8.2, equation 2.7).

The average calibration parameters from all calibrations are listed in table 3.1. The average pKa (acid dissociation constant and inflection point of the calibration curve,

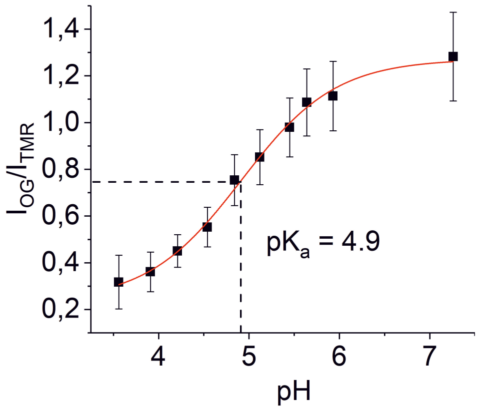

Figure 3.6: **Calibration of I_{OG}/I_{TMR} ratio in HEK293T cells.** Exemplary calibration curve of a single measurement day. The pH dependence of I_{OG}/I_{TMR} was calibrated at different pH values ranging from 3.5 to 7.3 and was fitted to a DoseResponse model (red line). An individual pH calibration was performed for each day of experiments with only one coverslip per preset pH. Therefore, the error bars do not refer to N = number of coverslips but to N = number of lysosomes ($>$ 500).

where I_{OG}/I_{TMR} is 50% of maximum) is 4.81 ± 0.11 and thus in the optimal range for the expected lysosomal pH between 4.3-5.5 [19].

Table 3.1: **Average values for the calibration parameters pK_a, $A1$, $A2$ and b (equation 2.7) and $\Delta(I_{OG}/I_{TMR})$ resulting from all calibrations (N = 33).**

pK_a	4.81 ± 0.11
$A1$	0.16 ± 0.08
$A2$	1.18 ± 0.14
b	0.82 ± 0.13
$\Delta(I_{OG}/I_{TMR})$	1.01 ± 0.12

3.4 Lysosomal [Cl⁻] and pH in HEK293T Cells Under Physiological Conditions

Under physiological conditions, an average cytosolic chloride concentration $[\mathrm{Cl}^-]_{cyto}$ of 56.4 ± 9.4 mM (SD) was measured with MEQ in HEK293T cells (figure 3.7 A). Although this is quite high, it is within the quite widespread range of $[\mathrm{Cl}^-]_{cyto}$ other groups have measured in different cell types with different methods [86, 87, 88, 89].

In lysosomes enlarged with YM-201636, an average chloride concentration $[\mathrm{Cl}^-]_{lyso}$ of 147 ± 16 mM (SD) was measured using MEQ. This is significantly higher than the measured cytosolic $[\mathrm{Cl}^-]$ (figure 3.7 A).

With SPQ, a similar chloride concentration $[Cl^-]_{lyso}$ of 150 ± 25 mM (SD) was measured in lysosomes with normal size (figure 3.7 A). When using YM-201636, however, a significantly lower chloride concentration $[Cl^-]_{lyso}$ of 122 ± 29 mM (SD) was determined with SPQ. The use of YM-201636 might have unknown effects, which influence $[Cl^-]$. Like mentioned before, the vesicles measured in this thesis are most likely a mixture of late endosomes and lysosomes in unperturbed cells. The treatment of cells with YM-201636 might partially disturb the mechanisms by which SPQ enters into and distributes within the endolysosomal system, so that the SPQ-filled vesicles in cells treated with YM-201636 have a higher relative amount of late endosomes, which might possess lower $[Cl^-]$. However, apart from the results presented in this chapter, the other SPQ-experiments from this study have been performed without the use of YM-201636 and the measurements with MEQ are not expected to be affected by YM-201636 in the same way, because unlike SPQ, diH-MEQ is membrane permeable and therefore able to enter the lysosomes via diffusion.

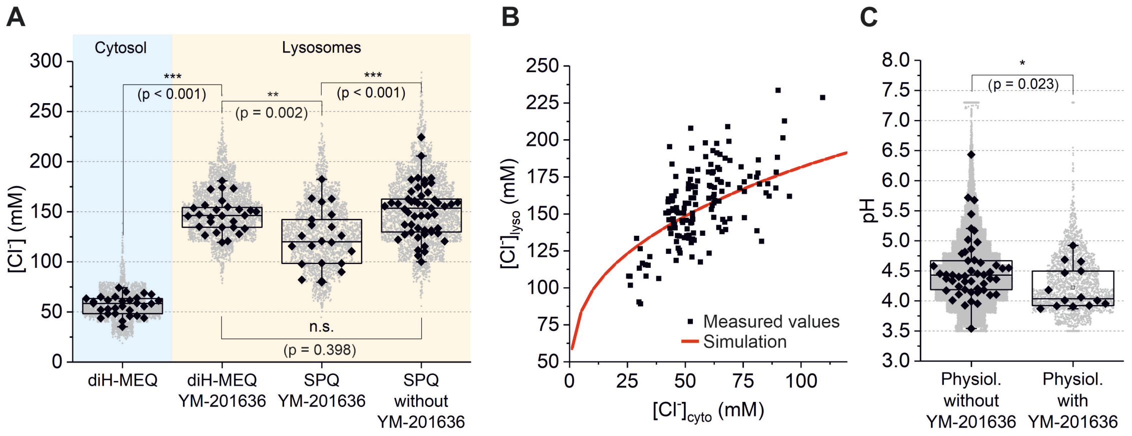

Figure 3.7: **Results under physiological conditions.** (A) Measured cytosolic (blue background) and lysosomal (orange background) $[Cl^-]$ under physiological conditions measured with MEQ and SPQ (either with or without enlargement of lysosomes by YM-201636). The small dots in light grey refer to single lysosomes, the bigger black dots represent single dishes as experimental units, which are used for statistics. (B) Lysosomal $[Cl^-]$ plotted over cytosolic $[Cl^-]$. Here, each black point represents the cytosolic and average lysosomal $[Cl^-]$ of a single cell measured with MEQ. The red line is the result of a simulation using the model by Ishida et al. [4] (C) Lysosomal pH measured with OG- and TMR-dextran in normal and enlarged lysosomes. Note the accumulation of the small grey dots (represent single lysosomes) at pH 7.3. Some measured I_{OG}/I_{TMR}-ratios were higher than the average ratio measured at the upper plateau of the sigmoidal pH calibration curve (at pH 7.3, figure 3.6). These values were assigned to pH 7.3, leading to an accumulation of dots at this pH in the graph.

In figure 3.7 (B), average lysosomal $[Cl^-]$ of single cells are plotted vs. the respective cytosolic [Cl^-]. There is a clear correlation: a higher $[\mathrm{Cl}^-]_{cyto}$ is accompanied by higher $[\mathrm{Cl}^-]_{lyso}$, which could also be shown by simulations using the model by Ishida et al. [4] (red line).

Figure 3.7 (C) shows the average pH of lysosomes in HEK293T cells. Normal-sized lysosomes have an average pH of 4.52 ± 0.52 (SD), consistent with lysosomal pH values determined before by other groups [19, 90, 91]. Lysosomes treated with YM-201636 have a slightly lower pH of 4.22 ± 0.35 (SD). Lenk et al. also report on hyperacidification of enlarged lysosomes and speculate that there might be proton-permeable channels or transporters in the lysosomal membrane, which have a PI(3,5)P2-dependence, that could account for the decreased pH in cells where this phosphoinositide is depleted [92].

3.5 V-ATPase is the Driving Force for Lysosomal Chloride Accumulation

In 2003, Sonawane et al. observed low [Cl^-] of ∼25 mM in early endosomes shortly after formation, despite the high extracellular [Cl^-] of ∼140 mM. This is explained by an interior-negative Donnan potential at the inner surface of the endosomal membrane, which leads to an extrusion of anions like chloride [93]. Furthermore, Saha et al. have shown that [Cl^-] in endocytic vesicles of haemocytes of *Drosophila* larvae increase from 37 mM to 109 mM during endolysosomal maturation [28].

These results show that the high lysosomal [Cl^-] shown in the previous chapter cannot simply be explained by high extracellular [Cl^-] taken up during endocytosis. Since the vesicular [Cl^-] increases during endolysosomal maturation, there has to be a driving force for the influx of Cl^- ions into the lumen. This driving force might be permitted by the v-ATPase, since it actively pumps protons into the lumen and builds up a lumen positive potential, which may initiate an inward flux of anions, such as chloride, to counter-balance the positive charges. Inhibition of the v-ATPase would then not only increase the luminal pH but would also lead to a decrease of luminal [Cl^-].

To block the v-ATPase, cells were incubated in cell medium supplemented with 200 nM bafilomycin A1 (Baf A1) for 6 h prior to measurements (and ongoing during the experiments). As a first result, figure 3.8 (A) shows that the lysosomal pH significantly increases as it was expected, since the v-ATPases do not pump protons into the lysosome anymore. However, with 6.29 ± 0.75 (SD), the resulting pH is still slightly acidic. This might be explained by another mechanism that possibly drives protons into the lumen, which is discussed in chapter 3.7.3.

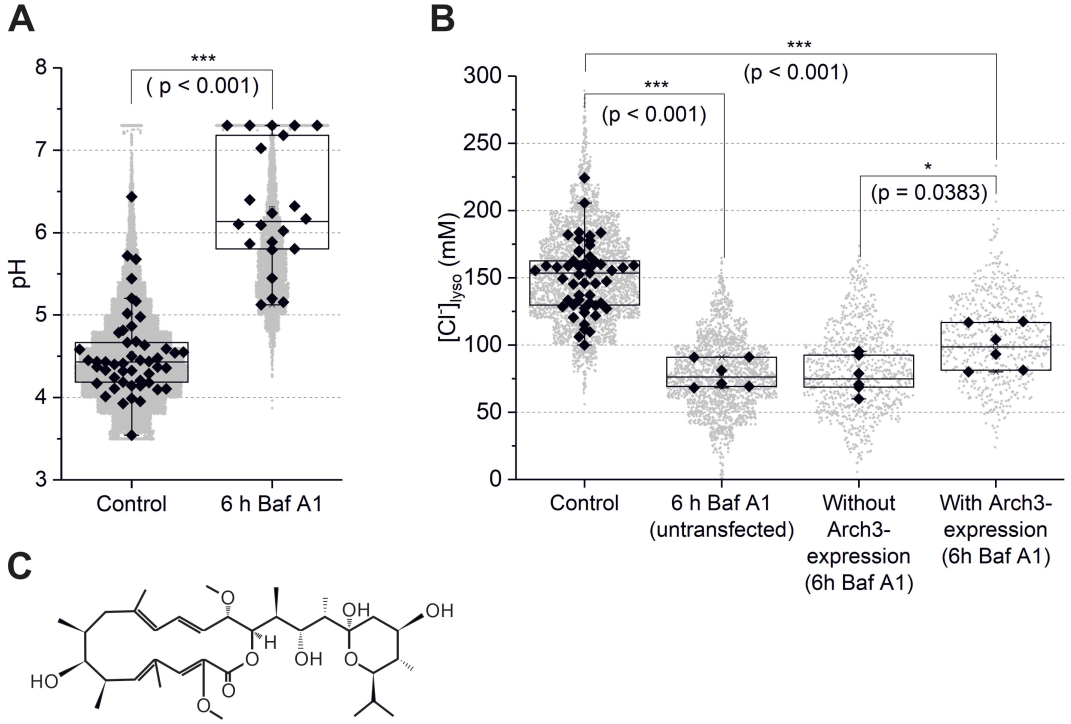

Figure 3.8: **Influence of proton concentration on [Cl⁻].** (A) Lysosomal pH measured with OG- and TMR-dextran in normal-sized lysosomes of HEK293T cells (without YM-201636) under normal conditions as well as after 6h incubation of cells in medium supplemented with 200 nM bafilomycin A1. The accumulation of values at pH 7.3 is more pronounced with Baf A1. Due to the higher pH, the I_{OG}/I_{TMR}-ratios in more lysosomes are higher than the average ratio measured at the upper plateau of the sigmoidal pH calibration curve. Thus, more measured values had to be assigned to pH 7.3. (B) Lysosomal [Cl⁻] measured with SPQ in normal-sized lysosomes of HEK293T cells (without YM-201636). The control was measured under normal conditions. The other three boxplots were measured after 6h incubation in medium with 200 nM bafilomycin A1 (6h Baf A1) either with untransfected cells, or in dishes which have been transfected with Arch3. In these dishes, $[\mathrm{Cl}^-]_{lyso}$ was measured in cells without Arch3-expression as well as in cells with Arch3-expression, after 2-10 min of activation of Arch3 with light (wavelength 561 nm). (C) Chemical structure of bafilomycin A1.

As predicted, figure 3.8 (B) shows that the treatment of cells with Baf A1 indeed leads to a significant decrease of lysosomal [Cl⁻] to 79 ± 11 mM (SD). Simulations using the model by Ishida et al. could reproduce this result (figure 3.14 A, red squares vs. blue circles). A reduction of [Cl⁻] through Baf A1 treatment was also observed by Hara-Chikuma et al. in the endosomes of hepatocytes from mice, where they used the Cl⁻-sensitive dye BAC conjugated to dextran together with the Cl⁻-insensitive dye TMR to measure endosomal [Cl⁻] ratiometrically [94].

In 2015, Rost et al. were able to reacidify lysosomes of HEK293 cells, which had been treated with Baf A1, optogenetically by the use of the light-driven proton pump

Archaerhodopsin-3 (Arch3) [95]. To test whether this could also rescue the lysosomal $[Cl^-]$ after Baf A1 treatment, cells were transfected with Arch3 coupled to CD63 for lysosomal targeting. To activate Arch3, cells were illuminated with 561 nm light for 2 to 10 min. The 561 nm pumping light was switched off during the 80 s for acquisition of the FLIM-images. Figure 3.8 (B) shows that lysosomal $[Cl^-]$ in those cells which showed Arch3-expression indeed increased significantly (*) to 99 ± 17 mM (SD) compared to $[Cl^-]_{lyso}$ of cells without Arch3 expression in the same dishes, where $[Cl^-]_{lyso}$ were still as low as 78 ± 14 mM (SD). However, the high $[Cl^-]$ of around 150 mM measured without Baf A1 could not be fully rescued with Arch3. This can have several reasons: First of all, the number of v-ATPases in the lysosomal membrane might be much higher than the number of Arch3 in the lysosomal membrane of transfected cells. Secondly, the transport rate of the v-ATPase might be higher than that of Arch3. Also, Rost et al. observed that the lysosomal acidification in their experiment required constant pumping, indicating a strong proton leak in lysosomes [95]. Hence, during the 80 s of FLIM recordings at 750 nm, which is a suboptimal excitation wavelength of the photocycle of Arch3, there might be a leak of protons, which would consequently reduce the measured $[Cl^-]_{lyso}$.

3.6 Blocking of Lysosomal K^+-Channel Increases Lysosomal $[Cl^-]$

Studies showing that the lysosomal pH is unaffected in neurons of ClC-7 knockout mice have raised questions regarding the role of chloride as a counterion for lysosomal acidification [33]. Instead of an influx of anions, an outflux of cations like sodium or potassium might as well dissipate the lumen positive potential built up by the v-ATPase. Some studies have suggested that especially potassium rather than sodium plays an important role in facilitating lysosomal acidification [91, 96, 97]. Cang et al. report that the potassium conductance in the lysosome is mainly mediated by the K^+-channel TMEM175 and that this channel can be blocked by 4-aminopyridine (figure 3.9 C) [98].

To test whether the inhibition of TMEM175 has an impact on the lysosomal pH or $[Cl^-]$, HEK293T cells were incubated in medium supplemented with 400 µM 4-aminopyridine (4-AP, Sigma) for 30 min. Figure 3.9 (B) shows that the lysosomal pH significantly (***) increases to 4.84 ± 0.32 (SD) upon 4-AP treatment. So, the lysosomal acidification is indeed impaired when the K^+-channel TMEM175 is blocked, but it is still acidic. The blocked K^+-efflux might increase the membrane potential of the lysosome to more lumen positive values, which could lead to an influx of Cl^-. Indeed, figure 3.9 (A) shows a significant increase of lysosomal [Cl$^-$] to 198 ± 23 mM (SD) in cells treated with 4-AP. This could explain why the measured lysosomal pH in those cells is still very acidic. The role of Cl$^-$ as a counterion might get more important upon blocking the K$^+$ efflux.

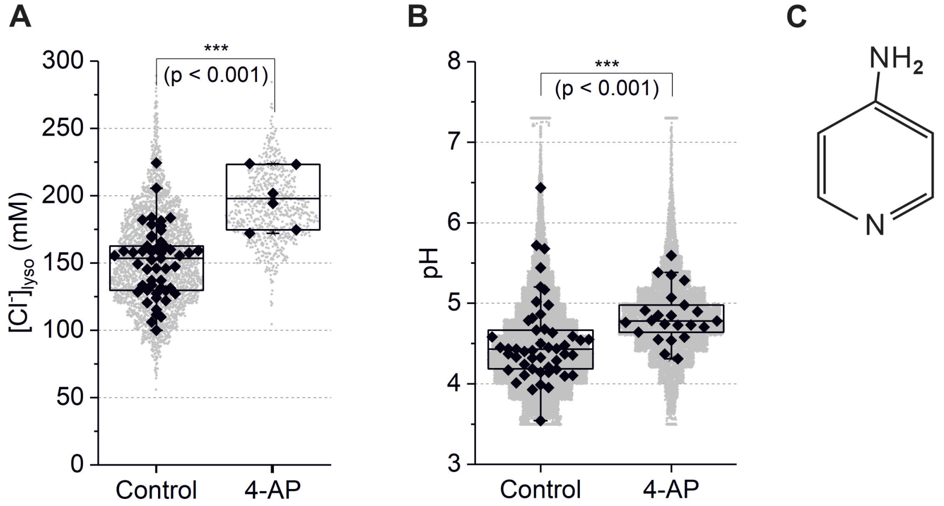

Figure 3.9: **Effect of 4-aminopyridine (4-AP) on lysosomal [Cl$^-$] and pH.** (A) Lysosomal [Cl$^-$] measured with SPQ in normal-sized lysosomes (without YM-201636) of HEK293T cells under normal conditions (control) and after 30 min incubation of cells in medium supplemented with 400 µM 4-AP. (B) Corresponding lysosomal pH. (C) Chemical structure of 4-AP.

Another interesting observation was made upon treatment of cells with 4-AP, as the lysosomal size in these cells was slightly increased, albeit not as much as upon treatment with YM-201636.

Because 4-AP has a benzene ring (figure 3.9 C) and therefore absorbs in the near-ultraviolett spectral region, it was tested whether the measured effect of 4-AP treatment is indeed biological or could also be an optical effect due to fluorescence of 4-AP itself. HEK293T cells, which were not loaded with any dye, were treated with 4-AP, and the fluorescence intensity and lifetimes were measured under the same conditions as in all other experiments (same filter, same excitation). The resulting fluorescence lifetime and intensity was indistinguishable from the cell's autofluorescence and negligibly low compared to SPQ fluorescence intensity.

Simulations with the mathematical model by Ishida et al. [4] could reproduce the increase of lysosomal [Cl$^-$] as well as a slight increase of the pH at lower potassium permeabilities P_K (figure 3.10). They furthermore predict a much higher [K$^+$], a lower [Na$^+$], and a more positive membrane potential U, when P_K is very low.

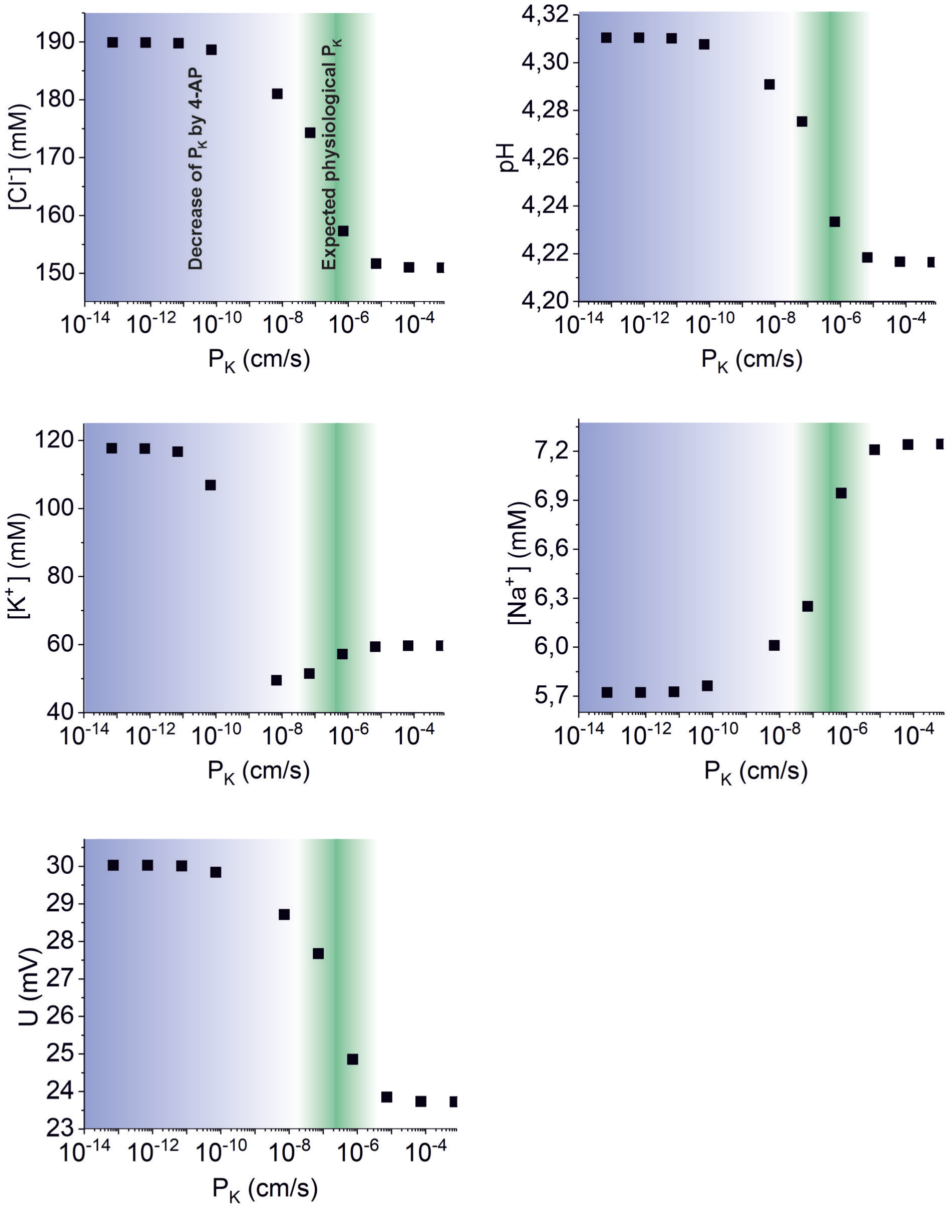

Figure 3.10: **Simulations of the impact of the potassium permeability P_K.** Simulated lysosomal $[Cl^-]$, pH, $[K^+]$, $[Na^+]$, and membrane potential U plotted versus the potassium permeability P_K to examine the influence of 4-AP. Simulations were performed with the Berkeley Madonna model for lysosomal pH regulation, provided by Ishida et al. [4]. Parameters used for simulations are listed in table 3.2, with N CLCs = 10000 and N v-ATPase = 15000, but with 150 mM as initial $[Cl^-]$ and 60 mM as initial $[K^+]$. These are the respective final concentrations according to the simulation with a P_K of $6.7 * 10^{-7}$ cm/s (which is assumed to be close to the physiological value without 4-AP), and were chosen for this simulation, because cells are treated with 4-AP only 30 min before measurements, so the majority of lysosomes is expected to already have reached these concentrations. The green background represents the values of P_K assumed to be close to the physiological value without 4-AP, the use of 4-AP is expected to decrease P_K (blue background).

3.7 Role of CLCs in Lysosomal Chloride Accumulation

The results from the previous chapters indicate that lysosomes accumulate Cl^- in a secondary active process driven by the v-type ATPases. Chloride accumulation apparently is electrogenic and directly modified by changes in the membrane potential. But the question is yet to be answered, by which pathway chloride ions enter the lysosome.

Lysosomes express various CLC chloride-proton exchangers, such as certain splice variants of ClC-3 [99], heterodimers of ClC-4 with these lysosomal ClC-3 splice variants [35], ClC-6 [36], and ClC-7 [37, 38, 100], which was postulated to represent the primary chloride permeation pathway in lysosomes. All the transporters exchange Cl^- and protons at a 2:1 stoichiometry [34] and thus transport three charges per transport cycle. The electrogenicity of the transport makes the lysosomal membrane potential a key determinant of the transport direction, i.e. whether the CLCs mediate chloride-driven acidification or proton-driven Cl^- accumulation.

In the following subchapters, the influence of ClC-7 as well as ClC-3b and ClC-6 on the lysosomal $[Cl^-]$ and pH are examined. ClC-7 and the two ClC-7 mutants E245A and Y756Q were always cotransfected with its β-subunit Ostm1 (osteopetrosis-associated transmembrane protein 1), which is required for the transport activity as well as the stability of ClC-7, probably by protecting it from degradation [41, 44, 45].

3.7.1 Overexpression of CLCs Does Not Change $[Cl^-]_{lyso}$

To investigate the influence of the members of the CLC family which are endogenously present in the lysosomal membrane, ClC-7, ClC-6, and ClC-3b were overexpressed in HEK293T cells. ClC-6 is usually almost exclusively expressed in neurons of the central and peripheral nervous system [36]. Nonetheless, for the sake of completeness, it was included in this measurement program.

Figure 3.11 (A) shows that neither the overexpression of ClC-7 nor the expression of ClC-6 changes the $[Cl^-]_{lyso}$ significantly.

Interestingly, the overexpression of ClC-3b leads to an increase of the size of endo-lysosomal vesicles, even without the use of YM-201636 (figure 3.11 C) [99]. Also, lysosomes overexpressing ClC-3b could not be loaded with SPQ. Therefore, here the $[Cl^-]$ were measured using MEQ instead of SPQ, and as a control, the results were compared to the $[Cl^-]$ of lysosomes enlarged with YM-201636 and measured with MEQ as well. Again,

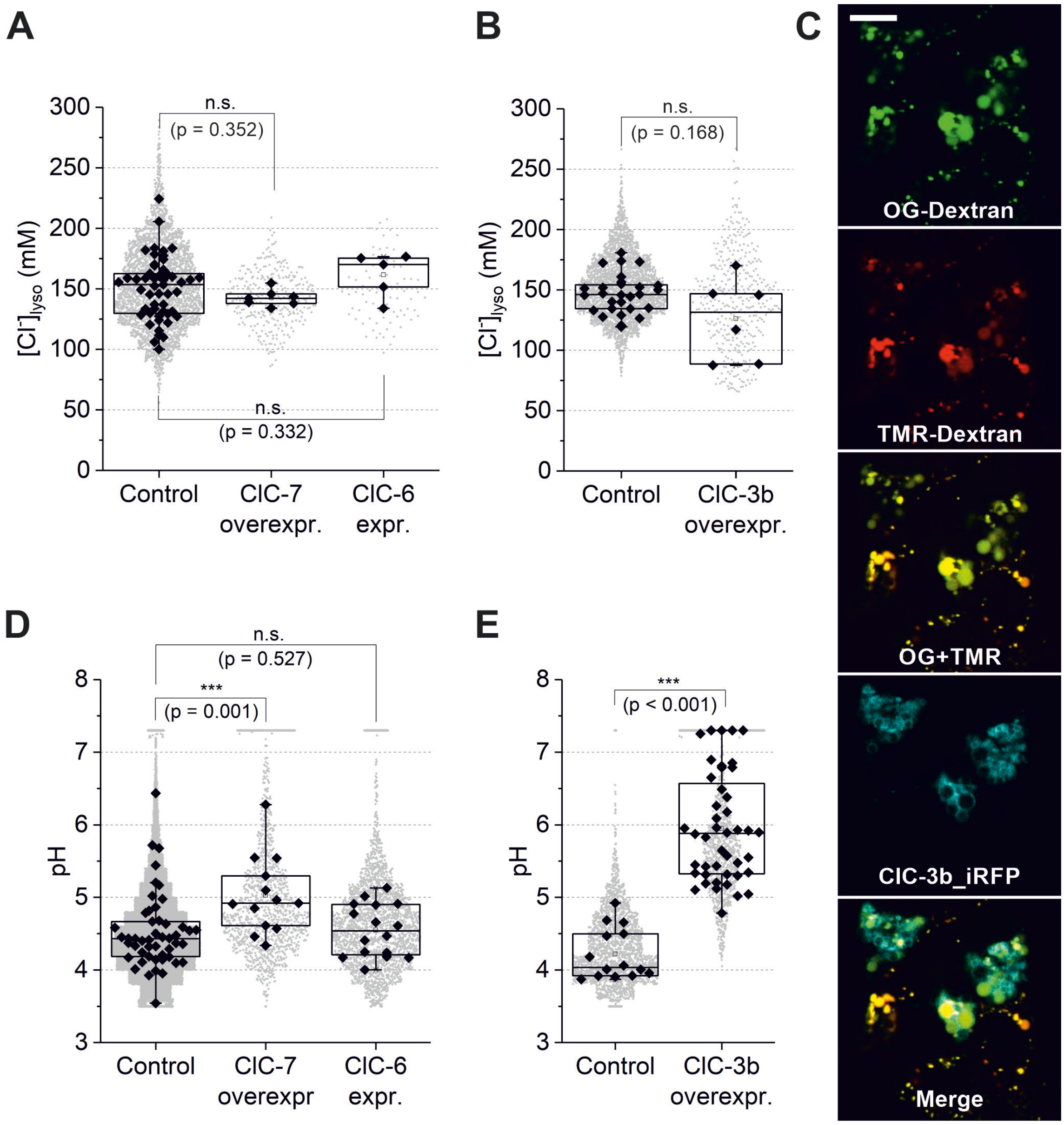

Figure 3.11: **Overexpression of CLCs.** (A) $[Cl^-]_{lyso}$ measured with SPQ in lysosomes of normal size in untransfected HEK293T cells (control) and cells overexpressing ClC-7 or expressing ClC-6. (B) $[Cl^-]_{lyso}$ measured with MEQ in enlarged lysosomes (with YM-201636) of untransfected HEK293T cells (control) and cells overexpressing ClC-3b. (C) Confocal images of HEK293T cells transfected with ClC-3b (iRFP) and loaded with OG- and TMR-dextran. The vesicles in the cells with ClC-3b-expression are enlarged, even though no YM-201636 was used. Scale bar: 10 µm. (D) Lysosomal pH in normal-sized lysosomes of untransfected HEK293T cells (control) and cells overexpressing ClC-7 or expressing ClC-6. (E) Lysosomal pH in enlarged lysosomes (with YM-201636) of untransfected HEK293T cells (control) and cells overexpressing ClC-3b.

the $[\mathrm{Cl}^-]_{lyso}$ is not significantly altered in these vesicles compared to untransfected cells (figure 3.11 B).

In contrast to these results, with the exception of ClC-6, the pH changes upon overexpression of CLCs. The overexpression of ClC-7 and ClC-3b significantly increases the luminal pH to 5.03 ± 0.53 (SD) and 5.95 ± 0.74 (SD), respectively (figures 3.11 D and E).

3.7.2 Effect of E245A and Y756Q Mutation of ClC-7 on Lysosomal $[\mathrm{Cl}^-]$ and pH

Mutations of channels and transporters can provide valuable information on the function of the respective WT protein, so in this chapter, two mutations of ClC-7 are examined.

The mutation E245A converts ClC-7 into an uncoupled Cl^- conductor and causes osteopetrosis [38]. Figure 3.12 (A) shows that this mutation leads to a significant (*) decrease of $[\mathrm{Cl}^-]_{lyso}$ to 123 ± 6 mM (SD). Weinert et al. measured the same effect in fibroblasts of mice [38], but they did not measure a change in the lysosomal pH. In contrast, here a significant (***) increase of the lysosomal pH to 5.25 ± 0.64 (SD) is determined (figure 3.12 B).

Y746Q is a disease-associated mutation of ClC-7, which modifies the time course of ClC-7 currents upon depolarizing voltage steps, i.e. it accelerates its usually slow activation by membrane depolarization. The mutation causes osteopetrosis as well as gingival hamartomas in cattle [47], but a change in $[\mathrm{Cl}^-]_{lyso}$ does not seem to cause this phenotype, since no significant influence on the lysosomal $[\mathrm{Cl}^-]$ was observed (figure 3.12 A). Also, the lysosomal pH is only slightly increased to 4.84 ± 0.64 (SD) in this mutation (figure 3.12 B).

An interesting observation was made with the E245A mutation, as lysosomes with this mutation, for some inexplicable reason, could not be enlarged by YM-201636 (figure 3.12 C). This was not the case for the Y746Q mutation (figure 3.12 D).

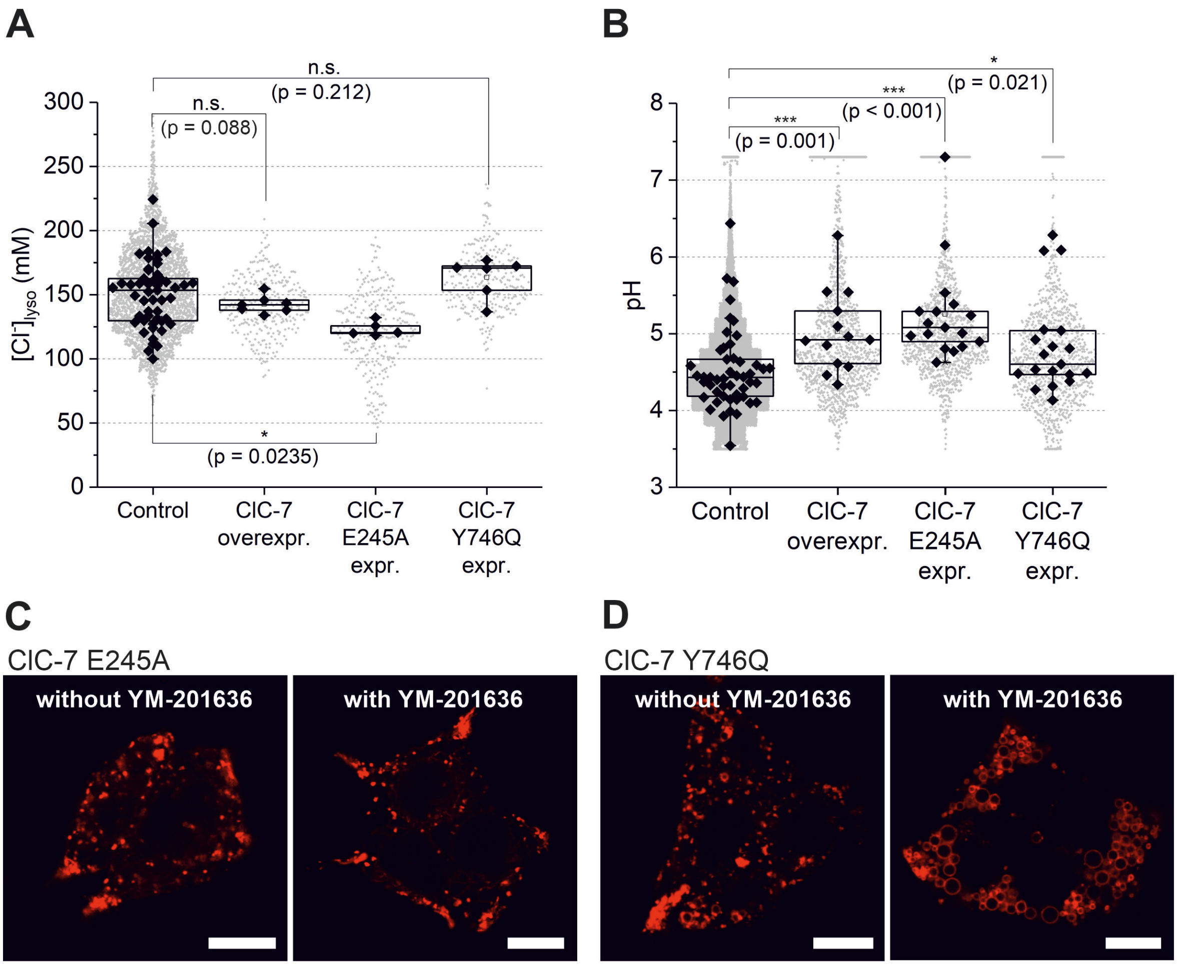

Figure 3.12: **Effect of mutations of ClC-7 on lysosomal $[Cl^-]$ and pH.** (A) Lysosomal $[Cl^-]$ measured with SPQ in normal-sized lysosomes of untransfected HEK293T cells (control) and cells overexpressing ClC-7 or expressing ClC-7 E245A or ClC-7 Y746Q. (B) Lysosomal pH of normal-sized lysosomes of untransfected HEK293T cells (control) and cells overexpressing ClC-7 or expressing ClC-7 E245A or ClC-7 Y746Q. (C) Confocal images of HEK293T cells transfected with ClC-7 E245A without and with YM-201636 treatment. Scale bars: 10 µm. (D) Confocal images of HEK293T cells transfected with ClC-7 Y746Q without and with YM-201636 treatment. Scale bars: 10 µm.

3.7.3 Knock-Down of ClC-7 Increases Lysosomal $[Cl^-]$

To reduce the expression of ClC-7 using shRNA-mediated knock-down, HEK293T cells were transfected with plasmid DNA with the sequence shown in table 2.2 two to three days prior to measurements.

The knock-down of ClC-7 significantly (*) increases the lysosomal $[Cl^-]$ to 173 ± 34 mM (SD) (figure 3.13 A). This result suggests that ClC-7 transports Cl^- out of the lysosome. Since Cl^- outward transport is coupled to H^+ uptake, one would expect a less acidic lysosomal pH in ClC-7 k.d. cells, but this was not observed, as shown in figure 3.13 (B). The reduced ClC-7-mediated lysosomal acidification might be compensated by an enhanced activity of the v-ATPases. Therefore, the effect of ClC-7 knock-down was examined after blocking the v-ATPases using 200 nM bafilomycin A1. Under these conditions, a lysosomal pH of 6.90 ± 0.65 (SD) was measured, which is significantly (**) higher than the lysosomal pH in untransfected cells treated with bafilomycin A1 (figure 3.13 C). This observation suggests that ClC-7 mediates proton uptake into the lysosomes, driven by the outward transport of Cl^-, which would also explain why lysosomes of untransfected cells do not exhibit a neutral pH after blocking the V-ATPase with bafilomycin A1, but are still slightly acidic (pH 6.29 ± 0.75 (SD), figure 3.13 C). Even though the v-ATPase is blocked, protons might still be transported into the lumen via ClC-7.

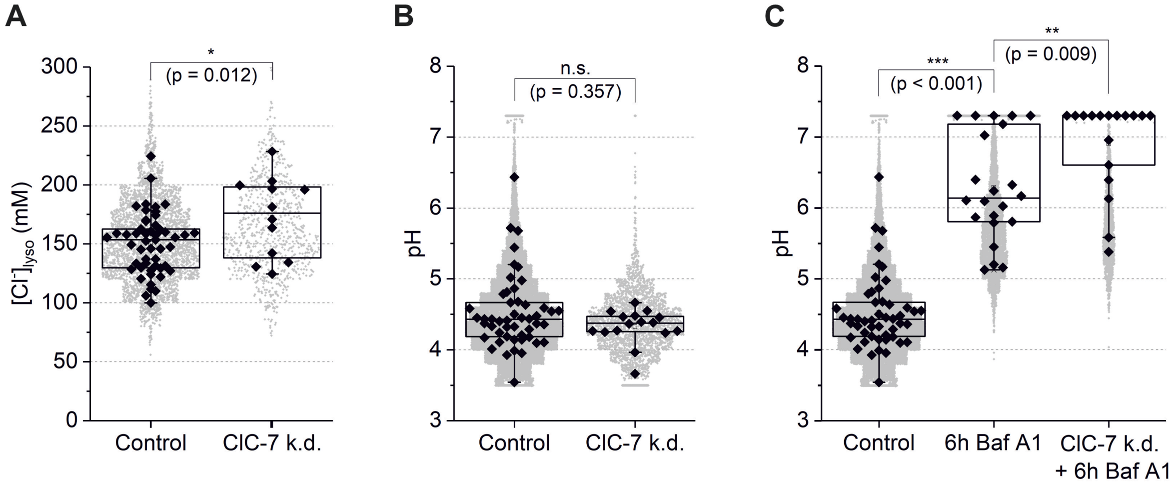

Figure 3.13: **Effect of ClC-7 k.d. on lysosomal $[Cl^-]$ and pH.** (A) Lysosomal $[Cl^-]$ measured with SPQ in normal-sized lysosomes of untransfected HEK293T cells (control) and cells, where ClC-7 has been knocked down (ClC-7 k.d.). (B) Corresponding lysosomal pH. (C) Lysosomal pH of normal-sized lysosomes of HEK293T cells (without YM-201636). The control was measured under normal conditions. The other two boxplots were measured after 6h incubation in medium supplemented with 200 nM bafilomycin A1 in lysosomes of untransfected cells and in lysosomes of cells, where ClC-7 has been knocked down (ClC-7 k.d.).

3.7.4 Simulations Can Partially Reproduce Experimental Results

Simulations using the mathematical model by Ishida et al. [4] could partially reproduce the experimental findings. Assuming a chloride permeability P_{Cl} of 1.2x10^{-5} cm/s [2], with decreasing numbers of CLCs the $[Cl^-]_{lyso}$ increases, which was also observed after knocking down ClC-7 expression (figure 3.14 A, red squares). As mentioned earlier, the proton permeability P_H of the lysosomal membrane presumably is quite high [95]. For simulations, it was set to $6.0 * 10^{-5}$ cm/s [4], but higher P_H than this were also tested and led to similar results (not shown).

At very high numbers of CLCs, a further increase of CLC-expression only slightly decreases $[Cl^-]_{lyso}$, which might be the reason why the overexpression of CLCs did not significantly change $[Cl^-]_{lyso}$. According to the simulations, higher expression levels of CLCs lead to a higher pH (figure 3.14 B, red squares). This was observed upon overexpression of CLCs, but is not in line with the experimental results after ClC-7 k.d. In experiments with Baf A1, the knock-down of ClC-7 further increased the lysosomal pH compared to untransfected cells treated with Baf A1. In the simulations, setting the number of v-ATPases to 0 leads to a neutral pH of 7.25 at any given number of CLCs (figure 3.14 B, blue circles). The model furthermore predicts increasing $[Na^+]_{lyso}$ and especially $[K^+]_{lyso}$ upon overexpression of CLCs (figure 3.14 C and D, red squares).

Table 3.2: **Parameters used for simulations.** For the initial $[Cl^-]$ a lower concentration than the extracellular $[Cl^-]$ was chosen. For the potassium and sodium permeability, values in the order of magnitude reported by Hartman et al. [2] were used, but with $P_{Na}/P_K \sim 0.3$ [3].

Parameter	Value	Reference
Temperature	37°C	Actual temp. during my experiments
Lysosome radius R	0.675 µm	Estimation from SPQ-images
Cytosolic pH	7.2	[101] [102]
Cytosolic $[K^+]$	145 mM	[103]
Cytosolic $[Cl^-]$	56 mM	Result from this study
Cytosolic $[Na^+]$	17.6 mM	[57]
Initial pH	7.4	pH of extracellular solution
Initial $[K^+]$	2.4 mM	$[K^+]$ in extracellular solution
Initial $[Cl^-]$	90 mM	
Initial $[Na^+]$	140 mM	$[Na^+]$ in extracellular solution
Proton permeability P_H	6.0×10^{-5} cm/s	[4]
Chloride permeability P_{Cl}	1.2×10^{-5} cm/s	[2]
Potassium permeability P_K	6.7×10^{-7} cm/s	
Sodium permeability P_{Na}	2.0×10^{-7} cm/s	
Water permeability P_W	0.052 cm/s	[104]

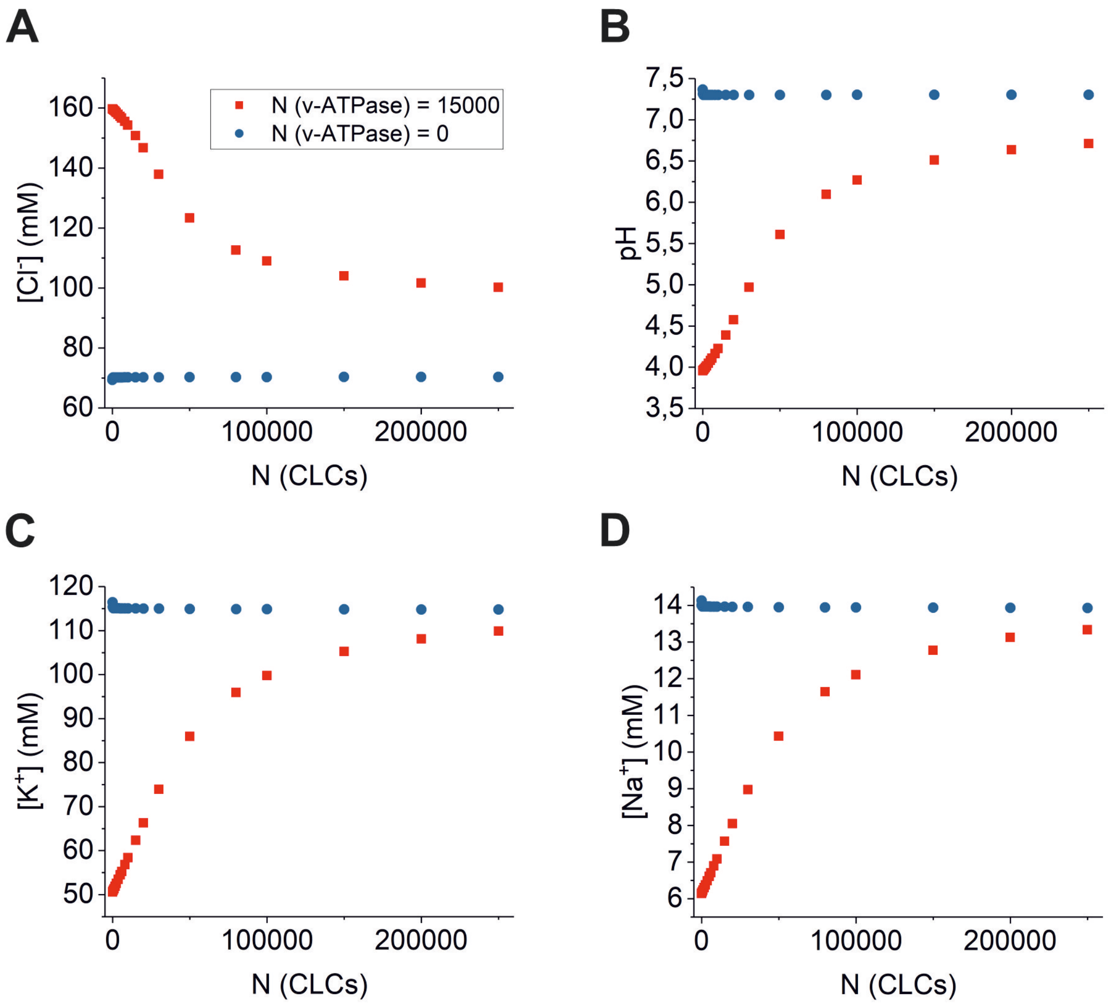

Figure 3.14: **Simulations of impact of CLC expression level.** Simulated lysosomal [Cl^-] (A), pH (B), [K^+] (C) and [Na^+] (D) plotted versus the number of CLCs, without bafilomycin A1 (red squares, 15000 v-ATPases) and with bafilomycin A1 (blue circles, 0 v-ATPases). Simulations were performed with the Berkeley Madonna model for lysosomal pH regulation, provided by Ishida et al. [4]. Parameters used for simulations are listed in table 3.2.

The experimental results from the chloride and pH measurements in cells expressing ClC-7 E245A could not be reproduced using the model by Ishida et al. The simulations predict higher lysosomal [Cl^-] and more acidic pH with the mutation than with WT ClC-7 (table 3.3), which contradicts the experimental findings.

Our knowledge about the parameters shown in table 3.2 is still lacking, so the chosen values might not be exactly right, and there might also still be unknown transport processes in the lysosome, which were not included in the model. This could explain the partial discrepancy between the experimental results and the simulations.

Table 3.3: **Simulated lysosomal ion concentrations with WT ClC-7 (1H$^+$:2Cl$^-$) and ClC-7 E245A (0H$^+$:1Cl$^-$).** Simulations were performed with the Berkeley Madonna model for lysosomal pH regulation, provided by Ishida et al. [4]. The parameters used for simulations are shown in table 3.2 (N v-ATPase = 15000, N CLCs = 16000).

	[Cl$^-$]	**pH**	**[K$^+$]**	**[Na$^+$]**
WT ClC-7	150 mM	4.42	63 mM	7.7 mM
E245A ClC-7	162 mM	3.94	54 mM	6.5 mM

3.8 Role of Other Cl$^-$-Transporters/Channels in Lysosomal Cl$^-$ Accumulation

Based on the previous results, ClC-7 might not be the main transporter through which chloride enters the lysosome. This gives rise to the question, which protein in the lysosomal membrane actually builds the passway for chloride to enter the lumen and leads to the high lysosomal [Cl$^-$].

In the following subchapters, three interesting potential candidates and their influence on the lysosomal [Cl$^-$] and pH are examined.

3.8.1 Overexpression of SLC26A11 Does Not Change Lysosomal [Cl$^-$]

SLC26A11 is a chloride transporter, that is expressed in several tissues including pancreas, brain, and kidney [105, 106, 107]. It has been proposed to function as anion channel in the surface membrane, that regulates neuronal cytoplasmic [Cl$^-$] under normal conditions [108] and builds a significant Cl$^-$ entry pathway during pathological swelling under brain ischemia [109].

SLC26A11 was identified as lysosomal protein in a recent mass spectrometry study. Although Xu et al. showed that SLC26A11 expression in the kidney is exclusively limited to the collecting duct [107], we observed vesicular expression of SLC26A11 in HEK293T cells (which are derived from human embryonic kidney, but not from the collecting duct) upon transfection with DNA encoding for SLC26A11. The confocal images in figure 3.15 (C) show that this expression colocalizes with the lysosomal marker LAMP1 (Pearsons's coefficient = 0.81 ± 0.05 (SD), N = 5 images, analyzed with JACoP plugin in Fiji, ImageJ [62, 63]), indicating lysosomal SLC26A11 localisation in HEK293T cells.

Since SLC26A11 is a chloride transporter, the transfection might have an impact on the lysosomal [Cl$^-$]. However, figure 3.15 (A) shows that $[Cl^-]_{lyso}$ is not significantly

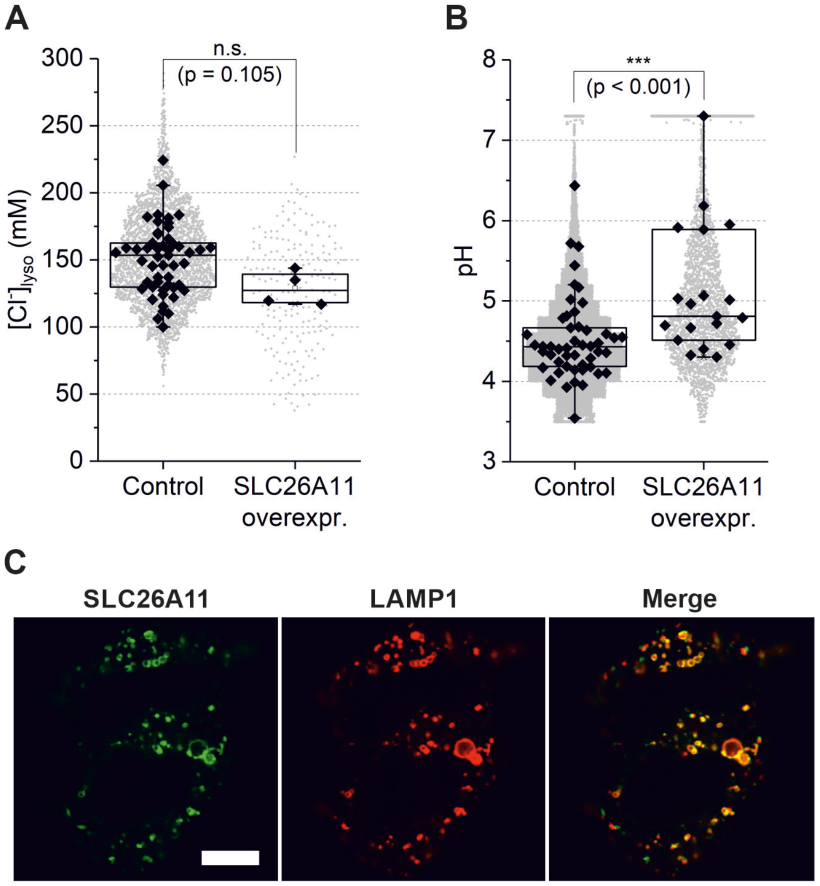

Figure 3.15: **Effect of overexpression of SLC26A11 on lysosomal [Cl$^-$] and pH.** (A) Lysosomal [Cl$^-$] measured with SPQ in normal-sized lysosomes (without YM-201636) of untransfected HEK293T cells (control) and cells overexpressing SLC26A11. (B) Corresponding lysosomal pH. (C) Confocal images of HEK293T cells transfected with SLC26A11 (with EGFP, green) and the lysosomal marker protein LAMP1 (with mCherry, red). Scale bar: 10 µm.

changed in transfected cells. Interestingly, with 5.10 ± 0.79 (SD) the pH in these cells is significantly (***) higher than in untransfected cells. The reason for this is unclear, maybe SLC26A11 exhibits a proton conductance in addition to its chloride transport function.

3.8.2 Sialin (SLC17A5) is Not Involved in Lysosomal Cl$^-$ Accumulation

Sialin (SLC17A5) is a H$^+$/sialic acid cotransporter, that transports protons and free sialic acid out of the lysosome [110, 111, 112]. In addition to that, in 2008, Moriyama et al. showed that sialin has an unexpected second function, as it is also able to import aspartate and glutamate into acidic organelles [113]. It belongs to the SLC17 family of organic anion transporters encompassing vesicular glutamate and nucleotide transporters, type 1 Na^+-dependent inorganic phosphate transporters, and sialin. Since vesicular glutamate transporters also function as proton-activated anion channels [114, 115], we tested the effect of sialin on lysosomal chloride and proton homeostasis.

Sialin was overexpressed or knocked down in HEK293T cells. For the knock down, two to three days prior to measurements, cells were transfected with plasmid DNA, the sequence of which is shown in table 2.2. The lysosomal pH significantly (***) increases upon sialin overexpression to 4.85 ± 0.49 (SD) (figure 3.16 B). This is not surprising, since sialin transports protons out of the lysosome. What is surprising is, however, that the k.d. of sialin only leads to a slight but not significant reduction of the lysosomal pH to 4.37 ± 0.26 (SD). The membrane potential might be slightly shifted towards more lumen positive values, due to reduced import of aspartate and glutamate into the lysosomes of cells in which sialin expression has been knocked down, so that the net-proton flux is practically unchanged in these cells.

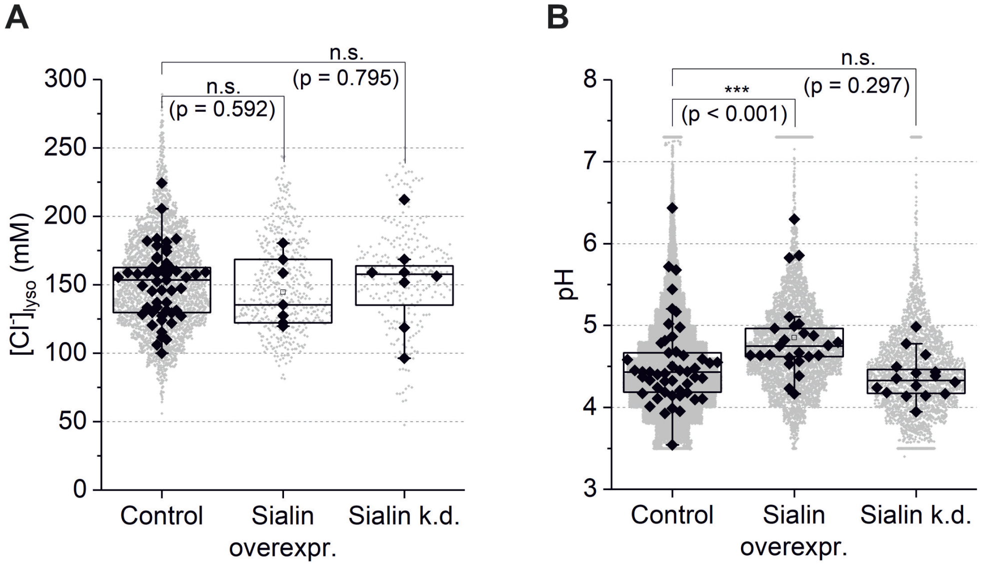

Figure 3.16: **Effect of Sialin overexpression and k.d. on lysosomal [Cl⁻] and pH.** (A) Lysosomal [Cl⁻] measured with SPQ in normal-sized lysosomes (without YM-201636) of untransfected HEK293T cells (control) and cells where sialin is overexpressed or knocked down. (B) Corresponding lysosomal pH.

Neither the overexpression nor the knock-down of sialin has a significant effect on the lysosomal [Cl⁻] (figure 3.16 A), so sialin does not seem to be involved in the regulation of luminal [Cl⁻] in HEK293T cells.

3.8.3 Knock-Down of PAC (TMEM206) Does Not Change Lysosomal [Cl$^-$]

PAC (TMEM206) has recently been identified as proton-activated chloride channel [116, 117]. In human epithelial HeLa cells, Wang et al. measured anion-selective whole-cell currents with a strong outward rectification, rapidly activated upon reduction of the extracellular pH below 5 [118].

Analogously, if PAC is present in the lysosomal membrane, it might carry an anion flux from the cytosol to the acidic lumen. Yang et al. report that the threshold for activation of PAC is pH 6.0 at 37°C [116]. Physiologically, such low pHs are only found in secretory vesicles or vesicles of the endocytic pathway, so Yang et al. argue that PAC might indeed traffic to the membrane of intracellular organelles, such as lysosomes, and play a role in the regulation of luminal [Cl$^-$] [116].

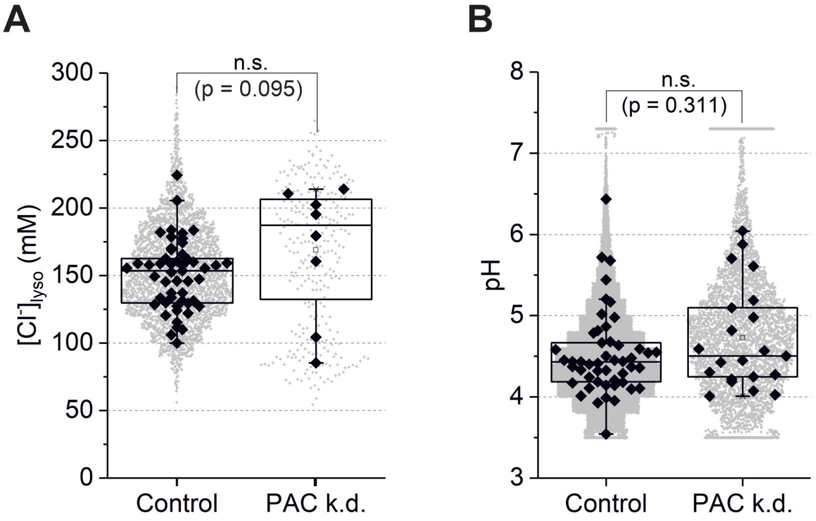

Figure 3.17: **Effect of PAC k.d. on lysosomal [Cl$^-$] and pH.** (A) Lysosomal [Cl$^-$] measured with SPQ in normal-sized lysosomes (without YM-201636) of untransfected HEK293T cells (control) and cells where PAC has been knocked down (PAC k.d.) (B) Corresponding lysosomal pH.

To investigate the possible role of PAC in the regulation of the lysosomal [Cl$^-$], HEK293T cells were transfected with plasmid DNA with the sequence shown in table 2.2 two to three days prior to measurements to knock down PAC expression. However, figures 3.17 (A) and (B) show that PAC k.d. neither has a significant effect on the lysosomal [Cl$^-$] nor on the pH, so PAC does not seem to be involved in the regulation of luminal [Cl$^-$] in HEK293T cells, possibly due to only low lysosomal expression of this protein.

3.9 Heterologous Expression of VGLUT1 in Lysosomes Decreases $[\mathrm{Cl}^-]_{lyso}$

Vesicular glutamate transporters are not endogenously expressed in lysosomes but rather in synaptic vesicles of glutamatergic neurons [119], where they transport glutamate, the major excitatory transmitter in the vertebrate nervous system, from the cytosol into the acidic lumen [115]. It has been shown that these transporters also function as proton-activated anion channels [114, 115], but the exact transport mechanisms are still not fully understood.

In attempts to target VGLUT1 to the plasma membrane by deleting the n-terminal of the sequence (aminoacids 1-62) and replacing aminoacids E(505) to V(511) in the c-terminal by alanine, an interesting discovery was made by colleagues from our institute. The transfection of HEK293T cells with this mutation leads to the expression of VGLUT1 in large vesicles. These large vesicles turn out to be lysosomes, as they colocalize with the lysosomal marker protein LAMP1 (figure 3.18 D).

Figure 3.18 (A) shows that cells expressing the mutated $\mathrm{VGLUT1}_{lyso}$ have significantly (*) higher cytosolic $[\mathrm{Cl}^-]_{cyto}$ of 67.8 ± 9.6 mM (SD) compared to untransfected cells. Strikingly, with 63.8 ± 13.7 mM (SD), the average lysosomal $[\mathrm{Cl}^-]_{lyso}$ in those cells is even lower than $[\mathrm{Cl}^-]_{cyto}$ (figure 3.18 B). The two representative fluorescence lifetime images in figure 3.18 (E), where the lifetimes of MEQ are represented by a color code ranging from orange (1 ns) to blue (4 ns), show this impressively. Usually, the fluorescence lifetime in the lysosomes is shorter than in the cytosol and therefore distinctly shifted towards orange (see figure 2.3 B), but in the images shown here, the lysosomes are shifted towards blue compared to the cytosol. However, the difference between $[\mathrm{Cl}^-]_{cyto}$ and $[\mathrm{Cl}^-]_{lyso}$ in cells expressing $\mathrm{VGLUT1}_{lyso}$ is not significant.

The expression of $\mathrm{VGLUT1}_{lyso}$ in the lysosomes also has an influence on the lysosomal pH. Figure 3.18 (C) shows that the lysosomal pH is significantly increased to 5.29 ± 0.68 (SD) in these cells.

Of course, VGLUT1 is not endogenously expressed in the lysosome, but these experiments might still help to understand the mechanism of pH- and $[\mathrm{Cl}^-]$-regulation in the lysosome or even the transport mechanism of WT VGLUT1, which is, as mentioned before, not entirely understood.

Since VGLUT1 exhibits anion channel function, its expression in the lysosomal membrane is expected to increase the chloride permeability P_{Cl}. Simulations using the model by Ishida et al. [4] show that the lysosomal $[\mathrm{Cl}^-]$ decreases with increasing P_{Cl},

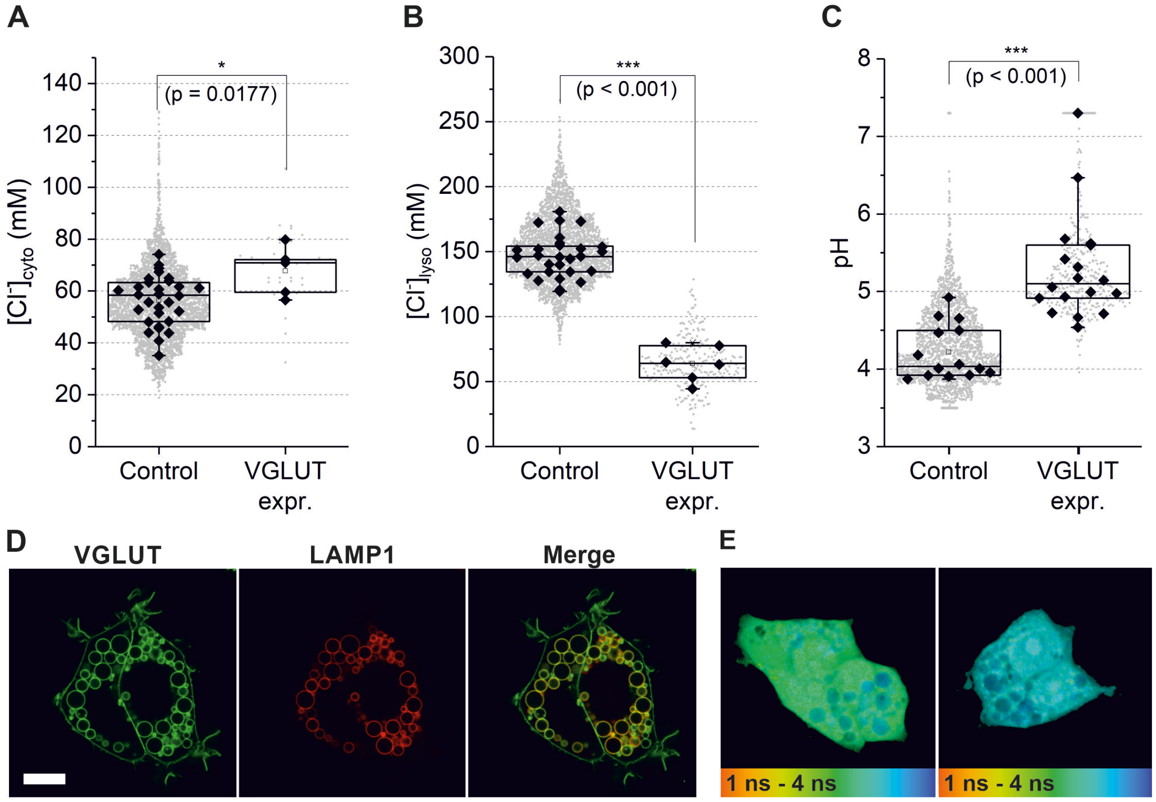

Figure 3.18: **Effect of expression of VGLUT1 in the lysosomal membrane.** (A) Cytosolic [Cl$^-$] measured with MEQ in untransfected HEK293T cells (control) and cells with VGLUT1 expression in the lysosomal membrane. (B) [Cl$^-$] measured with MEQ in enlarged lysosomes (with YM-201636) of untransfected HEK293T cells (control) and cells with VGLUT1 expression in the lysosomal membrane. Similar results were also observed with SPQ (not shown). (C) Corresponding lysosomal pH. (D) Representative confocal images of HEK293T cells transfected with VGLUT (green) and LAMP1 (red) (without YM-201636). Scale bar: 10 µm. (E) Two fluorescence lifetime images of HEK293T cells with VGLUT1 expression loaded with diH-MEQ, where the fluorescence lifetime within the lysosome is longer compared to the surrounding cytosol.

while the pH increases (figure 3.19). However, assuming a P_{Cl} of 1.2 x 10^{-5} cm/s, which leads to simulated [Cl$^-$] and pH close to the measured values in untransfected cells (red dots in figure 3.19), a further increase of P_{Cl} only slightly changes [Cl$^-$] and pH. The extreme decrease of [Cl$^-$] to ~64 mM and increase of pH to ~5.3 could not be reproduced by simply increasing P_{Cl}. Therefore, according to the simulations, the chloride channel function of VGLUT1 alone cannot explain the experimental findings.

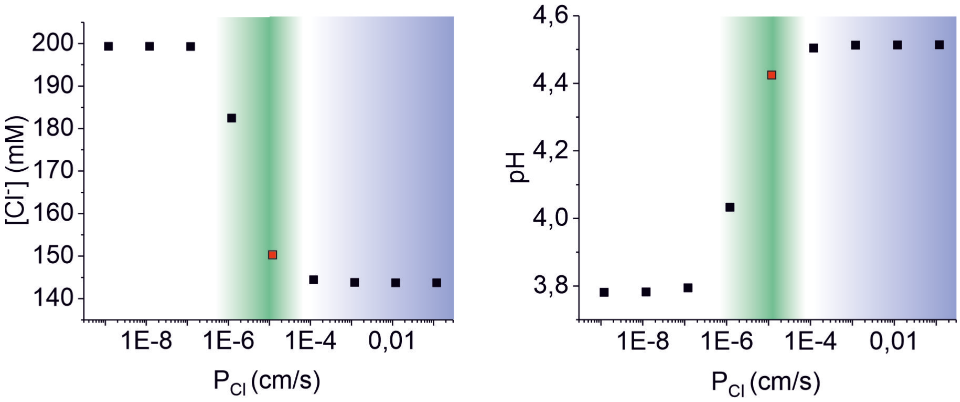

Figure 3.19: **Simulations of the impact of the chloride permeability P_{Cl}.** Simulated lysosomal [Cl$^-$], and pH plotted versus the chloride permeability P_{Cl} of the lysosomal membrane. Simulations were performed with the Berkeley Madonna model for lysosomal pH regulation, provided by Ishida et al. [4]. Parameters used for simulations are listed in table 3.2, with N CLCs = 16000 and N v-ATPase = 15000. The green background represents the values of P_{Cl} assumed to be close to the physiological value. The lysosomal [Cl$^-$] and pH simulated with P_{Cl} = 1.2 x 10^{-5} cm/s are close to the measured values under physiological conditions and are highlighted in red. The expression of VGLUT1$_{lyso}$ is expected to increase P_{Cl} (blue background).

3.10 Fusion of Lysosomes With Autophagosomes

In 2017, Chakraborty et al. showed that the depletion of lysosomal chloride directly correlates with a loss of the lysosome's degradative function and that a lower lysosomal [Cl$^-$] leads to a reduction of Ca^{2+} release from the lysosome [39], a process that is required for fusion of lysosomes with other compartments [30]. Hence, the experimental conditions from the previous chapters which lead to a reduction or an increase of lysosomal [Cl$^-$] might also have an influence on lysosomal fusion.

The fusion of lysosomes with autophagosomes was monitored using pftLC3. Under physiological conditions, 91.3% ± 4.1% (SD) of autophagosomes fuse with lysosomes (figure 3.20). In cells treated with Baf A1, a much lower percentage is expected, since Baf A1 is known to inhibit autophagosome-lysosome fusion [120]. Indeed, the measured percentage of fused autophagosomes is significantly lower (10.1% ± 13.4% (SD)) in cells treated with Baf A1 for 6 h. However, this result has to be interpreted with caution, since Baf A1 also increased the lysosomal pH to 6.29 ± 0.75 (SD) (chapter 3.5). Therefore, even if the autophagosomes fuse with the lysosomes, the pH in most of these lysosomes might not be low enough to quench the EGFP fluorescence sufficiently.

In cells expressing ClC-7 E245A or VGLUT1$_{lyso}$, the lysosomal pH was also increased, but only to 5.25 ± 0.64 (SD) and 5.29 ± 0.68 (SD), respectively. At this pH, the EGFP

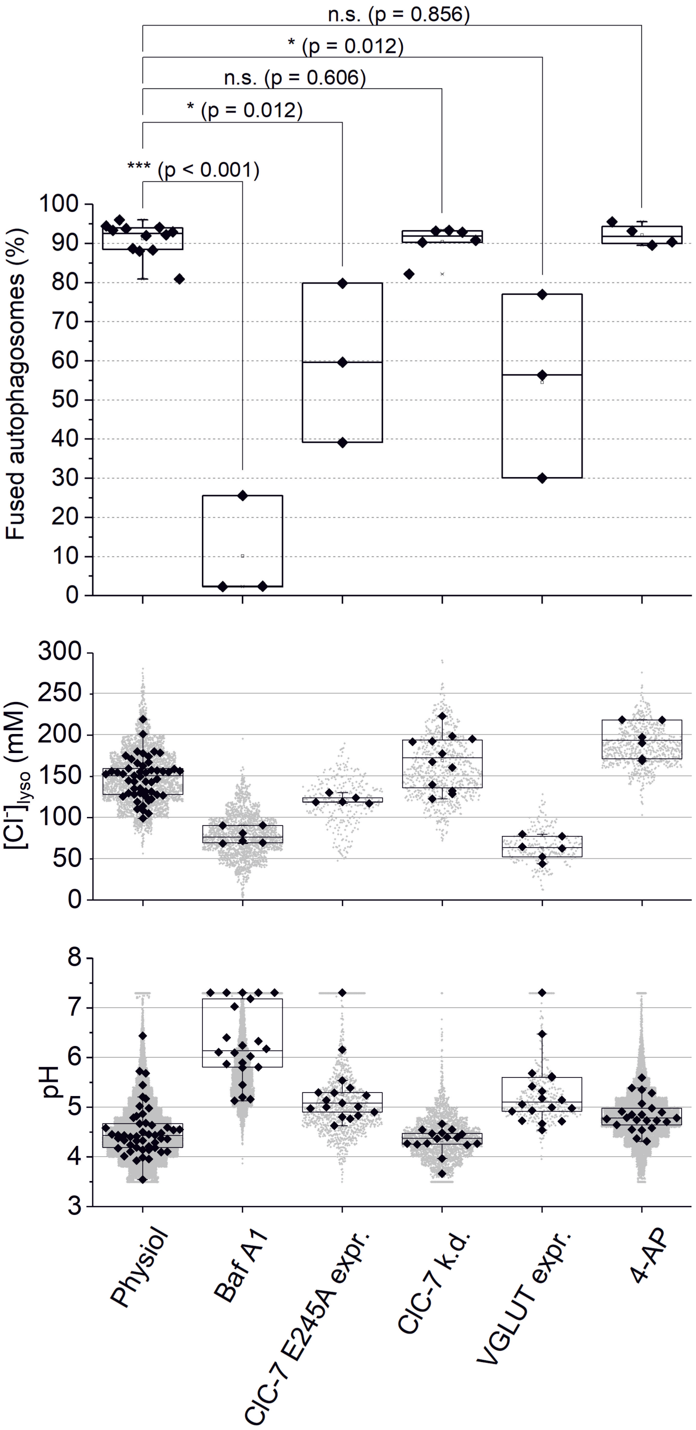

Figure 3.20: **Influence of different experimental conditions on lysosome-autophagosome fusion.** Percentage of fused autophagosomes, determined using pftLC3, and corresponding lysosomal [Cl$^-$] and pH from the previous chapters.

would still be sufficiently quenched, so, unlike the results with Baf A1, the pftLC3 results in these experiments are reliable. The lysosomal [Cl$^-$] in cells expressing ClC-7 E245A or VGLUT1$_{lyso}$ was decreased to 123 ± 6 mM (SD) and 64 ± 14 mM (SD), respectively (see chapters 3.7.2 and 3.9). ClC-7 E245A expression reduces the percentage of fused autophagosomes to 59.6% ± 20.3% (SD), and in cells expressing VGLUT1$_{lyso}$ only 54.5% ± 23.5% (SD) of the autophagosomes fuse with lysosomes. Hence, a lower [Cl$^-$] might indeed lead to an impairment of autophagosome-lysosome fusion. However, a possible role of the lysosomal pH on the impairment of the fusion mechanism cannot be excluded, since both ClC-7 E245A and VGLUT1$_{lyso}$ expression increased the pH to $>$ 5.2.

The knock-down of ClC-7 as well as the use of 4-AP increased lysosomal [Cl$^-$] to 173 ± 34 mM (SD) and 198 ± 23 mM (SD), respectively (chapters 3.7.3 and 3.6). While ClC-7 k.d. left the pH unaltered, the use of 4-AP led to an increase of the lysosomal pH, but only to 4.84 ± 0.32 (SD). Figure 3.20 shows that neither ClC-7 k.d. nor 4-AP treatment changes the percentage of fused autophagosomes. So, an increased lysosomal [Cl$^-$] does not seem to impair or enhance autophagosome-lysosome fusion.

3.11 Data

Table 3.4: **Data for calibration of SPQ in enlarged lysosomes of HEK293T cells (with YM-201636).**

[Cl$^-$]	**$1/\tau_{mean}$**	**SD**	**N (coverslips)**
30	0.402	0.035	4
40	0.446	0.029	4
50	0.449	0.036	4
60	0.494	0.023	5
70	0.494	0.043	5
80	0.526	0.019	4
90	0.566	0.021	3
100	0.573	0.019	3
110	0.624	0.023	4
120	0.647	0.026	3
130	0.665	0.011	3
140	0.708	0.007	3

Table 3.5: **Fitting parameters for calibration of SPQ in enlarged lysosomes of HEK293T cells (with YM-201636).**

Model	Linear fit
Equation	y = a + b*x
Intercept	0.322 ± 0.009
Slope	0.0027 ± 0.0001
Residual sum of squares	0.0014
Pearson's r	0.993
R-Square (COD)	0.987
Adj. R-Square	0.986

Table 3.6: **Data for calibration of SPQ in normal-sized lysosomes of HEK293T cells (without YM-201636).**

[Cl$^-$]	**1/τ_{mean}**	**SD**	**N (coverslips)**
30	0.287	0.023	3
40	0.325	0.020	3
50	0.341	0.006	3
60	0.350	0.008	3
70	0.402	0.014	3
80	0.408	0.022	3
90	0.449	0.005	3
100	0.497	0.027	3
110	0.488	0.023	3
120	0.519	0.013	3
130	0.540	0.014	3
140	0.577	0.002	3

Table 3.7: **Fitting parameters for calibration of SPQ in normal-sized lysosomes of HEK293T cells (without YM-201636).**

Model	Linear fit
Equation	y = a + b*x
Intercept	0.213 ± 0.009
Slope	0.0026 ± 0.0001
Residual sum of squares	0.001
Pearson's r	0.992
R-Square (COD)	0.985
Adj. R-Square	0.983

Table 3.8: **Data for calibration of MEQ in HEK293T cells (with YM-201636).**

[Cl$^-$]	**$1/\tau_{mean}$**	**SD**	**N (coverslips)**
10	0.182	0.012	3
20	0.209	0.009	3
30	0.242	0.013	3
40	0.254	0.011	3
50	0.277	0.021	3
60	0.301	0.010	3
70	0.329	0.015	4
80	0.366	0.011	3
90	0.375	0.011	3
100	0.420	0.027	3
110	0.452	0.023	3
120	0.451	0.038	3
130	0.471	0.021	3
140	0.518	0.011	3

Table 3.9: **Fitting parameters for calibration of MEQ in HEK293T cells (with YM-201636).**

Model	Linear fit
Equation	y = a + b*x
Intercept	0.157 ± 0.005
Slope	0.00253 ± 0.0006
Residual sum of squares	0.001
Pearson's r	0.996
R-Square (COD)	0.992
Adj. R-Square	0.992

Table 3.10: **Data for the exemplary pH calibration curve shown in figure 3.6.**

pH	**$\mathbf{I}_{OG}/\mathbf{I}_{TMR}$**	**SD**	**N (lysosomes)**
3.56	0.317	0.115	556
3.91	0.361	0.085	1012
4.21	0.451	0.070	734
4.54	0.553	0.085	1257
4.84	0.754	0.109	1307
5.12	0.852	0.118	1960
5.45	0.979	0.129	1393
5.64	1.086	0.144	1340
5.93	1.114	0.148	2125
7.26	1.282	0.190	1624

Table 3.11: **Fitting parameters for the exemplary pH calibration curve shown in figure 3.6.**

Model	DoseResp
Equation	y = A1 + (A2-A1)/(1+10$^{(pKa-pH)b}$)
A1	0.235 ± 0.043
A2	1.272 ± 0.043
pK$_a$	4.917 ± 0.061
b	0.832 ± 0.097
Reduced χ^2	0.049
R-Square (COD)	0.996
Adj. R-Square	0.994

Table 3.12: **Details on data of [Cl$^-$] measurements shown in figures 3.7 to 3.18.**

Figure	**Dye**	**Transfection/Treatment**	**YM-201636**	**Number of days**	**N (Number of coverslips)**	**Approx. number of cells**	**Number of lysosomes**	**Mean**	**SD**	**Median**
3.7 A	MEQ	physiol (cyto.)	yes	27	30	>3500	/	56.4	9.4	58.4
3.7 A	MEQ	physiol (lyso.)	yes	24	28	600	2951	147	16	146
3.7 A	SPQ	physiol	yes	13	22	400	2490	122	29	120
3.7 A	SPQ	physiol	no	37	51	600	3248	150	25	154
3.8 B	SPQ	Baf A1 (untrans.)	no	6	6	210	2007	79	11	76
3.8 B	SPQ	Baf A1 (no Arch3 expr.)	no	5	8	110	878	78	14	75
3.8 B	SPQ	Baf A1 (Arch3 expr.)	no	5	8	100	585	99	17	99
3.9 B	SPQ	4-AP	no	5	6	160	704	198	23	198
3.11 A	SPQ	ClC-7 overexpr.	no	5	7	80	292	143	7	142
3.11 A	SPQ	ClC-6 expr.	no	3	5	30	76	162	18	170
3.11 B	MEQ	ClC-3b overexpr.	no	4	6	80	379	126	34	131
3.12 A	SPQ	ClC-7 E245A	no	4	5	60	290	123	6	121
3.12 A	SPQ	ClC-7 Y746Q	no	4	6	80	276	164	15	171
3.13 A	SPQ	ClC-7 k.d.	no	5	12	190	807	173	34	176
3.17 A	SPQ	PAC k.d.	no	4	8	100	275	169	49	187
3.16 A	SPQ	Sialin overexpr.	no	4	7	130	483	145	24	135
3.16 A	SPQ	Sialin k.d.	no	6	8	80	263	153	34	158
3.15 A	SPQ	SLC26A11 expr.	no	4	4	50	188	129	13	127
3.18 A	MEQ	VGLUT expr. (cyto)	no	5	5	30	/	67.8	9.6	70.9
3.18 B	MEQ	VGLUT expr. (lyso)	no	5	6	40	243	63.8	13.7	64.0

Table 3.13: **Details on data of pH measurements shown in figures 3.7 to 3.18.**

Figure	**Transfection/Treatment**	**YM-201636**	**Number of days**	**N (Number of coverslips)**	**Approx. number of cells**	**Number of lysosomes**	**Mean**	**SD**	**Median**
3.7 B	physiol	no	22	49	>300	16793	4.52	0.52	4.43
3.7 B	physiol	yes	11	14	100	2290	4.22	0.35	4.03
3.8 A	Baf A1 (untrans.)	no	8	22	160	5632	6.29	0.75	6.14
3.9 B	4-AP	no	5	23	200	9123	4.84	0.32	4.78
3.11 D	ClC-7 overexpr.	no	3	13	70	1258	5.03	0.53	4.92
3.11 D	ClC-6 expr.	no	3	16	140	2443	4.55	0.36	4.54
3.11 E	ClC-3b overexpr.	no	9	44	150	1259	5.95	0.74	5.88
3.12 B	ClC-7 E245A	no	3	17	80	1180	5.25	0.64	5.08
3.12 B	ClC-7 Y746Q	no	4	19	90	1019	4.84	0.64	4.60
3.13 B	ClC-7 k.d.	no	4	16	110	2673	4.33	0.24	4.37
3.13 C	ClC-7 k.d., Baf A1	no	5	17	110	3120	6.90	0.65	7.3
3.17 B	PAC k.d.	no	4	21	160	4567	4.72	0.64	4.50
3.16 B	Sialin overexpr.	no	5	25	170	4555	4.85	0.49	4.75
3.16 B	Sialin k.d.	no	4	16	100	2874	4.37	0.26	4.33
3.15 B	SLC26A11 expr.	no	4	19	130	3007	5.10	0.79	4.81
3.18 C	VGLUT expr.	no	4	18	40	381	5.29	0.68	5.10

Table 3.14: **Statistical analysis of data shown in figures 3.7 to 3.13.**

Figure	Compared data		Normality test	Significance	Test
3.7 A	$[Cl^-]_{cyto}$ (MEQ)	$[Cl^-]_{lyso}$ (MEQ, YM-201636)	passed	*** ($p < 0.001$)	M.-W.
3.7 A	$[Cl^-]_{lyso}$ (MEQ, YM-201636)	$[Cl^-]_{lyso}$ (SPQ, YM-201636)	passed	** ($p = 0.002$)	M.-W.
3.7 A	$[Cl^-]_{lyso}$ (MEQ, YM-201636)	$[Cl^-]_{lyso}$ (SPQ, without YM-201636)	passed	n.s. ($p = 0.398$)	M.-W.
3.7 A	$[Cl^-]_{lyso}$ (SPQ, YM-201636)	$[Cl^-]_{lyso}$ (SPQ, without YM-201636)	passed	*** ($p < 0.001$)	t-test
3.7 B	pH (Physiol. without YM-201636)	pH (Physiol, with YM-201636)	failed	* ($p < 0.023$)	M.-W.
3.8 A	pH (control)	pH (Baf)	failed	*** ($p < 0.001$)	M.-W.
3.8 B	$[Cl^-]_{lyso}$ (control)	$[Cl^-]_{lyso}$ (Baf)	passed	*** ($p = 8.31E-9$)	t-test
3.8 B	$[Cl^-]_{lyso}$ (control)	$[Cl^-]_{lyso}$ (Arch3-Expr, Baf)	passed	*** ($p = 1.2E-5$)	t-test
3.8 B	$[Cl^-]_{lyso}$ (no Arch3-Expr, Baf)	$[Cl^-]_{lyso}$ (Arch3-Expr, Baf)	passed	* ($p = 0.0383$)	t-test
3.9 A	$[Cl^-]_{lyso}$ (control)	$[Cl^-]_{lyso}$ (4-AP)	passed	*** ($p = 4.3E-5$)	t-test
3.9 B	pH (control)	pH (4-AP)	failed	*** ($p < 0.001$)	M.-W.
3.11 A	$[Cl^-]_{lyso}$ (control)	$[Cl^-]_{lyso}$ (ClC-7 overexpr.)	passed	n.s. ($p = 0.352$)	M.-W.
3.11 A	$[Cl^-]_{lyso}$ (control)	$[Cl^-]_{lyso}$ (ClC-6 expr.)	passed	n.s. ($p = 0.332$)	t-test
3.11 B	$[Cl^-]_{lyso}$ (control)	$[Cl^-]_{lyso}$ (ClC-3b overexpr.)	passed	n.s. ($p = 0.168$)	M.-W.
3.11 D	pH (control)	pH (ClC-7 overexpr.)	failed	*** ($p = 0.001$)	M.-W.
3.11 D	pH (control)	pH (ClC-6 expr.)	failed	n.s. ($p = 0.527$)	M.-W.
3.11 E	pH (control)	pH (ClC-3b overexpr.)	failed	*** ($p < 0.001$)	M.-W.
3.12 A	$[Cl^-]_{lyso}$ (control)	$[Cl^-]_{lyso}$ (ClC-7 E245A expr.)	passed	* ($p = 0.0235$)	t-test
3.12 A	$[Cl^-]_{lyso}$ (control)	$[Cl^-]_{lyso}$ (ClC-7 Y746Q expr.)	passed	n.s. ($p = 0.212$)	t-test
3.12 B	pH (control)	pH (ClC-7 E245A expr.)	failed	*** ($p < 0.001$)	M.-W.
3.12 B	pH (control)	pH (ClC-7 Y746Q expr.)	failed	* ($p = 0.021$)	M.-W.
3.13 A	$[Cl^-]_{lyso}$ (control)	$[Cl^-]_{lyso}$ (ClC-7 k.d.)	passed	* ($p = 0.012$)	t-test
3.13 B	pH (control)	pH (ClC-7 k.d.)	failed	n.s. ($p = 0.357$)	M.-W.
3.13 C	pH (Baf)	pH (Baf, ClC-7 k.d.)	passed	** ($p = 0.009$)	M.-W.

Table 3.15: **Statistical analysis of data shown in figures 3.17 to 3.18**

Figure	**Compared data**		**Normality test**	**Significance**	**Test**
3.17 A	$[Cl^-]_{lyso}$ (Control)	$[Cl^-]_{lyso}$ (PAC k.d.)	passed	n.s. ($p = 0.095$)	M.-W.
3.17 B	pH (Control)	pH (PAC k.d.)	failed	n.s. ($p = 0.311$)	M.-W.
3.16 A	$[Cl^-]_{lyso}$ (control)	$[Cl^-]_{lyso}$ (Sialin overexpr.)	passed	n.s. ($p = 0.592$)	t-test
3.16 A	$[Cl^-]_{lyso}$ (control)	$[Cl^-]_{lyso}$ (Sialin k.d.)	passed	n.s. ($p = 0.795$)	t-test
3.16 B	pH (control)	pH (Sialin overexpr.)	failed	*** ($p < 0.001$)	M.-W.
3.16 B	pH (control)	pH (Sialin k.d.)	failed	n.s. ($p = 0.297$)	M.-W.
3.15 A	$[Cl^-]_{lyso}$ (control)	$[Cl^-]_{lyso}$ (SLC26A11 overexpr.)	passed	n.s. ($p = 0.105$)	t-test
3.15 B	pH (control)	pH (SLC26A11 overexpr.)	failed	*** ($p < 0.001$)	M.-W.
3.18 A	$[Cl^-]_{cyto}$ (control)	$[Cl^-]_{cyto}$ (VGLUT expr.)	passed	* ($p = 0.0177$)	t-test
3.18 B	$[Cl^-]_{lyso}$ (control)	$[Cl^-]_{lyso}$ (VGLUT expr.)	passed	*** ($p = 4.65E-13$)	t-test
3.18 A+B	$[Cl^-]_{lyso}$ (VGLUT expr.)	$[Cl^-]_{cyto}$ (VGLUT expr.)	passed	n.s. ($p = 0.601$)	t-test
3.18 C	pH (control)	pH (VGLUT expr.)	failed	*** ($p < 0.001$)	M.-W.

Table 3.16: **Details on pftLC3 data shown in figure 3.20.**

Condition	**Number of days**	**Number of coverslips (N)**	**Number of cells**	**Vesicles with GFP signal/cell**	**Vesicles with RFP signal/cell**	**Mean percentage of fused autophagosomes**	**SD**	**Median**
Physiol	7	12	269	0.80	9.10	91.3	4.1	92.6
Baf A1	3	3	79	15.97	17.12	10.1	13.4	2.4
ClC-7 E245A expr.	3	3	71	3.29	9.57	59.6	20.3	59.6
ClC-7 k.d.	3	6	108	0.87	8.72	90.5	4.3	91.9
VGLUT expr.	3	3	72	4.76	11.38	54.5	23.5	56.4
4-AP	3	4	76	0.72	8.99	92.2	2.8	91.8

Table 3.17: **Statistical analysis of data shown in figure 3.20.**

Compared data		**Normality test**	**Significance**	**Test**
Physiol	Baf A1	passed	*** (p = 5.76E-11)	t-test
Physiol	ClC-7 E245A expr.	failed	* (p = 0.012)	M.-W.
Physiol	ClC-7 k.d.	failed	n.s. (p = 0.606)	M.-W.
Physiol	VGLUT expr.	failed	* (p = 0.012)	M.-W.
Physiol	4-AP	failed	n.s. (p = 0.856)	M.-W.

3.12 Overview Over All Results of Chloride- and pH-Measurements

Table 3.18: **Overview over all results of chloride- and pH-measurements.**

Chapter	**Cl^--sensor**	**Transfection/Treatment**	**YM-201636**	**$[Cl^-]_{cyto}$ (mM)**	**$[Cl^-]_{lyso}$ (mM)**	**Lysosomal pH**
3.4	MEQ	physiol	yes	56.4 ± 9.4	147 ± 16	4.22 ± 0.35
3.4	SPQ	physiol	yes		122 ± 29	4.22 ± 0.35
3.4	SPQ	physiol	no		150 ± 25	4.52 ± 0.52
3.5	SPQ	Baf A1 (untrans.)	no		79 ± 11	6.29 ± 0.75
3.5	SPQ	Baf A1 (Arch3 expr.)	no		99 ± 17	
3.6	SPQ	4-AP	no		198 ± 23	4.84 ± 0.32
3.7.1	SPQ	ClC-7 overexpr.	no		143 ± 7	5.03 ± 0.53
3.7.1	SPQ	ClC-6 expr.	no		162 ± 18	4.55 ± 0.36
3.7.1	MEQ	ClC-3b overexpr.	no		126 ± 34	5.95 ± 0.74
3.7.2	SPQ	ClC-7 E245A	no		123 ± 6	5.25 ± 0.64
3.7.2	SPQ	ClC-7 Y746Q	no		164 ± 15	4.84 ± 0.64
3.7.3	SPQ	ClC-7 k.d.	no		173 ± 34	4.33 ± 0.24
3.8.3	SPQ	PAC k.d.	no		169 ± 49	4.72 ± 0.64
3.8.2	SPQ	Sialin overexpr.	no		145 ± 24	4.85 ± 0.49
3.8.2	SPQ	Sialin k.d.	no		153 ± 34	4.37 ± 0.26
3.8.1	SPQ	SLC26A11 expr.	no		129 ± 13	5.10 ± 0.79
3.9	MEQ	VGLUT expr.	no	67.8 ± 9.6	63.8 ± 13.7	5.29 ± 0.68

Chapter 4

Discussion

4.1 Physiological [Cl$^-$] in Cytosol and Lysosomes of HEK293T Cells

In this study, a method was established to quantitatively measure lysosomal chloride concentrations in HEK293T cells via fluorescence lifetime imaging microscopy (FLIM), using the chloride sensitive dyes MEQ and SPQ.

Thus far, our knowledge about the ionic composition in the lysosomes is insufficient. Lysosomes exhibit a very acidic pH, which impedes the use of genetically encoded biosensors for measuring ion concentrations in these organelles. Most commonly used chloride sensors, such as Cl-Sensor [51] and Clomeleon [52], are highly pH-sensitive [58, 121] or only reliable over a limited range of chloride concentrations. The quinolinium-based chloride-sensitive dyes MEQ and SPQ [1, 58, 61, 122], on the other hand, are unaffected by protons as well as by other cations. Moreover, they function by collisional quenching and are therefore sensitive to chloride over a broad range of concentrations [1, 86, 123, 124, 125], making them perfectly suited for studying even large alterations of [Cl$^-$]. However, the challenge is to target these dyes to the lysosomes.

SPQ is membrane-impermeant and enters the cell via endocytosis. In this study, it was demonstrated that incubation of cells in SPQ-supplemented medium for 2 h followed by a short chasing time results in accumulation of SPQ in the lysosomes, which was verified by colocalization experiments with fluorescently labeled dextran (figure 3.1). Whereas the vast majority of SPQ-filled vesicles is also loaded with dextran, not every dextran-positive vesicle contains SPQ, possibly due to preferential filling of certain lysosomal populations [126].

Therefore, we additionally established a method in which the distribution of the chloride-sensor does not depend on endocytosis: diH-MEQ, the reduced form of MEQ, is membrane permeable and thus enters the cell and all cell organelles via diffusion, where it rapidly reoxidizes to the Cl^--sensitive and membrane impermeant MEQ [1]. Incubation of cells in medium supplemented with diH-MEQ results in homogeneous staining of the whole cell with MEQ with seemingly similar fluorescence lifetimes in all cell compartments (figure 3.2 B). This result does not contradict organelle-specific chloride concentrations, but rather illustrates the difficulties to separate fluorescence signals arising from small and mobile organelles from cytoplasmic signals. To be able to distinguish lysosomal MEQ fluorescence lifetimes from those of other sources, the PIKfyve inhibitor YM-201636 was used to increase the lysosomal size [68]. This approach indeed revealed large vesicular structures visible in the fluorescence lifetime image, which colocalize with the lysosomal marker protein LAMP1 (figure 3.3). Increasing the lysosomal size additionally reduces the diffusion velocity of the lysosomes, thus supporting accurate determination of fluorescence lifetimes by time correlated single photon counting.

The comparison of lysosomal $[Cl^-]$ measured with the two different dyes, SPQ and MEQ, makes the results less susceptible to potential sources of error, such as selective accumulation of SPQ in only a subset of lysosomes, modification of lysosomal ion concentrations by YM-201636-mediated enlargement, or inaccuracies of photon counting due to the lysosomal mobility.

The lysosomal $[Cl^-]_{lyso}$ measured in HEK293T cells with the two different sensors, SPQ and MEQ, are quite similar. With MEQ, a $[Cl^-]_{lyso}$ of 147 ± 16 mM was obtained in enlarged lysosomes. Measurements with SPQ revealed $[Cl^-]_{lyso}$ of 150 ± 25 mM in lysosomes with normal size (figure 3.7 A).

The use of YM-201636 reduced the $[Cl^-]_{lyso}$ measured with SPQ to 122 ± 29 mM. The vesicles examined in this work are most likely a mixture of late endosomes and lysosomes in unperturbed cells, but the treatment of cells with YM-201636 might partially disturb the mechanisms by which SPQ enters into and distributes within the endolysosomal system. This could lead to a higher relative amount of SPQ-filled late endosomes than lysosomes in cells treated with YM-201636, which might explain the lower $[Cl^-]$. However, apart from this, the SPQ-experiments in this study have been performed without the use of YM-201636 and the measurements with MEQ are not expected to be affected by

YM-201636 in the same way, since diH-MEQ is membrane permeable and enters the lysosomes via diffusion.

MEQ offers the possibility to simultaneously monitor [Cl^-] in the lysosome and the cytosol. In this work, an average cytosolic [Cl^-] of 56.4 ± 9.4 mM was measured. Previously published cytosolic chloride concentrations in various mammalian cell types are widespread and range from around 10 mM [127, 128] to 100 mM [129], with most values between 20 mM and 60 mM. For example, $[\mathrm{Cl}^-]_{cyto}$ in mouse pyramidal neurons decrease with age from 54 mM (P4-P5) to 17 mM (P18-P51) [130]. In dorsal root ganglion neurons of mice, Gilbert et al. report on $[\mathrm{Cl}^-]_{cyto}$ of 77 mM (P1-P4) or 62 mM (adult) [88]. Zhou et al. obtained average $[\mathrm{Cl}^-]_{cyto}$ of 30 mM in an embryo rat aortic vascular smooth muscle cell line [131]. Koncz et al. report on 32 mM chloride in the cytosol of vascular smooth muscle cells [132]. In Bergmann glial cells Untiet et al. measured 35 mM chloride [125]. Results by Kaneko et al. demonstrate $[\mathrm{Cl}^-]_{cyto}$ of 40-50 mM in the cytosol of mammalian olfactory sensory neurons [86]. Treharne et al. revealed $[\mathrm{Cl}^-]_{cyto}$ of 40-50 mM in epithelia cells [133]. In the zona glomerulosa of mouse adrenal gland Scholl et al. measured $[\mathrm{Cl}^-]_{cyto}$ of 75 mM [124]. Sonawane et al. obtained 44 mM in J774 cells and 47 mM in CHO cells [87].

Thus far, only few publications on quantitative lysosomal chloride concentrations exist. Using MQAE, Hosogi et al. measured $[\mathrm{Cl}^-]_{lyso}$ of approx. 28 mM in a model cancer cell line (MKN28) under physiological conditions [134], but their results should be interpreted with caution for several reasons: MQAE is membrane permeable and stains the cytosol as well as possibly cell organelles. However, in experiments our group performed with MQAE in HEK293T cells, this dye did not accumulate in the lysosomes but in the mitochondria [74]. Furthermore, Hosogi et al. did not increase the size of the vesicles, so the cytosolic MQAE signal might overlap the signal originating from small organelles. To localize the positions of lysosomes, Hosogi et al. used acridine orange, a dye that in cells is retained in acidic cellular compartements, but has been shown to be fairly phototoxic [135]. Moreover, they used the fluorescence intensity of MQAE as a readout for [Cl^-]. The fluorescence intensity is directly proportional to the amount of fluorophore molecules, which is hard to control in cells and cell organelles. To overcome this problem, a ratiometric reference can be used, which apparently was not done by Hosogi et al. [134].

Weinert et al. conjugated MEQ to dextran in order to target the sensor to the lysosomes, but this conjugation severely reduced the sensitivity of MEQ above 60 mM Cl^-, and they could not obtain quantitative values [38].

In 2019, Park et al. manipulated MQAE for lysosomal targeting, by linking the quinolinium fluorophore to a lysosome-targeting morpholine group, and qualitatively measured changes in $[\mathrm{Cl}^-]_{lyso}$ of HeLa cells upon application of several substances [136].

Recently, Saha et al. developed a chloride-sensitive DNA "nanodevice" called Clensor [28]. This is, to my knowledge, thus far the only other chloride sensor which has been successfully used for quantitative measurements of lysosomal chloride concentrations. Clensor is composed of a sensing, a normalizing, and a targeting module [28]. The sensing module of Clensor is a peptide nucleic acid (PNA) sequence conjugated to the fluorescent, chloride-sensitive molecule BAC (10,10-bis[3-carboxypropyl]-9,9-biacridinium dinitrate), which is pH-insensitive [87]. For ratiometric chloride measurements, Clensor also contains a DNA sequence for binding of the chloride insensitive fluorophore Alexa 647. Clensor can specifically be targeted to compartments of the endocytic pathway, including the lysosomes, by binding to scavenger receptors and following the scavenger receptor-mediated endocytic pathway. Using this new device, in 2015, Saha et al. were able to measure $[\mathrm{Cl}^-]_{lyso}$ of approx. 109 mM in haemocytes of *Drosophila* larvae [28]. With the same sensor, Chakraborty et al. obtained $[\mathrm{Cl}^-]_{lyso}$ of 75 mM in the lysosomes of coelomocytes of *Caenorhabditis elegans* and approx. 118 mM in human and murine macrophages [39]. So, with the exception of the results by Hosogi et al. [134], the lysosomal $[\mathrm{Cl}^-]_{lyso}$ published thus far are considerably higher than cytosolic or endosomal $[\mathrm{Cl}^-]$ [28, 87].

With approx. 150 mM, the lysosomal $[\mathrm{Cl}^-]_{lyso}$ measured in HEK293T cells in this work are even higher. As indicated earlier, only a subset of lysosomes is loaded with SPQ (figure 3.1). Several studies have considered that there are sub-populations of lysosomes, which exhibit different behaviours and functions [8, 126, 137]. Many cell types have evolved specialized lysosomes with distinct function, e.g. melanosomes in skin cells [138] or azurophil granules in neutrophils [139]. Recently, Leung et al. [126] developed a new DNA nanodevice, ChloropHore, by combining Clensor with a pH-reporter domain, called I-switch, which undergoes a pH-dependent conformational change, that leverages Förster resonance energy transfer (FRET) [39]. Using this new sensor they were able to ratiometrically image pH and chloride simultaneously in the same lysosomes and revealed two major lysosome populations in human primary skin fibroblasts – a lower-chloride/lower-acidity population and a high-chloride/high-acidity population (absolute values were not provided). Interestingly, the latter was absent in primary cells derived from patients with Niemann-Pick disease, which belongs to the lysosomal storage diseases [126].

Based on these findings, it would be conceivable that the subset of lysosomes filled with SPQ belongs to a population of lysosomes with higher $[\mathrm{Cl}^-]$ and higher acidity. On the other hand, the equally high $[Cl^-]_{lyso}$ measured with MEQ contradict this hypothesis, because it is unlikely that diH-MEQ only diffuses into a subset of lysosomes. Hence, the preferential filling of certain lysosomal populations is probably not the reason for the higher $[Cl^-]_{lyso}$ measured in this work, compared to hitherto reported lysosomal $[Cl^-]_{lyso}$. However, with their results, Chakraborty et al. showed that $[Cl^-]_{lyso}$ is cell type dependent [39], like it is also the case for $[Cl^-]_{cyto}$. Furthermore, the simultaneous measurements of lysosomal and cytosolic $[Cl^-]$ with MEQ in my study revealed that higher $[Cl^-]_{cyto}$ are accompanied by higher $[Cl^-]_{lyso}$ (figure 3.7 B), and the obtained $[Cl^-]_{cyto}$ in HEK293T cells are relatively high as well.

Lysosomes express multiple transport proteins that mediate the transmembrane passage of Cl^- and H^+/OH^-, thus linking lysosomal pH and $[Cl^-]$. To study the interdependence of lysosomal H^+ and Cl^- homeostasis, $[Cl^-]$-measurements were combined with an established technique to quantify lysosomal pH. Under physiological conditions, ratiometric fluorescence intensity measurements with TMR- and OG-dextran revealed an average lysosomal pH of 4.52 ± 0.52 for normal-sized lysosomes and of 4.22 ± 0.35 in YM-201636-enlarged lysosomes (figure 3.7 C). These values are consistent with lysosomal pH values determined before by other groups [19, 90, 91]. Especially, enlarged vacuoles were reported to exhibit a hyperacidic pH in fibroblasts lacking FIG4, a PI(3,5)P2 biosynthetic factor [92].

4.2 Lysosomes Accumulate Cl^- via an Electrogenic Transport Process

The high lysosomal $[Cl^-]$ observed in this and other studies are close to extracellular concentrations, suggesting that they originate from endocytosis of the external medium, rather than from transporter-mediated Cl^--accumulation. There are, however, multiple observations that contradict this hypothesis.

Sonawane et al. measured low $[Cl^-]$ of ∼25 mM in early endosomes of J774 cells shortly after formation in a high extracellular $[Cl^-]$ of ∼140 mM. They explain this by an interior-negative Donnan potential at the inner surface of the endosomal membrane, which leads to an extrusion of anions during endocytosis [93]. Experiments with haemocytes of *Drosophila* larvae revealed increasing vesicular $[Cl^-]$ from 37 mM to 109 mM during endolysosomal maturation [28]. In this study, incubation of cells in extracellular solution with low $[Cl^-]$ of 5.4 mM for 3 h resulted in similar lysosomal chloride concentrations as under control conditions (supplementary figure A.1). Taken together, these experimental results strongly support active lysosomal Cl^- accumulation during endolysosomal maturation.

As shown in chapter 3.5, the v-ATPases might provide the driving force for this Cl^- accumulation in lysosomes. Using the energy of ATP, they acidify the lumen and build up a lumen positive potential by actively pumping protons into the lysosome. Inhibition of the v-ATPases using bafilomycin A1 did not only increase the lysosomal pH from 4.52 ± 0.52 to 6.29 ± 0.75 (figure 3.8 A), but also resulted in a severe reduction of $[Cl^-]_{lyso}$ from 150 ± 25 mM to 79 ± 11 mM (figure 3.8 B). A similar result has been observed before by Hara-Chikuma et al. in endosomes [94]. They used the Cl^--sensitive dye BAC conjugated to dextran and either transferrin (targets to early/recycling endosomes) or α_2-macroglobulin (targets to late endosomes). Together with the Cl^--insensitive dye TMR, they ratiometrically measured the chloride concentration in endosomes of hepatocytes from mice right after endocytosis and during the maturation to early/recycling or late endosomes. Without bafilomycin A1 they obtained a final $[Cl^-]$ of 46 mM in early/recycling endosomes and 58 mM in late endosomes, whereas in cells treated with bafilomycin A1 the $[Cl^-]$ remained as low as approx. 20 mM.

Using the light-driven proton pump Archaerhodopsin-3 (Arch3), in 2015, Rost et al. were able to optogenetically reacidify lysosomes of HEK293 cells which had been treated with bafilomycin A1 [95]. The same approach was used in this work to rescue the $[Cl^-]_{lyso}$ in cells treated with bafilomycin A1. Indeed, $[Cl^-]_{lyso}$ significantly increased to 99 ± 17 mM upon activation of Arch3 in the lysosomal membrane, but the high physiological $[Cl^-]_{lyso}$ of approx. 150 mM was not reached (figure 3.8 B), possibly due to low expression levels and/or transport rates of the optogenetic proton pump. Furthermore, Rost et al. showed that the lysosomal acidification in their experiments required constant pumping, indicating a strong proton leak in lysosomes [95]. Therefore, during the 80 s recordings at 750 nm, which is not the optimal wavelength for the activation of Arch3, this proton leak might have caused lysosomal alkalinization and chloride efflux.

Lysosomes are known to exhibit a significant K^+ conductance, that contributes to the lysosomal membrane potential [91, 97, 98]. The potassium conductance is mainly mediated by the K^+ channel TMEM175, which can be blocked by 4-aminopyridine (4-AP) [98]. The use of 4-AP leads to a significant increase of $[Cl^-]_{lyso}$ to 198 ± 23 mM (figure 3.9 A), probably due to a depolarization of the lysosomal lumen resulting from the blocked K^+-efflux, which allows an enhanced influx of Cl^-. This could also be shown in simulations using the model provided by Ishida et al. [4] (figure 3.10).

Taken together, these results suggest that lysosomes accumulate Cl^- in a secondary active process driven by the v-type ATPases. Chloride accumulation is electrogenic and directly modified by changes in the membrane potential.

4.3 $[\mathrm{Cl}^-]_{lyso}$ is Coupled to pH_{lyso} and Cl^- Partially Facilitates Lysosomal Acidification

The results from this work under different conditions show a correlation between lysosomal pH and $[\mathrm{Cl}^-]_{lyso}$: a higher $[\mathrm{Cl}^-]_{lyso}$ is generally accompanied by a more acidic pH (supplementary figure A.2). In the previous chapter, the contribution of the v-ATPase in the accumulation of chloride in the lysosome has been discussed. Conversely, the Cl^- influx might also facilitate the maintenance of the lysosomal pH, as it neutralizes the lumen positive potential built up by the v-ATPase.

A possible role of chloride as a counterion in intracellular vesicles with acidic pH has been suggested in several studies. Indeed, the disruption of ClC-5 in the endosomal membrane as well as the knock-out of ClC-3 in the membrane of synaptic vesicles impairs the acidification of endosomes and synaptic vesicles, respectively [31, 32]. In 2010 however, Steinberg et al. reported that lysosomes were able to re-acidify after protonophore-induced alkalinization, even when the chloride in the cytosol had been replaced with large organic anions which show a negligible permeability through most known Cl^--pathways [91]. Thus, they concluded that cytosolic anions are not essential for the acidification of lysosomes.

The ion flux that counters the lumen positive potential could be an inward flux of cytosolic anions, such as chloride, or an outward flux of cations out of the lysosome. In some studies, it has been proposed that especially potassium could play an important role in facilitating lysosome acidification [96, 97]. Indeed, in chapter 3.6 it was demonstrated that when blocking TMEM175, which is thought to be the main K^+-channel in the lysosomal membrane [98], by the use of 4-aminopyridine, the lysosomal acidification is slightly impaired as the pH increases to 4.84 ± 0.32 (figure 3.9 B). Similar results have also been shown by Cang et al. in TMEM175 k.o. cells [98]. With 4.84, however, the measured pH is still very acidic. As mentioned in the previous chapter, the use of 4-aminopyridine leads to a significant increase of $[\mathrm{Cl}^-]_{lyso}$ to 198 ± 23 mM (figure 3.9 A). Upon blocking the K^+-channel in the lysosomal membrane, the role of Cl^- as a counterion seems to become more important. Due to the blocked K^+-efflux, the lumen positive membrane potential might increase and allow an enhanced influx of Cl^-, by which the lysosomal pH can be stabilized and nearly rescued.

In summary, the results show that neither potassium nor chloride alone are essential for lysosomal acidification. Instead, both an outward flux of potassium and an inward flux of chloride seem to be able to counter the lumen positive potential built up by the v-ATPase and thus facilitate lysosomal acidification. To what extent these ion-fluxes contribute to the maintenance of the pH depends on the given conditions. Apparently, cells are able to dynamically adjust to different conditions, like variations in cytosolic [Cl^-], to maintain the acidic pH in the lysosome.

However, even though an influx of chloride and an efflux of potassium would equally dissipate the potential built up by the v-ATPase, the consequences of these processes on the osmotic pressure are opposed. Steinberg et al. speculate in their study that if the uptake of every proton was accompanied by the uptake of a chloride ion, the osmotic pressure would increase, which could possibly cause swelling or even rupture of the lysosomes [91]. Consistent with this assumption, a slight increase of the lysosomal size was indeed observed upon treatment of cells with 4-aminopyridine, as mentioned in chapter 3.6. In contrast to this, the efflux of potassium as a counterion would potentially lead to a reduction of the osmotic pressure and thus to lysosomal shrinking, because incoming protons are largely scavenged by the luminal buffer [91]. Therefore, a combination of both chloride and potassium as counterions might allow lysosomes to maintain their acidic pH as well as their osmolarity and volume.

4.4 ClC-7 Does Not Transport Chloride Into the Lysosomes of HEK293T Cells

The results discussed in chapter 4.2 indicate that Cl^- is accumulated via an electrogenic transport process, which I sought to identify in this study by overexpressing or knocking down certain candidate transport proteins.

The Cl^-/H^+ exchanger ClC-7 has been shown to be the main chloride transport protein in the lysosomal membrane [100]. Jentsch and coworkers suggested that ClC-7 transports chloride into and protons out of the lysosome [33, 38]. There are studies which support this hypothesis. In fibroblasts of mice, Weinert et al. observed reduced $[Cl^-]_{lyso}$ in ClC-7 k.o. lysosomes compared to WT [38]. However, these results should be interpreted with caution because of the low sensitivity of their fluorescence indicator at lysosomal [Cl^-] above ∼60 mM. Weinert et al. therefore tried to modify lysosomal [Cl^-] by incubating cells in low external [Cl^-] of 7 mM, which might have unwanted effects that influence the effect of ClC-7 k.o. Furthermore, they presumably did not perform the measurements at 37°C. Ion transporters exhibit temperature-dependent behaviour, so performing experiments at physiological temperatures might be important. Using the DNA "nanodevice" Clensor, Chakraborty et al. studied $[\mathrm{Cl}^-]_{lyso}$ in lysosomes of coelomocytes of *Caenorhabditis elegans* and compared values from WT and F42A8.3 k.d. or clh-6 k.d. animals, where F42A8.3 and clh-6 are the *C. elegans* homologues for ostm-1 and ClC-7 [39]. In both F42A8.3 k.d. and clh-6 k.d. animals they observed reduced $[\mathrm{Cl}^-]_{lyso}$ of ∼48 mM compared to ∼72 mM in WT animals. The pH was unaffected in all experiments [38, 39].

In this study, the effects of three lysosomal CLC transporters, ClC-7, ClC-6, and ClC-3b, as well as of two mutant ClC-7, E245A and Y746Q, on the lysosomal $[\mathrm{Cl}^-]$ and pH were examined. While the overexpression of ClC-6 in HEK293T cells left $[\mathrm{Cl}^-]_{lyso}$ and pH unaltered, the overexpression of ClC-7 and ClC-3b slightly (not significantly) decreased $[\mathrm{Cl}^-]_{lyso}$ and significantly increased the lysosomal pH (figure 3.11). The alkalinization upon ClC-7/3b overexpression is consistent with the hypothesis by Jentsch et al., but if the CLCs transported protons out of the lumen, an increase of $[\mathrm{Cl}^-]_{lyso}$ would be expected. However, a significant increase of $[\mathrm{Cl}^-]_{lyso}$ to 173 ± 34 mM was observed upon shRNA-mediated reduction of ClC-7 expression in HEK293T cells, suggesting that ClC-7 transports Cl^- out of the lysosome.

Simulations using the model provided by Ishida et al. [4] could reproduce these experimental findings. With increasing numbers of CLCs the simulated $[\mathrm{Cl}^-]_{lyso}$ decreases, but at very high numbers of CLCs, a further increase of CLC-expression only slightly decreases $[\mathrm{Cl}^-]_{lyso}$ (figure 3.14 A, red squares) which might be the reason why only the knock-down but not the overexpression of CLCs significantly changed the measured $[\mathrm{Cl}^-]_{lyso}$. The increase of the lysosomal pH with increasing numbers of CLCs could also be shown with the simulations (figure 3.14 B, red squares). The model furthermore predicts increasing $[\mathrm{Na}^+]_{lyso}$ and especially $[\mathrm{K}^+]_{lyso}$ upon overexpression of CLCs (figure 3.14 C and D, red squares), which might lead to an efflux of protons and therefore explain the increase of the pH.

It has been shown that lower lysosomal $[\mathrm{Cl}^-]_{lyso}$ lead to a reduced Ca^{2+}-release from the lysosome [39], which is required for fusion of lysosomes with other compartments [30]. Hence, lower $[\mathrm{Cl}^-]_{lyso}$ are expected to impair autophagosome-lysosome fusion, and results from this work support this assumption and furthermore indicate that an increase of $[\mathrm{Cl}^-]_{lyso}$ to values higher than physiological concentrations does not impair or enhance fusion (figure 3.20). The knock-down of ClC-7 in HEK293T cells did not affect autophagosome-lysosome fusion. If the knock-down had led to a decrease of $[\mathrm{Cl}^-]_{lyso}$, as was the case in *Caenorhabditis elegans* [39], less fusion of lysosomes with autophagosomes would have been expected. As a control, in cells transfected with ClC-7

E245A or VGLUT$_{lyso}$, which showed significantly reduced $[Cl^-]_{lyso}$, the fusion indeed was impaired. Hence, the higher $[Cl^-]_{lyso}$ in ClC-7 k.d. cells measured in this work are in line with the results from the autophagosome-lysosome fusion experiments.

Since Cl^- outward transport via lysosomal CLCs would be coupled to H^+ uptake, one would expect a less acidic pH at reduced ClC-7 expression levels, which was not observed (figure 3.13 B). The reduced ClC-7-mediated lysosomal acidification might be compensated by increased activity of the v-ATPases due to the higher $[Cl^-]_{lyso}$. Therefore, the effect of ClC-7 knock-down was studied in the presence of 200 nM bafilomycin A1. Under these conditions, a lysosomal pH of 6.90 ± 0.65 was measured, which is significantly higher than the lysosomal pH in untransfected cells treated with bafilomycin A1 (figure 3.13 C). This observation suggests that ClC-7 mediates proton uptake into the lysosomes, driven by the outward transport of Cl^-. This function of ClC-7 also explains why lysosomes of untransfected cells do not exhibit a neutral pH after blocking the V-ATPase with bafilomycin A1, but are still slightly acidic (pH 6.29 ± 0.75, figure 3.8 A). Even though the v-ATPase is blocked, protons might still be transported into the lumen by ClC-7.

Weinert et al. generated genetically modified animals expressing a mutant transporter, E245A ClC-7, that converts ClC-7 into an uncoupled Cl^-–conductor [38]. Compared to WT, they observed reduced $[Cl^-]_{lyso}$, but again, to measure this, they used MEQ conjugated to dextran and had to perform their measurements in ES with low $[Cl^-]$ of 7 mM, due to the low sensitivity of MEQ-dextran, which might have unknown effects on ClC-7. However, as shown in figure 3.12 A, in HEK293T cells transfected with the same mutation, SPQ-measurements also revealed a reduction of $[Cl^-]_{lyso}$ (to 123 ± 6 mM) compared to untransfected cells. Weinert et al. suggest that the WT ClC-7 exploits the proton-gradient across the lysosomal membrane to accumulate Cl^- in the lumen, while transporting protons out of the lysosome, along their gradient. This would, of course, not be possible with an uncoupled Cl^-–conductor. However, with this explanation, one would expect a decrease of the lysosomal pH, since no protons are transported out of the lysosome by ClC-7 E245A. Contrary to this expectation, a significant increase of the lysosomal pH to 5.25 ± 0.64 was measured in HEK293T cells upon transfection with the ClC-7 E245A mutant (figure 3.12 B). This finding, again, is in line with WT ClC-7 transporting protons into and chloride out of the lysosome, and not vice versa.

The question, why $[Cl^-]_{lyso}$ in HEK293T cells with ClC-7 E245A is lower than in untransfected cells, might be answered as follows: To transport chloride out of the lysosome, WT ClC-7 has to transport protons into the lumen against the proton-gradient across the lysosomal membrane, which might be important to facilitate a controlled and slow chloride efflux. The E245A mutation is uncoupling the chloride efflux from the proton transport, so chloride can more easily leave the lysosome via ClC-7 E245A, which leads to the measured reduced $[\mathrm{Cl}^-]_{lyso}$.

Taken together, our experiments support the notion that CLC chloride-proton exchangers mediate chloride transport out of the lysosome, driving proton inward movement. Results from patch-clamp recordings are in line with this. Electrophysiological experiments with ClC-7 expressed in the plasma membrane showed that ClC-7 is a strong outward rectifier, indicating a primary direction of Cl^- flow through ClC-7 out of the lysosome and proton flow into the lysosome [4, 41]. In a study by Cang et al., they performed whole-endolysosome patch clamp recordings and observed Cl^--currents in endolysosomes of macrophages and cardiac myocytes. These currents were abolished when they removed Cl^- from the pipette (lumen), which means that the underlying conductance allows unidirectional Cl^- movement from the lumen into the cytosol [3].

The results from this study seem to indicate that CLCs do not transport chloride into the lysosome, which raises the question, which channel or transporter is responsible for the Cl^- accumulation. The decrease of $[\mathrm{Cl}^-]_{lyso}$ observed upon ClC-7 E245A or $\mathrm{VGLUT1}_{lyso}$ expression (chapters 3.7.2 and 3.9) suggests that Cl^- accumulation cannot be mediated via a simple channel. The reduced $[\mathrm{Cl}^-]_{lyso}$ after blocking the V-ATPases as well as the enhanced accumulation of Cl^- upon lysosomal K^+-channel blockade demonstrate that an electrogenic, pH-dependent transport process is necessary, which in turn excludes electroneutral or pH independent transporters as molecular basis of Cl^- accumulation.

In this study I tested the effect of overexpression and/or knock-down of three potential candidates with possible lysosomal localization on lysosomal $[\mathrm{Cl}^-]$ and pH.

SLC26A11 is a member of the SLC26 family of multifunctional anion exchangers and targets to lysosomes upon heterologous expression in HEK293T cells (figure 3.15 C). In *Xenopus* oocytes, SLC26A11 expression results in the occurrence of a time- and voltage-dependent anion current [106], and cerebellum-specific knock-out of SLC26A11 reduces the cytosolic $[\mathrm{Cl}^-]$ of Purkinje neurons [108], indicating that SLC26A11 functions as anion channel or uniporter. However, the overexpression of SLC26A11 in HEK293T cells did not significantly change $[\mathrm{Cl}^-]_{lyso}$, but it increased the lysosomal pH to 5.10 ± 0.79 (figure 3.15 A and B), indicating that SLC26A11 might exhibit a proton conductance or modify H^+-ATPase activity. The ability of SLC26A11 to carry cations and to regulate acid translocation via the H^+-ATPase has been suggested before [106].

Sialin (SLC17A5) is a H^+/sialic acid cotransporter, that transports protons and free sialic acid out of the lysosome [110, 111, 112]. In addition, sialin is able to import aspartate and glutamate into acidic organelles [113]. Overexpression as well as knock down in HEK293T cells leaves [Cl$^-$] in lysosomes unaffected, while the lysosomal pH increases upon overexpression (figures 3.16 A and B).

Lastly, possible effects of the proton-activated chloride channel TMEM206 [116, 117] were tested, but no effects on lysosomal [Cl$^-$] or pH were observed (figures 3.17 A and B).

There are certainly proteins in the lysosomal membrane which have not yet been entirely understood and might play a role in luminal chloride accumulation [140]. There might also still be chloride transporters which have not even been discovered yet. The lysosome model by Ishida et al. [4] failed to reproduce many experimental findings, e.g. the increased pH in ClC-7 k.d. cells (in presence of bafilomycin A1, figure 3.14, blue circles) or the results with the E245A mutant of ClC-7 (table 3.3), indicating that there are transport processes in the lysosome which have not been considered in this model. The results from this work might have put us one step closer to understanding the chloride transport mechanisms in the lysosome, but to get the whole picture still more work needs to be done.

4.5 Cl$^-$-Driven Acidification Through CLCs Requires Lumen Negative Membrane Potential

ClC-7 has been shown to be capable of carrying Cl$^-$ both into and out of lysosomes isolated from native tissue [100]. The electrogenicity of the transport makes the lysosomal membrane potential a key determinant of the transport direction, i.e. whether the CLCs mediate chloride-driven acidification or proton-driven Cl$^-$ accumulation [41].

With the cytosolic and luminal concentrations of Cl$^-$ and H$^+$ measured under physiological conditions in chapter 3.4, the reversal potential of ClC-7 can be calculated using the Nernst-equation.

The electrochemical potential ΔG is the sum of the chemical and the electrical driving forces:

$$\Delta G = RTln\frac{c_1}{c_2} + zF\Delta U. \tag{4.1}$$

R is the universal gas constant, T the temperature, c_1 and c_2 are the ion concentrations, z is the charge of the ion, F is the Faraday constant, and ΔU the voltage across the membrane. In case of substrate exchange, the forces have to be subtracted. Accordingly, for the CLCs in the lysosomal membrane, which all have a 2Cl$^-$:1H$^+$ stoichiometry [34], the following equation applies:

$$\Delta G = RTln\frac{[H^+_{lyso}]}{[H^+_{cyto}]} + F\Delta U - 2\left(RTln\frac{[Cl^-_{lyso}]}{[Cl^-_{cyto}]} - F\Delta U\right). \tag{4.2}$$

Under equilibrium conditions at the reversal potential, ΔG equals 0. After some mathematical transformations and simplifications, the reversal potential is described by the following equation:

$$\Delta U = \frac{RT}{3F}ln\left(\left(\frac{[Cl^-_{lyso}]}{[Cl^-_{cyto}]}\right)^2\frac{[H^+_{cyto}]}{[H^+_{lyso}]}\right). \tag{4.3}$$

Insertion of the concentrations measured in chapter 3.4 yields a reversal potential of the CLCs of -38 mV (lumen negative). At lower membrane potentials than this, the CLCs transport protons into the lumen and chloride out. Supplemental figure A.3 shows that higher lysosomal [Cl$^-$] and pH would lead to more positive reversal potentials, whereas higher cytosolic [Cl$^-$] and pH would shift it to more negative values.

The membrane potential of the lysosome is a matter of ongoing debate. In a study from 1983, Ohkuma et al. measured a lumen positive membrane potential using a cyanine dye in purified lysosomes from the liver of rats [141]. In 2011, Kiovusalo et al. also reported a lumen positive membrane potential of 28.5 mV, which they obtained in the lysosomes of RAW264.7 cells via FRET [142]. In contrast to that, in 2013, Ishida et al. simulated membrane potentials between -10 and +10 mV [4]. Cang et al. measured lumen negative membrane potentials via lysosomal patch-clamp recordings of lysosomes of RAW264.7 and glial cells in 2015 [98] and with the same technique, in 2017, Wang et al. obtained lumen negative membrane potentials of -15 to -30 mV [143]. Hence, the reported lysosomal membrane potentials are quite scattered.

However, the reversal potential calculated above, together with the hypothesis discussed in the previous chapter, that ClC-7 transports chloride out of and protons into the lysosome, predicts a lysosomal membrane potential lower than -38 mV (lumen negative) in HEK293T cells. This is more negative than the hitherto reported lysosomal membrane potentials.

To further understand this result, in future experiments we plan to modify [Na$^+$] and [K$^+$], e.g. by blocking the Na$^+$/K$^+$-ATPase, since these concentrations probably have a great impact on the membrane potential. We plan to measure the resulting change in [Na$^+$] and [K$^+$] and its impact on lysosomal [Cl$^-$] and pH.

4.6 Lysosomal Expression of VGLUT1 Provides Insight Into its Transport Mechanisms

Vesicular glutamate transporters (VGLUTs) belong to the SLC17 family of organic anion transporters. They are not endogeneously present in the lysosomal membrane but in the membrane of synaptic vesicles (SV), where they transport glutamate, the major excitatory transmitter in the vertebrate nervous system, from the cytosol into the lumen of the synaptic vesicle [115, 119]. The glutamate transport depends on an electrochemical proton gradient driven by the v-ATPase and requires chloride ions, but the exact transport mechanisms of VGLUTs are not entirely understood [119].

In this work, a mutant VGLUT1 was targeted to the lysosomal membrane of HEK293T cells (chapter 3.9). Although this maneuver created an artificial situation that will not occur in any native cell, experiments with VGLUT provided novel insights into electrical properties of lysosomes.

It has been shown that VGLUT exhibits a chloride conductance which supports glutamate uptake [114]. Heterologous expression of VGLUT1_{lyso} in the lysosome decreases the lysosomal $[\text{Cl}^-]_{lyso}$ to 63.8 ± 13.7 mM (figure 3.18 B). With 67.8 ± 9.6 mM the cytosolic $[\text{Cl}^-]_{cyto}$ is not significantly different from $[\text{Cl}^-]_{lyso}$ in HEK293T cells expressing VGLUT1_{lyso} (figure 3.18 A). Martineau et al. [115] reported that the glutamate uptake can be fuelled by the chloride gradient in SV, and that the transport process continues until this gradient is vanished. Shortly after endocytosis, the $[\text{Cl}^-]$ in the lumen of the SV is higher than in the cytosol. At resting state, Martineau et al. measured similar $[\text{Cl}^-]$ in the SV and the cytosol of cultured hippocampal neurons of mice, and they observed much higher resting $[\text{Cl}^-]$ in SV of VGLUT1-deficient mice than in WT, since here, no chloride can leave the SV lumen via VGLUT1.

Interestingly, the $[\text{Cl}^-]_{cyto}$ in HEK293T cells expressing VGLUT1_{lyso} is significantly higher than in untransfected cells. The efflux of chloride from the lumen into the cytosol might lead to this increase of $[\text{Cl}^-]_{cyto}$. This finding demonstrates that lysosomal chloride transporters/channels can contribute to setting the cytoplasmic chloride concentration.

Martineau et al. proposed that VGLUT1 is a glutamate/H^+ exchanger associated with a stoichiometrically uncoupled Cl^- conductance [115]. If the accumulation of glutamate in the lysosomal lumen is accompanied by an export of protons out of the lumen along their chemical gradient, an increase of the lysosomal pH in cells expressing VGLUT1_{lyso} is expected. Indeed, the pH increases to 5.29 ± 0.68 upon expression of VGLUT1_{lyso} in the lysosomal membrane (figure 3.18 C), and the observed chloride efflux might compensate the change in the membrane potential caused by the charge transfer.

Moreover, since most of the lysosomal chloride seems to exit the lysosomes via VGLUT1$_{lyso}$, the chloride efflux through ClC-7 presumably decreases or even stops and with it the proton influx via ClC-7, further increasing the luminal pH. Assuming that the expression of VGLUT1$_{lyso}$ leads to a passive distribution of chloride along its electrochemical gradient, the lysosomal membrane potential U can be calculated from the Nernst equation:

$$U = \frac{RT}{zF} ln \frac{[Cl^{-}]_{cyto}}{[Cl^{-}]_{lyso}} \tag{4.4}$$

where R is the universal gas constant, T the temperature, z is the charge of the ion (-1 for chloride), and F the Faraday constant. Insertion of the $[\mathrm{Cl}^-]_{cyto}$ and $[\mathrm{Cl}^-]_{lyso}$ measured in the presence of VGLUT1$_{lyso}$ reveals a slightly lumen-negative membrane potential of -1.6 mV. Hence, under these conditions, the CLCs might even actively contribute to the alkalinization, considering their reversal potential of almost -40 mV (lumen negative, see chapter 4.5).

Nevertheless, with 5.29 the pH is still acidic, probably because at some point, when the chloride gradient is vanished, the effect of the v-ATPase activity exceeds the VGLUT1$_{lyso}$ activity, so more protons are pumped into the lumen by the v-ATPase than are transported out of the lumen via VGLUT1 [115] (and CLCs).

Taken together, the results support the model of VGLUT1 being a glutamate/H^+-exchanger associated with a stoichiometrically uncoupled Cl^- conductance. If the lysosomal membrane endogeneously expressed transporters with a transport mechanism similar to that of VGLUT1, the physiological $[\mathrm{Cl}^-]_{lyso}$ would not be able to reach values as high as 150 mM. Like VGLUT1, Sialin is a member of the SLC17 family of organic anion transporters. Sialin is endogeneously expressed in the lysosomal membrane and mediates H^+-aspartate/glutamate exchange, but, in contrast to VGLUT1, it does not exhibit an associated anion conductance [114]. Accordingly, sialin expression in HEK293T cells does not affect lysosomal $[\mathrm{Cl}^-]$ and only slightly increases the lysosomal pH to 4.85 ± 0.49 (figures 3.16 A and B).

In future experiments, we plan to examine whether the experimental findings would also occur without a H^+-coupled glutamate transport of VGLUT1$_{lyso}$. In skeletal muscle, where the chloride conductance exceeds the potassium conductance several-fold, chloride is passively distributed, and changes in $[\mathrm{Cl}^-]$ leave the resting potential of the cells unaffected, because chloride fluxes across the membrane preserve the passive distribution given by the muscle´s membrane potential [144]. The expression of VGLUT1 in the lysosomal membrane induces a large pH-dependent chloride conductance. Like in skeletal muscle, this chloride conductance might mediate Cl^- efflux, until chloride is passively distributed. In agreement with this, blocking the lysosomal K^+ channel TMEM175 using 4-AP depolarizes the lysosomal membrane to +13.6 mV (equation 4.4 with $[Cl^-]_{lyso}$ shown in supplemental figure A.4, VGLUT expression + 4-AP), which increases the lysosomal $[Cl^-]$ in cells expressing $VGLUT1_{lyso}$ (supplemental figure A.4). The glutamate transport function might not be necessary for the observed chloride efflux. However, according to simulations, a simple increase of the chloride permeability cannot explain the experimental findings (figure 3.19), at least not to that extent. We therefore plan to experimentally test this by repeating the measurements with the mutant H120A, which abolishes the glutamate transport of VGLUT [145].

Chapter 5

Conclusion

This thesis demonstrated, for the first time, a method to measure lysosomal chloride concentrations via fluorescence lifetime imaging microscopy using the quinolinium-based dyes MEQ and SPQ. MEQ offers the possibility to simultaneously monitor the chloride concentration in the cytosol and enlarged lysosomes, while with SPQ the chloride concentration in normal-sized lysosomes can be measured. The lysosomal chloride concentrations obtained with the two sensors are quite similar and much higher than the measured cytosolic chloride concentration.

In combination with ratiometric pH measurements with oregon green 488- and tetramethylrhodamine-dextran, new insights into lysosomal ion regulation could be obtained. It was shown that the v-ATPase is the driving force for the chloride accumulation in the lysosome and that chloride plays a role in lysosomal acidification, especially if the efflux of potassium as a counterion is blocked.

Furthermore, it was demonstrated that an electrogenic, pH-dependent transport process is necessary for lysosomal chloride accumulation. However, various experimental results indicate that in HEK293T cells, CLC chloride-proton exchangers, such as ClC-7, do not transport chloride into the lysosome and protons out, like it had been suggested before, but vice versa. They mediate chloride transport out of the lysosome, driving proton inward movement against the chemical gradient, which could be a mechanism to facilitate a controlled and slow chloride efflux. Several other transporters and their role in lysosomal chloride accumulation were tested and could be ruled out.

In addition, heterologous expression of the vesicular glutamate transporter VGLUT1 in the lysosomal membrane could provide insights into its transport mechanism. Changes in the lysosomal and cytosolic chloride concentration and the lysosomal pH in transfected cells support a proposed glutamate/H^+ exchange associated with a stoichiometrically uncoupled Cl^- conductance of VGLUT1 [115].

Appendix A

Supplements

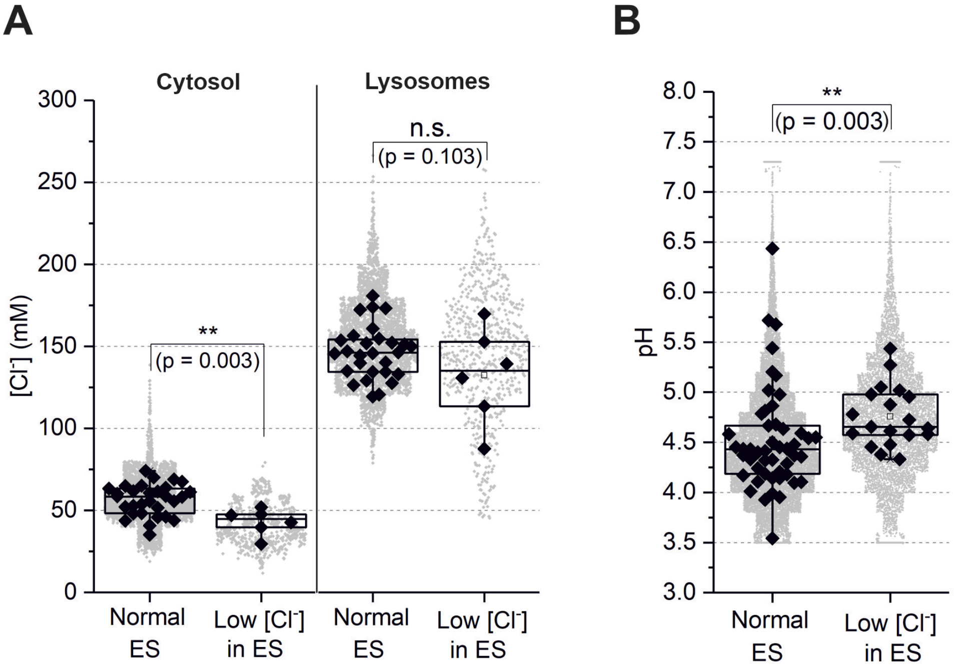

Figure A.1: **Results after incubation in ES with low [Cl$^-$].** (A) Cytosolic and lysosomal [Cl$^-$] measured with MEQ after incubation in extracellular solution (ES) with low [Cl$^-$] of 5.4 mM for at least 3h prior to measurements (also during loading of cells with diH-MEQ). (B) Lysosomal pH after incubation in ES with low [Cl$^-$] for 3h.

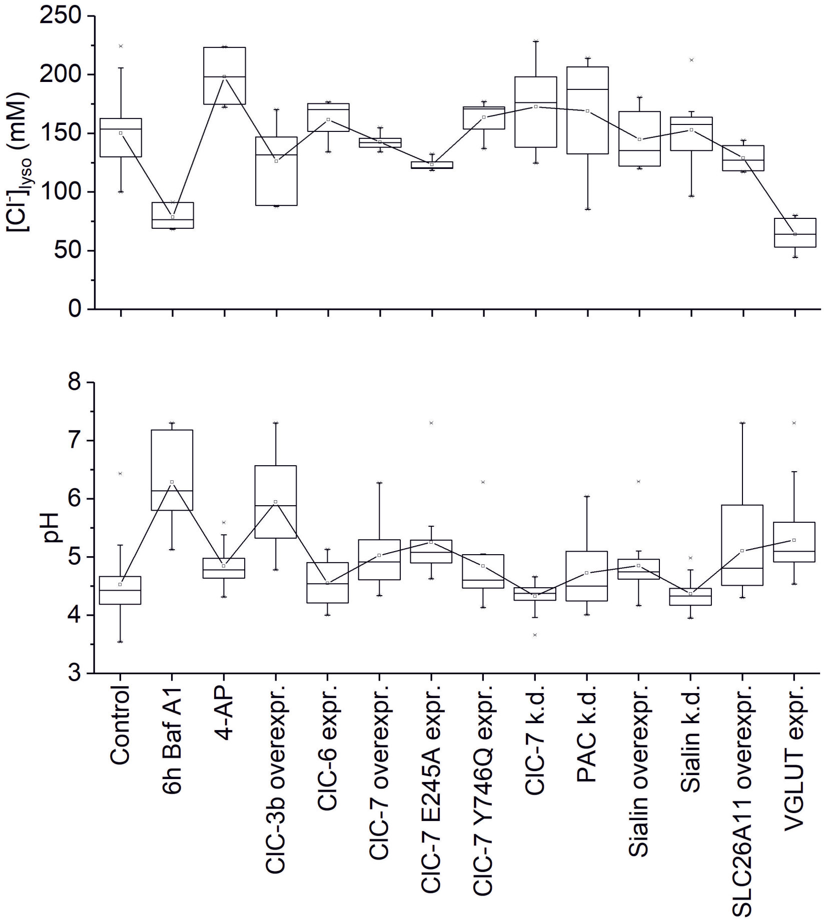

Figure A.2: **Correlation between lysosomal [Cl^-] and pH.** The results from this work under different conditions show a correlation between lysosomal pH and $[Cl^-]_{lyso}$. A higher $[Cl^-]_{lyso}$ is generally accompanied by a more acidic pH.

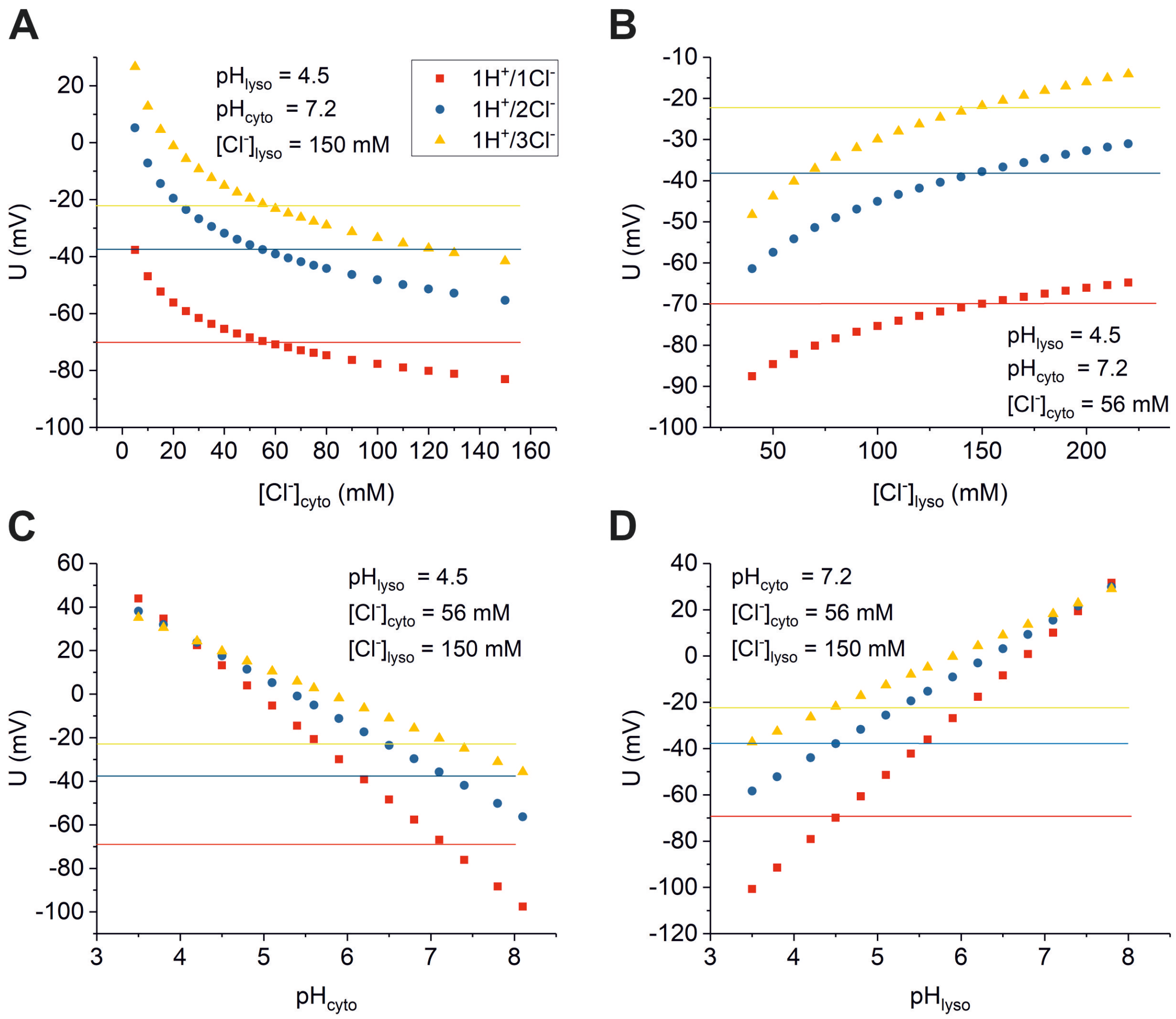

Figure A.3: **Reversal potential of lysosomal CLCs.** Reversal potential U of CLCs over $[\mathrm{Cl}^-]_{cyto}$, $[\mathrm{Cl}^-]_{lyso}$, pH_{cyto}, and pH_{lyso}, calculated according to equation 4.3. Higher lysosomal $[\mathrm{Cl}^-]$ and pH lead to more positive reversal potentials, whereas higher cytosolic $[\mathrm{Cl}^-]$ and pH shift it to more negative values. Changing the stoichiometry to $1\mathrm{H}^+{:}1\mathrm{Cl}^-$ (red squares) or $1\mathrm{H}^+{:}3\mathrm{Cl}^-$ (yellow triangles) leads to an overall shift of the reversal potential to more negative or more positive values, respectively, compared to $1\mathrm{H}^+{:}2\mathrm{Cl}^-$ (blue circles). The horizontal lines indicate the respective reversal potentials resulting from insertion of the measured concentrations (chapter 3.4) into equation 4.3.

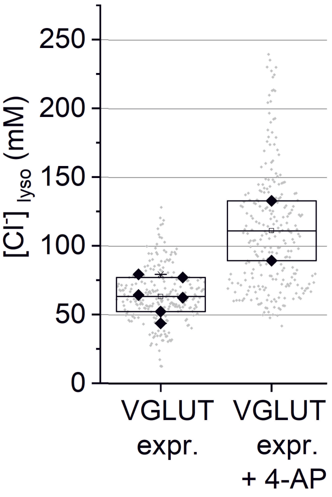

Figure A.4: **Influence of 4-AP in VGLUT-expressing lysosomes.** $[\mathrm{Cl}^-]_{lyso}$ cells expressing VGLUT1$_{lyso}$ without 4-AP ($[\mathrm{Cl}^-]_{lyso} = 63.8 \pm 13.7$ mM (SD)) and after 30 min incubation of cells in medium supplemented with 400 µM 4-AP ($[\mathrm{Cl}^-]_{lyso} = 113 \pm 32$ mM (SD), N=2 coverslips, >50 cells, 250 lysosomes).

Bibliography

[1] J. Biwersi and A. S. Verkman. Cell-permeable fluorescent indicator for cytosolic chloride. *Biochemistry*, 30(32):7879–7883, 1991.

[2] T. Hartmann and A.S. Verkman. Model of ion transport regulation in chloride-secreting airway epithelial cells. Integrated description of electrical, chemical, and fluorescence measurements. *Biophys. J.*, 58:391–401, 1990.

[3] C. Cang, B. Bekele, and D. Ren. The voltage-gated sodium channel TPC1 confers endolysosomal excitbility. *Nature Chemical Biology*, 10(6):463–469, 2014.

[4] Y. Ishida, S. Nayak, J. A. Mindell, and M. Grabe. A model of lysosomal ph regulation. *Journal of General Physiology*, 141(6):705–720, 2013.

[5] J. P. Luzio, M. D. Parkinson, S. R. Gray, and N.A. Bright. The delivery of endocytosed cargo to lysosomes. *Biochem Soc Trans.*, 37(5):2019–2021, 2009.

[6] N. Mizushima and M. Komatsu. Autophagy: renovation of cells and tissues. *Cell*, 147(4):728–741, 2011.

[7] C. F. Bento, M. Renna, G. Ghislat, C. Puri, A. Ashkenazi, M. Vicinanza, F. M. Menzies, and D. C. Rubinztein. Mammalian autophagy: How does it work? *Annu Rev Biochem.*, 85:685–713, 2016.

[8] J. Pu, C. M. Guardia, T. Keren-Kaplan, and J. S. Bonifacino. Mechanisms and functions of lysosome positioning. *J. Cell. Sci.*, 129:4329–4339, 2016.

[9] C. Settembre, A. Fraldi, D. L. Medina, and A. Ballabio. Signals from the lysosome: a control centre for cellular clearance and energy metabolism. *Nat Rev Mol Cell Biol.*, 14(5):283–296, 2013.

[10] A. Efeyan, W. C. Comb, and D. M. Sabatini. Nutrient-sensing mechanisms and pathways. *Nature*, 517:302–310, 2015.

[11] C. Cang, Y. Zhou, B. Navarro, Y. J. Seo, K. Aranda, L. Shi, S. Battaglia-Hsu, I. Nissim, D. E. Clapham, and D. Ren. mTOR regulates lysosomal ATP-sensitive two-pore Na(+) channels to adapt to metabolic state. *Cell*, 152(4):778–790, 2013.

[12] A. Ballabio and J. S. Bonifacino. Lysosomes as dynamic regulators of cell and organismal homeostasis. *Nature Reviews Molecular Cell Biology*, 21:101–118, 2020.

[13] H. Xu and D. Ren. Lysosomal physiology. *Annu Rev Physiol.*, 77:57–80, 2015.

[14] D. Bandyopadhyay, A. Cyphersmith, J. A. Zapata, Y. J. Kim, and C. K. Payne. Lysosome Transport as a Function of Lysosome Diameter. *PLOS ONE*, 9(1), 2014.

[15] M.-N. Cordonnier, D. Dauzonne, D. Louvard, and E. Coudrier. Actin Filaments and Myosin I Alpha Cooperate with Microtubules for the Movement of Lysosomes. *Mol. Biol. Cell*, 12(12):4013–4029, 2001.

[16] A. B. Mukherjee, A. P. Appu, T. Sadhukhan, S. Casey, A. Mondal, Z. Zhang, and M. B. Bagh. Emerging new roles of the lysosome and neuronal ceroid lipofuscinoses. *Mol Neurodegener*, 14(1), 2019.

[17] G. M. Cooper. The Cell: A Molecular Approach. 2nd edition. *Sunderland (MA): Sinauer Associates*, 2000.

[18] J. A. Mindell. Lysosomal acidification mechanisms. *Annual Review of Physiology*, 74:69–86, 2012.

[19] D. E. Johnson, P. Ostrowski, V. Jaumouille, and S. Grinstein. The position of lysosomes within the cell determines their luminal pH. *J. Cell Biol.*, 212(6):677–692, 2016.

[20] T. Nishi and M. Forgac. The vacuolar (H+)-ATPases–nature's most versatile proton pumps. *Nature Reviews Molecular Cell Biology*, 3(2):94–103, 2002.

[21] M. Forgac. Vacuolar atpases: rotary proton pumps in physiology and pathophysiology. *Nature Reviews Molecular Cell Biology*, 8:917–929, 2007.

[22] A. Sardini, J. S. Amey, K. H. Weylandt, M. Nobles, M. A. Valverde, and C. F. Higgins. Cell volume regulation and swelling-activated chloride channels. *Biochim Biophys Acta.*, 1618(2):153-162, 2003.

[23] V. Faundez and H. C. Hartzell. Intracellular chloride channels: determinants of function in the endosomal pathway. *Sci STKE*, 233, 2004.

[24] P. Bregestovski, T. Waseem, and M. Mukhtarov. Genetically encoded optical sensors for monitoring of intracellular chloride and chloride-selective channel activity. *Front Mol Neurosci.*, 2(15), 2009.

[25] A. G. Valdivieso, M. Clauzure, M. Massip-Copiz, and T. A. Santa-Coloma. The Chloride Anion Acts as a Second Messenger in Mammalian Cells - Modifying the Expression of Specific Genes. *Cell Physiol. Biochem.*, 38(1):49–64, 2016.

[26] M. Clauzure, A. G. Valdivieso, M. M. Massip-Copiz, C. Mori, A. V. Dugour, J. M. Figueroa, and T. A. Santa-Coloma. Intracellular chloride concentration changes modulate il-1β expression and secretion in human bronchial epithilial cultured cells. *Journal of Cellular Biochemistry*, 118(8):2131–2140, 2017.

[27] R. Planells-Cases and T. J. Jentsch. Chloride channelopathies. *Biochim Biophys Acta*, 1792(3):173–189, 2009.

[28] S. Saha, V. Prakash, S. Halder, K. Chakraborty, and Y. Krishnan. A ph-independent dna nanodevice for quantifying chloride transport in organelles of living cells. *Nature Nanotechnology*, 10:645–651, 2015.

[29] M. Saito, P. I. Hanson, and P. Schlesinger. Luminal chloride-dependent activation of endosome calcium channels: Patch clamp study of enlarged endosomes. *J. Biol. Chem.*, 282(37):27327–27333, 2007.

[30] J. P. Luzio, N. A. Bright, and P. R. Pryor. The role of calcium and other ions in sorting and delivery in the late endocytic pathway. *Biochemical Society Transactions*, 35(5):1088–1091, 2007.

[31] M. Hara-Chikuma, Y. Wang, S. E. Guggino, W. B. Guggino, and A. S. Verkman. Impaired acidification in early endosomes of clc-5 deficient proximal tubule. *Biochemical and Biophysical Research Communications*, 329(3):941–946, 2005.

[32] S. M. Stobrawa, T. Breiderhoff, S. Takamori, D. Engel, M. Schweizer, A. A. Zdebik, M. R. Bösl, K. Ruether, H. Jahn, A. Draguhn, R. Jahn, and T. J. Jentsch.

Disruption of clc-3, a chloride channel expressed on synaptic vesicles, leads to a loss of the hippocampus. *Cell Press*, 29(1):185–196, 2001.

[33] D. Kasper, R. Planells-Cases, J. C. Fuhrmann, O. Scheel, O. Zeitz, K. Ruether, A. Schmitt, M. Poet, R. Steinfeld, M. Schweizer, U. Kornak, and T. J. Jentsch. Loss of the chloride channel clc-7 leads to lysosomal storage disease and neurodegeneration. *EMBO J.*, 24(5):1079–1091, 2005.

[34] T. Stauber and T. J. Jentsch. Chloride in vesicular trafficking and function. *Annual Review of Physiology*, 75:453–477, 2013.

[35] R. E. Guzman, S. Bungert-Plümke, A. Franzen, and C. Fahlke. Preferential association with ClC-3 permits sorting of ClC-4 into endosomal compartments. *J. Biol. Chem.*, 292(46):19055–19065, 2017.

[36] M. Pöet, U. Kornak, M. Schweizer, A. A. Zdebik, O. Scheel, S. Hoelter, W. Wurst, A. Schmitt, J. C. Fuhrmann, R. Planells-Cases, S. E. Mole, C. A. Hübner, and T. J. Jentsch. Lysosomal storage disease upon disruption of the neuronal chloride transport protein clc-6. *Proc Natl Acad Sci U S A*, 103(37):13854–13859, 2006.

[37] U. Kornak, D. Kasper, M. R. Bosl, E. Kaiser, M. Schweizer, A. Schulz, W. Friedrich, G. Delling, and T. J. Jentsch. Loss of the ClC-7 chloride channel leads to osteopetrosis in mice and man. *Cell*, 104(2):201–215, 2001.

[38] S. Weinert, S. Jabs, C. Supanchart, M. Schweizer, N. Gimber, M. Richter, J. Rademann, T. Stauber, U. Kornak, and T. J. Jentsch. Lysosomal pathology and osteopetrosis upon loss of H^+-driven lysosomal Cl^- accumulation. *Science*, 328(5984):1401–1403, 2010.

[39] K. Chakraborty, K. Leung, and Y. Krishnan. Hight lumenal chloride in the lysosome is critical for lysosome function. *Elife*, 2017.

[40] J. Rohrbough, H.-N. Nguyen, and F. S. Lamb. Modulation of ClC-3 gating and proton/anion exchange by internal and external protons and the anion selectivity filter. *J Physiol*, 596(17):4091–4119, 2018.

[41] L. Leisle, C. F. Ludwig, F. A. Wagner, T. J. Jentsch, and T. Stauber. Clc-7 is a slowly voltage-gated 2Cl/1H+-exchanger and requires ostm1 for transport activity. *EMBO J.*, 30:2140–2152, 2011.

[42] F. M. Platt, A. d'Azzo, B. L. Davidson, E. F. Neufeld, and C. J. Tifft. Lysosomal storage diseases. *Nat Rev Dis Primers*, 4(1):27, 2018.

[43] F. M. Platt, B. Boland, and A. C. van der Spoel. The cell biology of disease: lysosomal storage disorders: the cellular impact of lysosomal dysfunction. *J. Cell Biol.*, 199(5):723–734, 2012.

[44] A. Barrallo-Gimeno, A. Gradogna, I. Zanardi, M. Pusch, and R. Estevez. Regulatory–auxiliary subunits of clc chloride channel–transport proteins. *J Physiol.*, 593(18):4111–4127, 2015.

[45] P. F. Lange, L. Wartosch, T. J. Jentsch, and J. C. Fuhrmann. Clc-7 requires ostm1 as a beta-subunit to support bone resorption and lysosomal function. *Nature*, 440(7081):220–223, 2006.

[46] S. E. Mole and R. E. Williams. Neuronal ceroid-lipofuscinoses. *GeneReviews*, 2001.

[47] A. Sartelet, T. Stauber, W. Coppieters, C. F. Ludwig, C. Fasquelle, T. Druet, Z. Zhang, N. Ahariz, N. Cambisano, T. J. Jentsch, and C. Charlier. A missense mutation accelerating the gating of the lysosomal Cl/H+-exchanger ClC-7/Ostm1 causes osteopetrosis with gingival hamartomas in cattle. *Dis Model Mech.*, 7(1):119–128, 2014.

[48] A. R. A. Marques and P. Saftig. Lysosomal storage disorders - challenges, concepts and avenues for therapy: beyond rare diseases. *J. Cell Sci.*, 132(2), 2019.

[49] C. Wang, M. A. Telpoukhovskaia, B.A. Bahr, X. Chen, and L. Gan. Endo-lysosomal dysfunction: a converging mechanism in neurodegenerative diseases. *Curr Opin Neurobiol*, 48:52–58, 2018.

[50] J.-H. Lee, W. Haung Yu, A. Kumar, S. Lee, P. S. Mohan, C. M. Peterhoff, D. M. Wolfe, M. Martinez-Vicente, A. C. Massey, G. Sovak, Y. Uchiyama, D. Westaway, S. S. Sisodia, A. M. Cuervo, and R. A. Nixon. Lysosomal proteolysis and autophagy require presenilin 1 and are disrupted by alzheimer-related ps1 mutations. *Cell*, 141(7):1146–1158, 2010.

[51] O. Markova, M. Mukhtarov, E. Real, Y. Jacob, and P. Bregestovski. Genetically encoded chloride indicator with improved sensitivity. *Journal of Neuroscience Methods*, 170(1):67–76, 2008.

[52] T. Kuner and G. J. Augustine. A genetically encoded ratiometric indicator for chloride: Capturing chloride transients in cultured hippocampal neurons. *Neuron*, 27(3):447–459, 2000.

[53] A. S. Verkman. Physiology and Pathology of Chloride Transporters and Channels in the Nervous System, Part 2: Current Methods for Studying Chloride Regulation, Chap. 6. *Chemical and Gfp-Based Fluorescent Chloride Indicators*, pages 111–123, 2009.

[54] N. P. Illsley and A. S. Verkman. Membrane chloride transport measured using a chloride-sensitive fluorescent probe. *Biochemistry*, 26(5):1215–1219, 1987.

[55] C. D. Geddes. Optical halide sensing using fluorescence quenching: theory, simulations and applications - a review. *Meas. Sci. Technol.*, 12:R53–R88, 2001.

[56] C. Biskup and T. Gensch. Fluorescence lifetime imaging of ions in biological tissues. *"Fluorescence Lifetime Spectroscopy and Imaging. Principles and Applications in Biomedical Diagnostics" D. Elson, P.W.M. French and L. Marcu, eds. Taylor Francis*, 2014.

[57] J. Meyer, V. Untiet, C. Fahlke, T. Gensch, and C. R. Rose. Quantitative determination of cellular [Na+] by fluorescence lifetime imaging with CoroNaGreen. *J Gen Physiol.*, 151(11):1319–1331, 2019.

[58] T. Gensch, V. Untiet, A. Franzen, P. Kovermann, and C. Fahlke. Determination of Intracellular Chloride Concentrations by Fluorescence Lifetime Imaging. *Advanced Time-Correlated Single Photon Counting Applications, Springer International Publishing*, 2015.

[59] W. Becker. Advanced time-correlated single photon counting techniques. Number 81 in Springer Series in Chemical Physics. Springer, Berlin, Heidelberg, 2005 edition, 2005.

[60] S. Jayaraman and A. S. Verkman. Quenching mechanism of quinolinium-type chloride-sensitive fluorescent indicators. *Biophysical Chemistry*, 85(1):49–57, 2000.

[61] A. S. Verkman. Development and biological applications of chloride-sensitive fluorescent indicators. *Am. J. Physiol.*, 259(3):C375–88, 1990.

[62] J. Schindelin, I. Arganda-Carreras, E. Frise, V. Kaynig, M. Longair, T. Pietzsch, S. Preibisch, C. Rueden, S. Saalfeld, B. Schmid, J.-Y. Tinevez, D. J. White,

V. Hartenstein, K. Eliceiri, P. Tomancak, and A. Cardona. Fiji: An open-source platform for biological-image analysis. *Nature Methods*, 9(7):676–682, 2012.

[63] S. Bolte and F. P. Cordelieres. A guided tour into subcellular colocalization analysis in light microscopy. *Journal of microscopy*, 224(3):213–232, 2006.

[64] F. L. Graham and A. J. van der Eb. A new technique for the assay of infectivity of human adenovirus 5 DNA. *Virology*, 52(2):456–467, 1973.

[65] O. Boussif, F. Lezoualch, M.A. Zanta, M.D. Mergny, D. Scherman, B. Demeneix, and J.P. Behr. A versatile vector for gene and oligonucleotide transfer into cells in culture and in vivo: Polyethylenimine. *Proceedings of the National Academy of Sciences of the United States of America*, 92(16):7297–7301, 1995.

[66] P.A. Longo, J. M. Kavran, M.-S. Kim, and D.J. Leahy. Transient mammalian cell transfection with polyethylenimine (pei). 529:227–240, 2013.

[67] A.-M. Ellegaard, M. Jäättelä, and J. Nylandsted. Visualizing lysosomal membrane permeabilizationby fluorescent dextran release. *Cold Spring Harb. Protoc.*, 2015(10):900–903, 2015.

[68] C. C. Chen, E. S. Butz, Y. K. Chao, Y. Grishchuk, L. Becker, S. Heller, S. A. Slaugenhaupt, M. Biel, C. Wahl-Schott, and C. Grimm. Small molecules for early endosome-specific patch clamping. *Cell Chem. Biol.*, 24(7):907–916, 2017.

[69] H. B. Jefferies, F. T. Cooke, P. Jat, C. Boucheron, T. Koizumi, M. Hayakawa, H. Kaizawa, T. Oshishi, P. Workman, M. D. Waterfield, and P. J. Parker. A selective PIKfyve inhibitor blocks PtdIns(3,5)P(2) production and disrupts endomembrane transport and retroviral budding. *EMBO Rep.*, 9(2):164–170, 2008.

[70] M.E.G. de Araujo, G. Liebscher, M.W. Hess, and L.A. Huber. Lysosomal size matters. *Traffic*, 21:60–75, 2020.

[71] A.-S. Nicot, H. Fares, B. Payrastre, A. D. Chisholm, M. Labouesse, and J. Laporte. The phosphoinositide kinase PIKfyve/Fab1p regulates terminal lysosome maturation in caenorhabditis elegans. *Molecular Biology of the Cell*, 17:3062–3074, 2006.

[72] T. Gensch (IBI-1, Forschungszentrum Jülich, Germany) and E. Polverini (Department of Physics, University of Parma, Italy). Quenching of MQAE-Fluorescence

by Chloride in Water studied by Molecular Dynamics Simulations. unpublished, 2006-2007.

[73] A. Sillen and Y. Engelborghs. The correct use of “average” fluorescence parameters. *Photochemistry and Photobiology*, 67:475–486, 1998.

[74] S. Rahmati. Accuracy of TCSPC-based Fluorescence Lifetime Data and its Dependence on Number of Detected Photons. *Masterarbeit University of Siegen/Forschungszentrum Jülich*, 2018.

[75] R. Krapf, C. A. Berry, and A. S. Verkman. Estimation of intracellular chloride activity in isolated perfused rabbit proximal convoluted tubules using a fluorescent indicator. *Biophys. J.*, 53:955–962, 1988.

[76] N. Marandi, A. Konnerth, and O. Garaschuk. Two-photon chloride imaging in neurons of brain slices. *Pflugers Arch*, 445:357–365, 2002.

[77] W. G. Telford, D. M. Shcherbakova, D. Buschke, T. S. Hawley, and V. V. Verkhusha. Multiparametric Flow Cytometry Using Near-Infrared Fluorescent Proteins Engineered from Bacterial Phytochromes. *PLOS ONE*, 10(3), 2015.

[78] J. A. Thomas, R. N. Buchsbaum, A. Zimniak, and E. Racker. Intracellular ph measurements in ehrlich ascites tumor cells utilizing spectroscopic probes generated in situ. *Biochemistry*, 18(11):2210–2218, 1979.

[79] J. Canton and S. Grinstein. Measuring lysosomal pH by fluorescence microscopy. *Lysosomes and Lysosomal Diseases*, pages 85–99, 2015.

[80] M. Mukhtarov, L. Liguori, T. Waseem, F. Rocca, S. Buldakova, D. Arosio, and P. Bregestovski. Calibration and functional analysis of three genetically encoded cl/ph sensors. *Frontiers in Molecular Neuroscience*, 6, 2013.

[81] S. Kimura, T. Noda, and T. Yoshimori. Dissection of the Autophagosome Maturation Process by a Novel Reporter Protein, Tandem Fluorescent-Tagged LC3. *Autophagy*, 3(5):452–460, 2007.

[82] M. A. El-Brolosy and Y. R. Stainier. Genetic compensation: A phenomenon in search of mechanisms. *PLOS*, 13(7), 2017.

[83] C. B. Moore, E. H. Guthrie, M. Tze-Han Huang, and D. J. Taxman. Short Hairpin RNA (shRNA): Design, Delivery, and Assessment of Gene Knockdown. *Methods Mol. Biol.*, 629:141–158, 2010.

[84] S. Milstein, M. Nguyen, R. Meyers, and A. de Fougerolles. Measuring RNAi Knockdown using qPCR. Laboratory Methods in Enzymology: Cell, Lipid and Carbohydrate. *Methods in Enzymology*, 533:57–77, 2013.

[85] X.-T. Cheng, Y.-X. Xie, B. Zhou, N. Huang, T. Farfel-Becker, and Z.-H. Sheng. Characterization of LAMP1-labeled nondegradative lysosomal and endocytic compartments in neurons. *Journal of Cell Biology*, 217(9):3127–3139, 2018.

[86] H. Kaneko, I. Putzier, U. B. Kaupp, and T. Gensch. Chloride accumulation in mammalian olfactory sensory neurons. *The Journal of Neuroscience*, 24(36):7931–7938, 2004.

[87] N. D. Sonawane, J. R. Thiagarajah, and A. S. Verkman. Chloride concentration in endosomes measured using a ratioable fluorescent cl- indicator. *The Journal of Biological Chemistry*, 277(7):5506–5513, 2002.

[88] D. Gilbert, C. Franjic-Wuertz, K. Funk, T. Gensch, S. Frings, and F. Moehrlen. Differential maturation of chloride homeostasis in primary afferent neurons of the somatosensory system. *Int. J. Dev. Neurosci.*, 25:479–489, 2007.

[89] C. Hille, M. Lahn, G.-H. Loehmannsroeben, and C. Dosche. Two-photon fluorescence lifetime imaging of intracellular chloride in cockroach salivary glands. *Photochem. Photobiol. Sci.*, 8:319–327, 2009.

[90] S. Ohkuma and B. Poole. Fluorescence probe measurement of the intralysosomal ph in living cells and the perturbation of ph by various agents. *Cell Biology*, 75(7):3327–3331, 1978.

[91] B. E. Steinberg, K. K. Huynh, A. Brodovitch, S. Jabs, T. Stauber, T. J. Jentsch, and S. Grinstein. A cation counterflux supports lysosomal acidification. *The Journal of Cell Biology*, 189(7):1171–1186, 2010.

[92] G. M. Lenk, Y. N. Park, R. Lemons, E. Flynn, M. Plank, C. M. Frei, M. J. Davis, B. Gregorka, J. A. Swanson, M. H. Meisler, and J. O. Kitzman. CRISPR knockout screen implicates three genes in lysosome function. *Scientific Reports*, 9(9609), 2019.

[93] N. D. Sonawane and A. S. Verkman. Determinants of [Cl] in recycling and late endosomes and Golgi complex measured using fluorescent ligands. *Journal of Cell Biology*, 160(7):1129–1138, 2003.

[94] M. Hara-Chikuma, B. Yang, N. D. Sonawane, S. Sasaki, S. Uchida, and A. S. Verkman. Clc-3 chloride channels facilitate endosomal acidification and chloride accumulation. *The Journal of Biological Chemistry*, 280(2):1241–1247, 2005.

[95] B. R. Rost, F. Schneider, M. K. Grauel, C. Wozny, C. G. Bentz, A. Blessing, T. Rosenmund, T. J. Jentsch, D. Schmitz, P. Hegemann, and C. Rosenmund. Optogenetic acidification of synaptic vesicles and lysosomes. *Nature Neuroscience*, 18(12):1845–1852, 2015.

[96] Y. Moriyama. Potassium ion dependent proton efflux and depolarization from spleen lysosomes. *Biochem. Biophys. Res. Commun.*, 156(1), 1988.

[97] R. W. Van Dyke. Acidification of rat liver lysosomes: quantitation and comparison with endosomes. *Am. J. Physiol*, 265(4 Pt 1), 1993.

[98] C. Cang, K. Aranda, Y. J. Seo, B. Gasnier, and D. Ren. TMEM175 Is an Organelle K(+) Channel Regulating Lysosomal Function. *Cell*, 162(5):1101–1112, 2015.

[99] R. E. Guzman, E. Miranda-Laferte, A. Franzen, and C. Fahlke. Neuronal ClC-3 Splice Variants Differ in Subcellular Localizations, but Mediate Identical Transport Functions. *J. Biol. Chem.*, 290(43):25851–25862, 2015.

[100] A. R. Graves, P. K. Curran, C. L. Smith, and J. A. Mindell. The Cl-/H+ antiporter ClC-7 is the primary chloride permeation pathway in lysosomes. *Nature*, 453:788–792, 2008.

[101] A. Roos and W. F. Boron. Intracellular pH. *Physiol. Rev.*, 61:296–434, 1981.

[102] M.M. Wu, J. Llopis, S. Adams, J.M. McCaffery, M.S. Kulomaa, T.E. Machen, H.P. Moore, and R.Y. Tsien. Organelle pH studies using targeted avidin and fluorescein-biotin. *Chem. Biol.*, 7:197–209, 2000.

[103] B. Alberts, A. Johnson, J. Lewis, M. Raff, K. Roberts, and P. Walter. Molecular Biology of the Cell. Fifth edition. *Garland Science, New York*, 1, 2008.

[104] W.I. Lencer, P. Weyer, A.S. Verkman, D.A. Ausiello, and D. Brown. FITC-dextran as a probe for endosome function and local-ization in kidney. *Am. J. Physiol.*, 258:309–317, 1990.

[105] A. K. Stewart, B. E. Shmukler, D. H. Vandorpe, F. Reimhold, J. F. Heneghan, M. Nakakuki, A. Akhavein, S. Ko, H. Ishiguro, and S. L. Alper. SLC26 anion exchangers of guinea pig pancreatic duct: molecular cloning and functional characterization. *Am J Physiol Cell Physiol*, 301(2):C289–303, 2011.

[106] N. Rahmati, K. Kunzelmann, J. Xu, S. Barone, L. Sirianant, C. I. De Zeeuw, and M. Soleimani. Slc26a11 is prominently expressed in the brain and functions as a chloride channel: expression in Purkinje cells and stimulation of V H(+)-ATPase. *Pflügers Arch*, 465(11):1583–1597, 2013.

[107] J. Xu, S. Barone, H. Li, S. Holiday, K. Zahedi, and M. Soleimani. Slc26a11, a chloride transporter, localizes with the vacuolar h^+-atpase of a-intercalated cells of the kidney. *Kidney International*, 80(9):926–937, 2011.

[108] N. Rahmati, M. F. Vinueza Veloz, J. Xu, S. Barone, N. Rodolfo Ben Hamida, M. Schonewille, F. E. Hoebeek, M. Soleimani, and C. I. De Zeeuw. SLC26A11 (KBAT) in Purkinje Cells Is Critical for Inhibitory Transmission and Contributes to Locomotor Coordination. *eNeuro*, 3(3), 2016.

[109] R. L. Rungta, H. B. Choi, J. R. Tyson, A. Malik, L. Dissing-Olesen, P. J. C. Lin, S. M. Cain, P. R. Cullis, T. P. Snutch, and B. A. MacVicar. The cellular mechanisms of neuronal swelling underlying cytotoxic edema. *Cell*, 161(3):610–621, 2015.

[110] F. W. Verheijen, E. Verbeek, N. Aula, C. E. Beerens, A. C. Havelaar, M. Joosse, L. Peltonen, P. Aula, H. Galjaard, P. J. van der Spek, and G. M. Mancini. A new gene, encoding an anion transporter, is mutated in sialic acid storage diseases. *Nat Genet*, 23(4):462–465, 1999.

[111] P. Morin, C. Sagne, and B. Gasnier. Functional characterization of wild-type and mutant human sialin. *EMBO J*, 23(23):4560–4570, 2004.

[112] L. M. Prolo, H. Vogel, and R. J. Reimer. The lysosomal sialic acid transporter sialin is required for normal cns myelination. *J Neurosci.*, 29(49):15355–15365, 2009.

[113] T. Miyaji, N. Echigo, M. Hiasa, S. Senoh, H. Omote, and Y. Moriyama. Identification of a vesicular aspartate transporter. *Proc. Natl. Acad. Sci. U. S. A.*, 105:11720–11724, 2008.

[114] J. Eriksen, R. Chang, M. McGregor, K. Slim, T. Suzuki, and R. H. Edwards. Protons Regulate Vesicular Glutamate Transporters through an Allosteric Mechanism. *Neuron*, 90(4):768–780, 2016.

[115] M. Martineau, R. E. Guzman, C. Fahlke, and J. Klingauf. Vglut1 functions as a glutamate/proton exchanger with chloride channel activity in hippocampal glutamatergic synapses. *Nature Communications*, 8(2279), 2017.

[116] J. Yang, J. Chen, M. del Carmen Vitery, J. Osei-Owusu, J. Chu, H. Yu, S. Sun, and Z. Qiu. Pac, an evolutionarily conserved membrane protein, is a proton-activated chloride channel. *Science*, 364(6438):395–399, 2019.

[117] F. Ulrich, S. Blin, K. Lazarow, T. Daubitz nad J. P. von Kries, and T. J. Jentsch. dentification of TMEM206 proteins as pore of PAORAC/ASOR acid-sensitive chloride channels. *Elife*, 8, 2019.

[118] H. Wang, T. Shimizu, T. Numata, and Y. Okada. Role of acid-sensitive outwardly rectifying anion channels in acidosis-induced cell death in human epithelial cells. *Pflugers Arch - Eur J Physiol*, 454:223–233, 2006.

[119] H. Omote, T. Miyaji, M. Hiasa, N. Juge, and Y. Moriyama. Structure, Function, and Drug Interactions of Neurotransmitter Transporters in the Postgenomic Era. *Annu Rev Pharmacol Toxicol*, 56:385–402, 2016.

[120] C. Mauvezin and T.P. Neufeld. Bafilomycin A1 disrupts autophagic flux by inhibiting both V-ATPase-dependent acidification and Ca-P60A/SERCA-dependent autophagosome-lysosome fusion. *Autophagy*, 11(8):1437–1438, 2015.

[121] D. Arosio and G. M. Ratto. Twenty years of fluorescence imaging of intracellular chloride. *Front Cell Neurosci*, 8(258), 2014.

[122] E. Wöll, M. Gschwentner, J. Fürst, S. Hofer, G. Buemberger, A. Jungwirth, J. Frick, P. Deetjen, and M. Paulmichl. Fluorescence-optical measurements of chloride movements in cells using the membrane-permeable dye diH-MEQ. *Pflügers Arch*, 432(3):486–493, 1996.

[123] H. Kaneko, I. Putzier, S. Frings, and T. Gensch. Determination of intracellular chloride concentration in dorsal root ganglion neurons by fluorescence lifetime imaging. In Fuller C.M. (Ed.). *Calcium-Activated Chloride Channels, Book Series: Current Topics in Membranes*, 53:167–194, 2002.

[124] U. I. Scholl, G. Stölting, J. Schewe, A. Thiel, H. Tan, C. Nelson-Williams, A. A. Vichot, S. C. Jin, E. Loring, V. Untiet, T. Yoo, J. Choi, S. Xu, A. Wu, M. Kirchner, P. Mertins, L. C. Rump, A. M. Onder, C. Gamble, D. McKenney, R. W. Lash, D. P. Jones, G. Chune, P. Gagliardi, M. Choi, R. Gordon, M. Stowasser, C. Fahlke, and R. P. Lifton. CLCN2 Chloride Channel Mutations in Familial Hyperaldosteronism Type II. *Nat Genet.*, 50(3):349–354, 2018.

[125] V. Untiet, P. Kovermann, N. J. Gerkau, T. Gensch, C. R. Rose, and C. Fahlke. Glutamate transporter-associated anion channels adjust intracellular chloride concentrations during glial maturation. *Glia*, 65(2):388–400, 2017.

[126] K. Leung, K. Chakraborty, A. Saminathan, and Y. Krishnan. A DNA nanomachine chemically resolves lysosomes in live cells. *Nature Nanotechnology*, 14:176–183, 2019.

[127] A. F. Dulhunty. The Dependence of Membrane Potential on Extracellular Chloride Concentration in Mammalian Skeletal Muscle Fibres. *J. Physiol.*, 276:67–82, 1978.

[128] J. A. Heiny, S. C. Cannon, and M. DiFranco. A four-electrode method to study dynamics of ion activity and transport in skeletal muscle fibers. *J. Gen. Physiol.*, 151(9):1146–1155, 2019.

[129] C. W. Habela, N. J. Ernest, A. F. Swindall, and H. Sontheimer. Chloride Accumulation Drives Volume Dynamics Underlying Cell Proliferation and Migration. *J. Neurophysiol.*, 101(2):750–757, 2009.

[130] S. Sulis Sato, P. Artoni, S. Landi, O. Cozzolino, R. Parra, E. Pracucci, F. Trovato, J. Szczurkowska, S. Luin, D. Arosio, F. Beltram, L. Cancedda, K. Kaila, and G. M. Ratto. Simultaneous two-photon imaging of intracellular chloride concentration and pH in mouse pyramidal neurons in vivo. *PNAS*, 114(41):8770–8779, 2017.

[131] J.-G. Zhou, J.-L. Ren, Q.-Y.-Qiu, H. He, and Y.-Y. Guan. Regulation of Intracellular Cl- Concentration through Volume-regulated ClC-3 Chloride Channels in A10 Vascular Smooth Muscle Cells. *The Journal of Biological Chemistry*, 280(8):7301–7308, 2005.

[132] C. Koncz and J. T. Daugirdas. Use of MQAE for measurement of intracellular [Cl-] in cultured aortic smooth muscle cells. *American Journal of Physiology-Heart and Circulatory Physiology*, 267(6):2114–2123, 1994.

[133] K. J. Treharne, R. M. Crawford, and A. Mehta. CFTR, chloride concentration and cell volume: could mammalian protein histidine phosphorylation play a latent role? *Experimental Physiology*, 91(1):131–139, 2005.

[134] S. Hosogi, K. Kusuzaki, T. Inui, X. Wang, and Y. Marunaka. Cytosolic chloride ion is a key factor in lysosomal acidificationand function of autophagy in human gastric cancer cell. *J. Cell. Mol. Med.*, 18(6):1124–1133, 2014.

[135] A. Pierzynska-Mach, P. A. Janowski, and J. W. Dobrucki. Evaluation of Acridine Orange, LysoTracker Red, and Quinacrine as Fluorescent Probes for Long-Term Tracking of Acidic Vesicles. *Cytometry A.*, 85(8):729–737, 2014.

[136] S.-H. Park, J. Y. Hyun, and I. Shin. A lysosomal chloride ion-selective fluorescent probe for biological applications. *Chem. Sci.*, 10:56–66, 2019.

[137] H. Pertoft, B. Wärmegard, and M. Höök. Heterogeneity of lysosomes originating from rat liver parenchymal cells. Metabolic relationship of subpopulations separated by density-gradient centrifugation. *Biochem. J.*, 174(1):309–317, 1978.

[138] C. Wasmeier, A. N. Hume, G. Bolasco, and M. C. Seabra. Melanosomes at a glance. *J. Cell Sci.*, 121:3995–3999, 2008.

[139] M. Faurschou and N. Borregaard. Neutrophil granules and secretory vesicles in inflammation. *Microbes Infect.*, 5:1317–1327, 2003.

[140] A. Chapel, S. Kieffer-Jaquinod, C. Sagne, Q. Verdon, C. Ivaldi, M. Mellal, J. Thirion, M. Jadot, C. Bruley, J. Garin, B. Gasnier, and A. Journet. An Extended Proteome Map of the Lysosomal Membrane Reveals Novel Potential Transporters. *Mol Cell Proteomics*, 12(6):1572–1588, 2013.

[141] S. Ohkuma, Y. Moriyama, and T. Takano. Electrogenic Nature of Lysosomal Proton Pump as Revealed with a Cyanine Dye. *J. Biochem.*, 94:1935–1943, 1983.

[142] M. Koivusalo, B. E. Steinberg, D. Mason, and S. Grinstein. In situ Measurement of the Electrical Potential Across the Lysosomal Membrane Using FRET. *Traffic*, 12(8):972–982, 2011.

[143] W. Wang, X. Zhang, Q. Gao, M. Lawas, L. Yu, X. Cheng, M. Gu, N. Sahoo, X. Li, P. Li, S. Ireland, A. Meredith, and H. Xu. A voltage-dependent K+ channel in the lysosome is required for refilling lysosomal Ca2+ stores. *The Journal of Cell Biology*, 216(6):1715–1730, 2017.

[144] A. L. Hodgkin and P. Horowicz. The influence of potassium and chloride ions on the membrane potential of single muscle fibres. *J Physiol*, 148:127–160, 1959.

[145] N. Juge, Y. Yoshida, S. Yatsushiro, H. Omote, and Y. Moriyama. Vesicular glutamate transporter contains two independent transport machineries. *J. Biol. Chem.*, 281:39499–39506, 2006.

Danksagung

Im Folgenden möchte ich mich bei allen herzlich bedanken, die mich in den vergangenen Jahren unterstützt und zum Gelingen dieser Arbeit beigetragen haben.
In erster Linie danke ich meinem Doktorvater Herrn Prof. Dr. Christoph Fahlke, der mir zugetraut hat, in einem fachfremden Gebiet zu promovieren und mir ermöglicht hat an diesem Forschungsprojekt in seinem Institut zu arbeiten. Er hatte stets ein offenes Ohr für mich und hat mich immer unterstützt und mit guten Ideen meine Arbeit vorangetrieben.
Ebenfalls bedanke ich mich bei Frau Prof. Dr. Christine R. Rose und bei Herrn Prof. Dr. Klaus Suhling für die Übernahme des Zweit- und Drittgutachtens dieser Arbeit.
Des Weiteren möchte ich mich bei meinen Betreuern Raul Guzman und Thomas Gensch, sowie bei Felix Beinlich für die anregenden Diskussionen und die fortwährende fachliche und technische Unterstützung bedanken.
Ich bedanke mich bei Arne Franzen, Petra Thelen und Maike Berndt für die großartige Hilfe in der Molekularbiologie.
Für die Synthese des diH-MEQ danke ich Markus Holschbach und Dirk Bier aus dem INM-5.
Ich danke meinen lieben Kollegen Bettina, Nadine, Daniel, Rachel, Juan, Jana, Anita, Arnd, Christoph, Claudia, sowie allen Mitarbeitern des IBI-1.
Insbesondere danke ich meiner Büronachbarin Miriam für die vielen netten Gespräche, die anregenden Diskussionen, die Unterstützung, die schönen Spaziergänge, und dafür, dass sie mich an meinen durchgeplanten Messtagen vorm Hungertod bewahrt hat.
Besonderer Dank gilt außerdem meinen Eltern, die mich schon mein ganzes Leben uneingeschränkt unterstützt haben, und meinem Mann David für die persönliche Unterstützung und die schönen Momente während unserer Zeit in Jülich.

Eidesstattliche Versicherung

Ich versichere an Eides statt, dass die Dissertation von mir selbstständig und ohne unzulässige fremde Hilfe unter Beachtung der "Grundsätze zur Sicherung guter wissenschaftlicher Praxis an der Heinrich-Heine-Universität Düsseldorf" erstellt worden ist.

Jülich, 21. Juli 2020

Andrea Jansen-Grabowski